11-5-2014

Miniature Ion Optics Towards a Micro Mass Spectrometer

Ashish Chaudhary
University of South Florida, achaudh2@mail.usf.edu

Miniature Ion Optics Towards a Micro Mass Spectrometer

by

Ashish Chaudhary

A dissertation submitted in partial fulfillment
of the requirements for the degree of
Doctor of Philosophy
Department of Electrical Engineering
College of Engineering
University of South Florida

Major Professor: Jing Wang, Ph.D.
Andrew Hoff, Ph.D.
Rudy Schlaf, Ph.D.
Ashok Kumar, Ph.D.
Friso van Amerom, Ph.D.
Tim Short, Ph.D.

Date of Approval:
November 5, 2014

Keywords: Micromachined Ion Traps, Deep Reactive Ion Etching, Planar Ion Funnel, Handheld Low-Power Chemical Sensor

DEDICATION

To my parents, my wife and my precious daughter who have inspired me in their own ways to pursue my dreams.

ACKNOWLEDGMENTS

I would like to express my sincere gratitude to Dr. Jing Wang for providing continued support and guidance throughout all phases of my pursuit for Ph.D. while working full time at SRI International. I would also like to thank my committee members Dr. Andrew Hoff, Dr. Rudy Schlaf and Dr. Ashok Kumar for serving on the defense committee. I really appreciate their time and consideration in reviewing my dissertation providing valuable feedback. I would like to take this opportunity to thank my mentor and boss Dr. Tim Short for over a decade of encouragement, guidance and professional growth. Lastly, I'd like to express my sincere gratitude and admiration for Dr. Friso van Amerom who constantly and consistently inspired me in this field of research and without whom many of the exciting experiments described in this dissertation would not have taken place.

I'd like to also thank the MEMS group at SRI International (Largo) for providing the cleanroom facility and guidance to develop custom microfabrication techniques.

TABLE OF CONTENTS

LIST OF TABLES

LIST OF FIGURES

ABSTRACT

This PhD dissertation reports the development of miniature ion optics components of a mass spectrometer (MS) with the ultimate goal to lay the foundation for a compact low-power micromachined MS (μMS) for broad-range chemical analysis. Miniaturization of two specific components a) RF ion traps and b) an ion funnel have been investigated and miniature low-power versions of these components have been developed and demonstrated successfully in lab experiments. Power savings, simpler electronics and packaging schemes required to operate the micro-scale RF cylindrical ion traps have been the key motivation driving this research. Microfabricated cylindrical ion traps (μCITs) and arrays in silicon, silicon-on-insulator and stainless steel substrates have been demonstrated and average power of as low as 55 mW for a low mass range (28 to 136 amu) and mass spectra with better than a unit-mass-resolution have been recorded. For the ion funnel miniaturization effort, simple assembly, small form factor and ease of integration have been emphasized. A simplification of the conventional 3D ion funnel design, called the planar ion funnel, has been developed in a single plate and has been tested to demonstrate ion funneling at medium vacuum levels (1E-5 Torr) using DC voltages and power less than 0.5 W. Miniaturization of these components also enables use of other novel ion optics components, packaging and integration, which will allow a new class of μMS architectures amenable for radical miniaturization.

CHAPTER 1

INTRODUCTION

In today's world, there is an insatiable appetite to know what, when and how in the quickest time possible. The technological revolution of telecom and internet has led to the peaking of this sense of awareness that spawns out into every aspect of our lives. One important aspect of this heightened awareness is chemical analysis. The driving force ranges from matters of homeland security to first responders; from a terrestrial regime to outer space explorations in search of life; from scientific/medical studies to commercial applications such as oil and gas exploration. To this effect, there has been a monumental effort in development of chemical sensors, detectors and analyzers with emphasis on simpler operation for the user, cost effective, enhanced mass analysis, rapid analysis cycle time, and miniaturization. When it comes to chemical analysis, mass spectrometry is often considered as the most extensive analytical technique and it has become a bench mark in this realm. In the following sections, I focus on the fundamentals of mass spectrometry and discuss the path towards miniaturization of mass spectrometers (MSs), towards a low size, weight, and power (SWaP) chemical detector.

1.1 Dissertation Outline

The organization of this dissertation is as follows.

Chapter 1 describes the introduction about chemical sensing and mass spectrometry and introduces the most relevant topics and theory about ion trap mass spectrometers.

Chapter 2 describes the development and demonstration of the first micro machined miniature ion trap in Si and validates the choice of miniature ion traps as ultimately low-power mass analysis. Critical improvements are mentioned.

Chapter 3 describes a gradient ion trap array with a range of ion trap geometry in the same Si chip. This method has been demonstrated as a rapid iterative step for determining the most optimum geometry and ease of validating other experimental studies.

Chapter 4 describes a novel planar ion funnel in a 2D form factor which can ultimately enable a simple approach for ion concentration from a large flux of dispersed ion to small volume such as that of a μCIT.

Chapter 5 describes the ongoing work, which makes use of novel ion optics (including μCIT arrays and broad beam electrons source) and packaging approach towards ultimately designing a μMS. Future direction is discussed with focus on optimizations critical for an efficient μMS design.

1.2 Mass Spectrometry

Mass Spectrometry is an analytical technique to determine the atomic or molecular mass of an unknown substance. The chemical of interest is introduced into a vacuum chamber in a controlled manner and ionized by an appropriate method to create ions of the analyte of interest. The ions are mass analyzed in a mass analyzer and detected, typically by a fast high gain electron multiplier to record the signal. The choice of ionization method, mass analyzer and detection method in the MS instrument determines the types of samples (solid, liquid, or gas) that can be mass analyzed, the method of mass analysis and how well the masses can be distinguished i.e. the mass resolution and specificity. The knowledge of the atomic/molecular mass can be used to determine the chemical composition of the compound, elemental/isotopic configurations, and in some cases indirect analysis of proteins and peptides. The range of samples types that can be analyzed and the mass resolution offered by mass spectrometry lends itself to a broad spectrum of applications such as medical diagnosis and DNA sequencing, homeland security for screening hazardous substances at high throughput transits such as airports, monitoring of hazardous natural and man-made dangers such as chemical warfare

agent manufacturing and storage, industrial process control, basic scientific investigations, oil and gas exploration and low earth orbit and outer space explorations.

1.3 Ion Trap Mass Spectrometer

A mass spectrometer is an instrument that creates a controlled vacuum environment to analyze the chemical of interest in its charged state, i.e., ions. The mass analysis can be performed by several methods such as electrostatic fields, electrodynamic fields, magnetic fields or a combination of these. MS classification extends widely based primarily on the type of mass analyzer used and the method of introduction/ionization of the analyte. Some of the most popular types of mass analyzers include quadrupole mass filters [1], triple quads [2], time of flight [3], quadrupole time-of-flight [4], magnetic sectors [5] , ion cyclotron resonance [6] and ion traps [7]. This research focuses on 3D RF ion traps as the mass analyzer due to the inherent amenability of ion traps for miniaturization and ease of construction. We will focus on the class of MS instrument that uses RF ion traps as mass analyzers and are commonly referred to as an "ion trap mass spectrometer" (ITMS).

1.3.1 Quadrupole Ion Trap

The original quadrupole ion trap (QIT) also known as the "Paul Trap" is a 3D version of the quadrupole mass filter and was invented by Wolfgang Paul in 1953. Instead of trapping the charged particle in a two dimensions as in a quadrupole mass filter, the QIT forms a 3D trapping potential, by virtue of the 3D form-factor obtained by stacking 3 electrodes together. By applying the appropriate RF potential on the ring electrode and grounding the endplate electrodes, the ions can be trapped in a stable trajectory at the center of the QIT assembly. Figure 1 shows the construction of the QIT and other components used to operate the QIT as a mass spectrometer. The QIT uses hyperbolic shapes on the surfaces of the ring and endplate electrode facing each other to generate a quadrupolar potential well. The two endplate electrodes have a center through-hole to allow entry and exit of ions from the potential well. In the case of internal

ionization, the ion gate can be replaced by a source of electrons, such as a tungsten filament, at the entrance endplate, to cause internal ionization of analytes present inside the QIT volume.

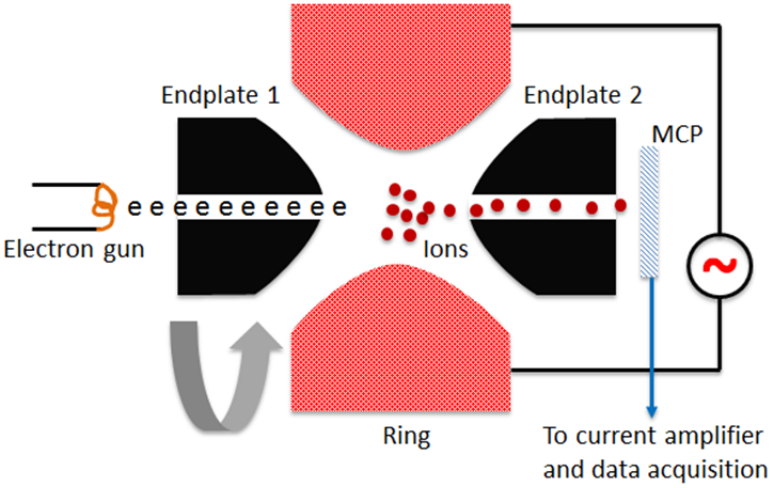

Figure 1 A schematic of an ITMS using QIT as the mass analyzer.

With the application of an appropriate amplitude and frequency of the RF potential to the ring electrode, the ion cloud at the center of the trap experiences a restoring force that continuously drives the ions back to center, circulating in a cloud of small trajectories. The quadrupolar potential generated due to the hyperbolic shape of the electrodes generates a linear electric field. This in turn applies a force that is linear to the relative displacement of the ion at that moment of time during trapping.

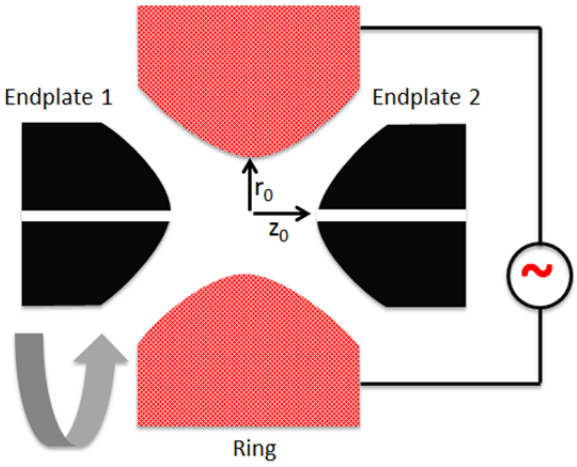

Figure 2 A cross-sectional view of the QIT along the cylindrical axis illustrating the radial and axial dimensions of the trap geometry.

The motion of the ions in the QIT can be described using the second-degree differential equation, as shown by Mathieu [9]. The force applied on the ions inside the QIT can be defined in terms of the Mathieu's parameters a_z and q_z and the trapping performance can be derived as follows:

$$a_z = -8eU/mr_0^2\,\Omega^2 \quad q_z = 4eV/mr_0^2\Omega^2 \qquad (1)\ [7]$$

where a_z and q_z are the dimension-less Mathieu's parameters, U and V are the DC and the RF potentials (volts) applied respectively, e is the charge of a singly charged ion (1.6E-19 C), m is the atomic/molecular mass (kg) of the trapped ion, r_0 is radius of the trap (Figure 2) and Ω is the angular frequency (rad/s) of the RF potential.

Equation 1 represents a perfect QIT, where $r_0^2 = 2z_0^2$, to obtain an ideal quadrupolar field [7].

1.3.2 Stability Diagram

The trajectory of the trapped ions and their stability can be defined in terms of stability/instability diagram using Equation 1. Figure 3 illustrates the plot of the stability diagram where az represents the ejection boundary in the radial direction and q_z represents the ejection criteria of ions in the axial direction.

To determine the stability of a particular ion, a_z and q_z can be calculated using Equation 1 and based on the values of the a_z and q_z, the ion's stability can be assessed. Conversely, other factors (RF potential amplitude, frequency, and size r_0) of the Equation 1 can be adjusted to operate the QIT to trap ions of a certain mass. For a perfect QIT geometry, the stability extends out to a max q_z value of 0.908, which is commonly referred to as the low-mass cut-off (LMCO) range. Conversely, for a trap operating as q_z 0.908, any ion with a mass lower than the LMCO will not be trapped as the resulting q_z value for that particular ion will be > 0.908.

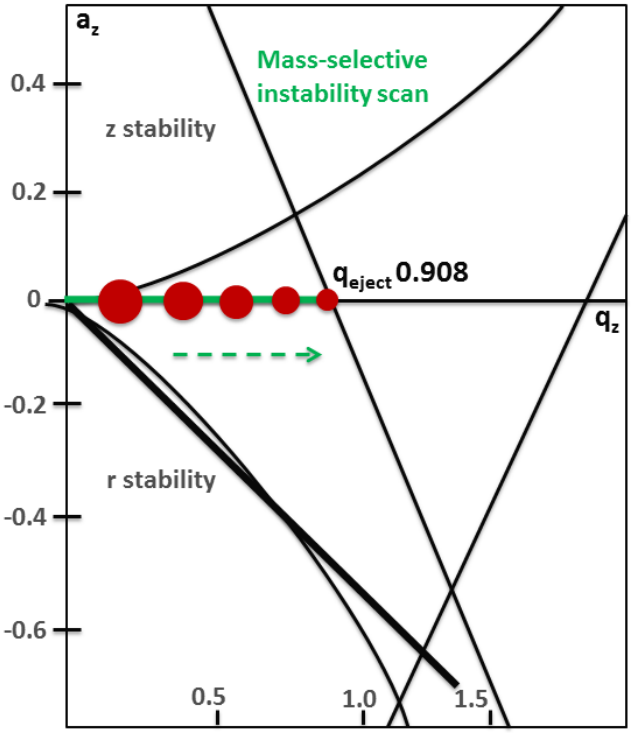

Figure 3 A plot of the stability diagram with red dots representing ions of different masses

One common type of mass analysis makes use of the “mass-selective instability mode”, in which the QIT is operated using RF potential, while the DC potential is kept zero, as illustrated by the green line in Figure 3. In this case, the value of a_z is zero and the ion stability can be plotted on the x-axis for different q_z value. As the ions are trapped at a certain set of parameters (for q_z<0.908), they can be cooled down to shrink to a smaller cloud via collisional cooling with background atoms. He is a common buffer gas used for this purpose. Collisional cooling has been demonstrated to improve the mass resolution by virtue of extracting thermal kinetic energies of the ions [11] . Once trapped for a few ms, the RF potential can be ramped and the increasing q_z value, as depicted in Figure 3 and 4, the ions can be ejected sequentially in the increasing order of the mass to charge ratio. For singly charged ions, this means the ions will eject out in the increasing order of their masses. This signal when detected using a fast high-gain electron multiplier is used to create the mass spectrum.

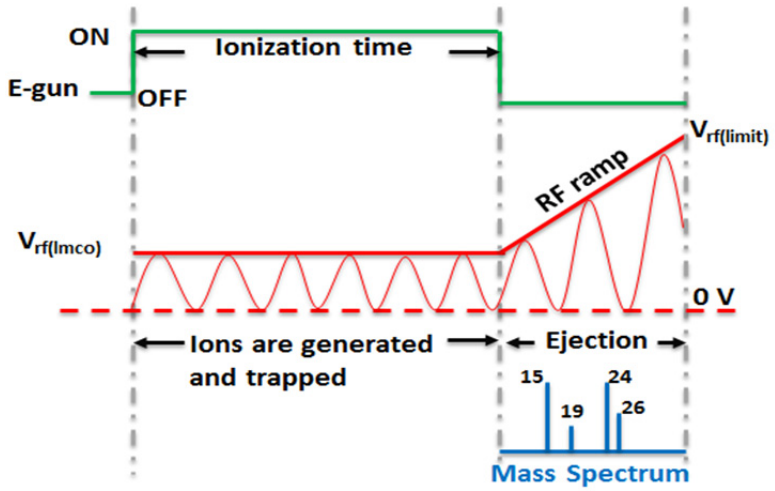

Figure 4 Illustration of waveform sequence for practical implementation of mass-selective instability mode operation for ions generated internally inside the QIT.

1.3.3 Axial Modulation

As ions are trapped in the parabolic shaped pseudo-potential well inside the QIT, the trajectories of the ions are defined by two main frequencies, also called the secular frequencies. The two secular frequencies define the motion of ions in the axial and radial directions. At one instant in time, the ion is being forced towards the center of the trap radially, while it is also forced away from the center of the trap axially. This simultaneous focusing and de-focusing effect in axial and radial dimension results in an “8”-shaped trajectory [12] traversed by the ion during a few micro seconds. The ions oscillating in these trajectories can be “excited” by applying a very low amplitude RF signal on the endplates. Typical potentials required to cause this excitation is on the order of few millivolts, and about half or one-third of the main RF frequency. This method of exciting the ions is called resonant excitation and is a fraction of the axial secular frequency is used for excitation; it is commonly referred to as “axial modulation”. Axial modulation has been demonstrated to improve the mass resolution [13] of the ion traps by virtue of ejection of ions of similar masses in a tighter packet during RF ramp mass ejection, while minimizing the perturbation from ions of higher masses still trapped [12]. Axial modulation has also been found useful in order to increase the mass range of the QIT [14].

1.3.4 Miniature Cylindrical Ion Traps

A cylindrical ion trap (CIT) is a simplified modification of the QIT, where the hyperbolic shape of the electrodes is replaced by a cylindrical shape. The CIT geometry was patented in early 1960s [15] and since then has been demonstrated by various groups for mass analysis in mass selective instability mode [16-19], and also as ion storage devices [20, 21] . Figure 5 illustrates the geometry of CIT in comparison to a QIT as generated in ion optics software SIMION to display the trapping potential.

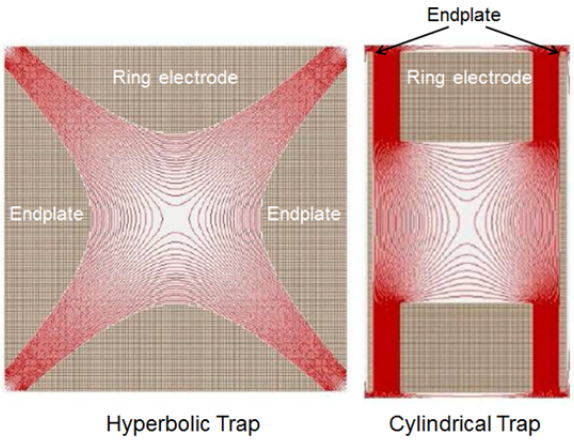

Figure 5 A comparison of QIT vs. CIT geometry and trapping potential contours (in red).

CITs are an attractive candidate choice of mass analyzer for this research as the cylindrical shape lends itself amenable to miniaturization due to the ease of construction via conventional machining as well as micro machining processes. Miniature CITs allow drastic reduction in RF trapping voltage (V_{rf}) required for mass analysis for the same mass as compared to the larger counterparts, thereby drastically reducing the overall power consumption [22]. Equation 2 defines the ion trap LMCO (ions with *m/z* larger than this value are trapped, while smaller ions are ejected from the trap):

$$(m/z)_{bnd} = -4A_2V_{rf}/q_{bnd}r_0^2\Omega^2 \quad (2)$$

where A_2 is the relative contribution of the quadratic term in the multipole description of the trapping potential, q_{bnd} is the boundary of the ion trap stability region on the *q* axis, r_0 is the radius of the ring electrode, and Ω is the angular frequency of the trapping RF voltage [11].

As an example, a commercial hyperbolic ion trap that has a typical r_0 of 1 cm uses RF voltages up to 7000 $V_{0\text{-}p}$ at 1 MHz for an analysis mass range of 700 m/z. Reducing r_0 to 0.5 cm would decrease the required voltage to 1750 $V_{0\text{-}p}$ at the same frequency. If r_0 were only 0.5 mm, the RF voltage at 1 MHz would be 17.5 $V_{0\text{-}p}$, a tremendous savings in voltage and power, and therefore in overall mass spectrometer size and electronics as well. It should be noted, however, that the trapping RF frequency must usually be increased in very small traps to trap enough ions (ions must be redirected more frequently to avoid collision with the ion trap electrodes). In addition, the RF amplitude must be high enough to provide an adequate potential well to efficiently trap the ions. Thus, using a more realistic 5 MHz frequency, the 0.5 mm r_0 trap would need an RF voltage of 437 $V_{0\text{-}p}$ for the same mass range as the typical commercial trap, still a reduction in voltage by a factor of 16.

Equation 2 describes the power *P* as a function of the capacitance of the ion trap, voltage V_{rf}, the angular frequency Ω, and *Q*, the quality factor of the tuned circuit. It shows that a reduction in V_{rf} will reduce the power by the square of V_{rf} if the frequency, quality factor, and capacitance are kept constant. For the example discussed above, the voltage reduction factor of 16 results in a 256-fold decrease in power consumption. Power increases as a linear function of frequency [23].

$$P = CV_{rf}{}^2\Omega/2\pi Q \tag{3}$$

A lower RF voltage requirement also alleviates stringent design aspects and allows components to be packed into a smaller overall foot print. Simpler RF electronics directly reduce the resource allocation required on an instrument level and often are cost-effective to manufacture.

1.3.5 Array of Ion Traps

One drawback of scaling down the size of the CITs is the reduced trapping capacity per trap. Simulation-based analysis indicate that the number of trapped ions scales as the 1.55-1.75

power of r_0 [24]. This translates into lower sensitivity per miniature CITs due to decreased number of ions of the chemical of interest that can be analyzed. One way to circumvent this problem is to build a multitude of miniature CITs and operate them in unison. By doing so, the sensitivity lost due to miniaturization can be recovered, while maintaining the power and voltage savings of a miniature trap.

The number of ions that can be trapped in a CIT scales with the radius (r_0) of the trap [25]. Figure 6 illustrates the relationship of the analyzable ions as compared to radius and number of traps in an array.

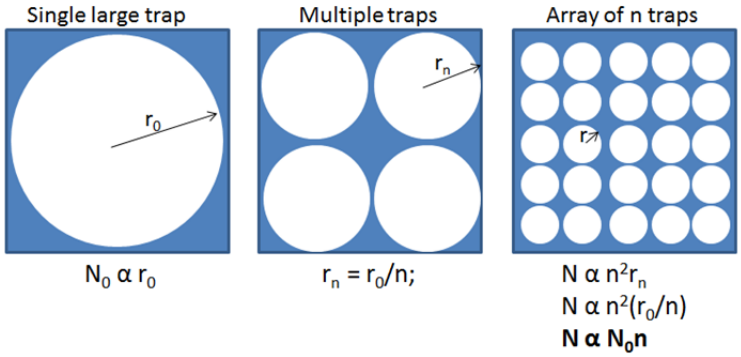

Figure 6 Scaling of number of ions trapped (N) with CIT array size (n)

If the foot print of the mass analyzer is kept constant, then the number of ions trapped in an array of n smaller traps scales with the size of the array.

1.4 Motivation and Potential for μ-Mass Spectrometers

Figure 7 shows an example of the evolution of miniature MS instrumentation in the commercial market for the past few decades. One of the main focuses in ITMS has been the solution path towards a low SWaP instrument that would enable cost effective and rapid in-situ chemical analysis and thereby provide real-time assessment of potentially hazardous events/scenario. In order to take mass spectrometry to the field, the overall foot print and complexity needs to be reduced. In-field measurements also require instruments that are relatively more tolerant to shock and vibrations. Power consumption is a crucial factor that needs to be addressed when designing miniature instruments as battery packs also needs to be

reduced to relieve the overall resources required to operate chemical screening mission. To enable novel missions, such as a dispersive network of sensors, these instruments need to be cost-effective and highly repeatable. Novel components and design concepts are needed to incorporate radical miniaturization.

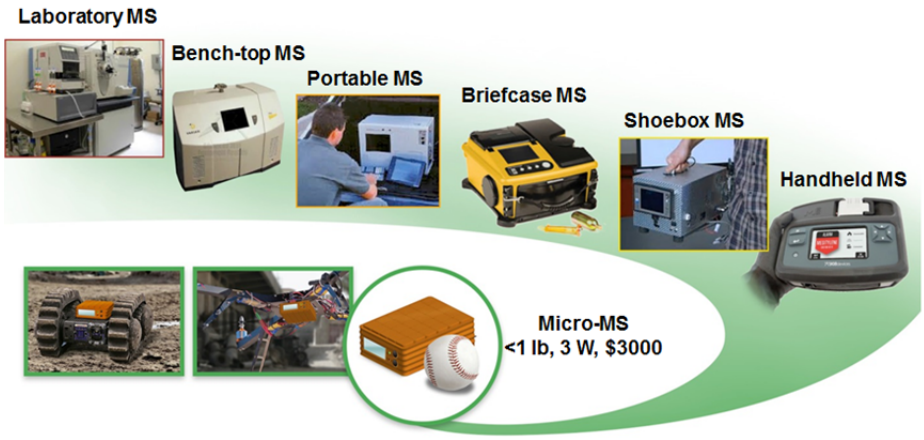

Figure 7 The evolution of MS instrumentation towards miniaturization that will enable stand-off "on-the-go" chemical screening missions on mobile platform.

The ultimate goal of this research is to lay the foundation for low SWaP-C MS instruments that will ultimately transform the MS from an "instrument" to a "device" scale. It is worth mentioning here that there has to be an optimum balance of the savings in all aspects of SWaP-C, as any one of these factor will prevent use of such devices in a large scale dispersive network configuration.

Some of the critical applications where this perceived μMS device would be highly applicable are:

- Handheld detection for homeland security
- Networked detection across sea ports and airports
- Single point and networked constellation for LEO weather awareness, space and planetary exploration
- Pervasive environmental monitoring (Ocean, Terrestrial and Atmospheric)

- Single point and pervasive stand-off chemical screening for protection of warfighters against chemical warfare agents (CWAs), toxic industrial compounds and explosive related compounds (ERCs)
- Consumer applications including household applications towards general awareness and improvement in standard of life. Some examples are mold detection, fouling of food in refrigerators, personal heath devices etc.

The global mass spectrometry market was assessed at $ 3.9B in 2013 and is expected to exceed $ 5.9B by the year 2018 [26]. It is worth pointing out that this market assessment is based on the current MS instrumentation which lends itself in applications which are limited to mostly scientific, clinical environmental and defense. It is expected that the availability of the above described form-factor and capabilities of μMS devices will significantly broaden the application base, as shown in Figure 8 and the market potential can be many folds higher than assessed currently.

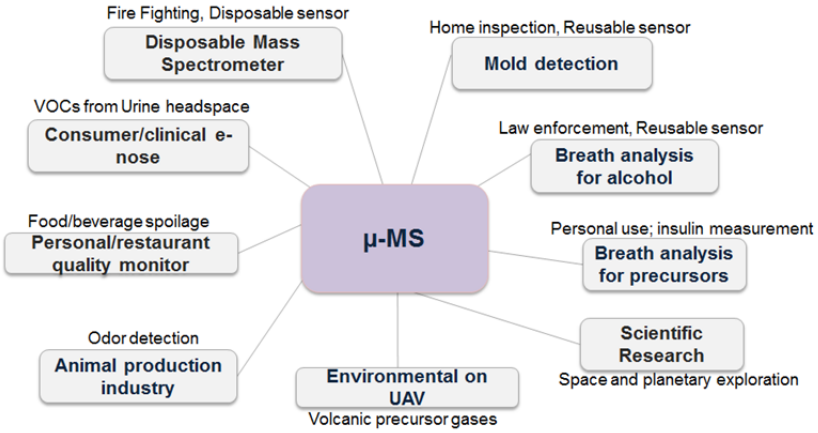

Figure 8 Expected application base for μMS

CHAPTER 2

μCIT ARRAY: GENERATION-1

2.1 Abstract

This chapter[1] describes a novel approach, in which MEMS technology is used for constructing miniature CIT mass spectrometer (MS) arrays in silicon (Si), is described. MEMS processes were used to fabricate precise μCIT geometries in a stack of Si, SiO_2, and Si_3N_4. These geometries were then selectively coated with conductive (Cr/Au) layers to obtain a functional μCIT array with individual μCIT radii (r_0) of 360 μm, half-thickness (z_0) of 351 μm and aperture size (r_H) of 162 μm. Each trap of a 5 × 5 CIT array was operated in the mass selective instability mode to analyze trichloroethylene (TCE) and perfluorotributylamine (PFTBA) at a pressure of 10^{-5} Torr. Mass spectra from individual μCITs in the array were obtained using a rasterable electron beam for internal ionization. Investigation of the operation of individual μCITs in the array is a critical step towards the understanding of the overall functioning of mass spectrometer arrays.

2.2 Background

Miniaturized chemical sensors are in ever increasing demand as in-situ analyzers for a wide range of applications, including environmental monitoring and homeland security [27]. Handheld sensors, for example, can be used for real-time mapping of toxic chemicals, on-site detection of specific hazardous materials, discovery of short-lived chemicals in the environment,

---

[1] This chapter was published in Journal of Microelectromechanical Systems (10.1109/JMEMS.2009.2013390). Permission is included in Appendix A.

and tracking of rapid fluctuations of chemical concentrations [28, 29]. They may also be used for large scale autonomous industrial monitoring and point-of-care medical analysis. For harsher environments and exacting situations, future devices will need to be able to handle multiple complex samples rapidly with high specificity and sensitivity. These sensors will also need to have low power consumption and be relatively inexpensive. Present day MS instruments are relatively costly and large. If miniaturized, they could be good candidates for handheld chemical analyzers due to their accuracy, sensitivity and short response time [30]. Cost reduction of miniaturized MSs could ultimately lead to large-scale deployments of MS sensors for parallel monitoring, and networks of MS analyzers that can instantly detect and report chemical anomalies [31].

With the advent of microelectromechanical systems (MEMS) technology, new avenues are now possible for building extremely small structures with micrometer precision in a variety of substrates. Several research groups have demonstrated the use of MEMS fabrication techniques to miniaturize MS components. For example, various mass analyzers [32-37], Faraday cup detectors [38], ionization sources [39-41], and micro-scale vacuum pumps [42-44] have been successfully fabricated and operated for proof of concept. Other examples of MEMS-based components related to the field of MS miniaturization are micromachined gas chromatograph (GC) columns [45], microfabricated sample introduction systems [46], and micromachined electrospray ionization (ESI) devices [47]. Integration of multiple components into a truly miniature microfabricated mass spectrometer [37] could lead to production of extremely powerful and cost-effective chemical analyzers. One significant advantage that MEMS fabrication strategies have over conventional machining methods is that they enable low-cost batch production of high-precision geometries and easy integration of these geometries to obtain millimeter-scale assemblies.

A reduction in system performance, however, often results from component miniaturization. For example, MS miniaturization is typically accompanied by a reduction in

sensitivity. In the case of miniature ITMSs, this loss of sensitivity results primarily from lower transmission of ions and electrons into and out of the traps, as well as from the lower ion storage capacity of smaller ion traps. Sensitivity can, in principle, be regained by using an array of miniature ion traps that operate in unison [48]. Aside from the potential for low-cost batch fabrication of MS devices, arrays of microfabricated miniature ion traps can operate at much lower trapping voltages [33] than larger commercially available ion trap MSs, thereby significantly reducing the overall power consumption of the MS system. The array approach has the additional advantage in that MS arrays could be used to perform parallel analysis for increased throughput or accuracy [49].

As the underlying methods of MEMS fabrication are fundamentally different from conventional machining, MEMS approaches might provide radically new ways to design ion optics and other MS components that have the same functionality as their larger counterparts, but with improved redundancy or reliability [50]. For example, most commercial ion trap mass spectrometers use ion traps with high-precision hyperbolic electrodes and a typical ring-electrode radius of 1 cm. It has been shown that the trapping electric potential produced by a hyperbolic geometry can be closely approximated by a cylindrical geometry [17, 18]. Since the introduction of CITs in the 70s [16], numerous research groups have investigated CIT performance as a MS [51-53]. Also, several groups have improved the theoretical models for optimization of performance of CIT MSs [54-56]. Cylindrical structures are much easier to miniaturize and micro machine than hyperbolic electrodes. Therefore, in the present work MEMS fabrication methods were used to construct an array of μCIT mass spectrometers with radii of 360 μm. Data obtained from the μCIT array are reported, and future strategies are discussed. It is likely that future MEMS-fabricated mass spectrometer ion optics will deviate even further from conventional MS ion optics, allowing the implementation of radically new designs [57] that have not been possible to realize with conventional approaches.

2.3 Fabrication

A MEMS process was developed to construct arrays of μCITs. The three-dimensional structures were built in silicon (Si) wafers, with thermally grown silicon oxide (SiO_2), and low pressure chemical vapor deposition (LPCVD) silicon nitride (Si_3N_4), by using bulk micromachining. The approach [58] was to build μCIT arrays by fabricating two symmetrical half-μCIT arrays, selectively metallizing specific areas of the Si and Si_3N_4 layers by sputtering Cr/Au, and then bonding the two half-arrays back-to-back. The strategy of using conductive and non-conductive materials followed by metallization to make metal-coated ion optics has been validated in our previous work on fabrication of a low temperature co-fired ceramics (LTCC) based miniature CIT [59].

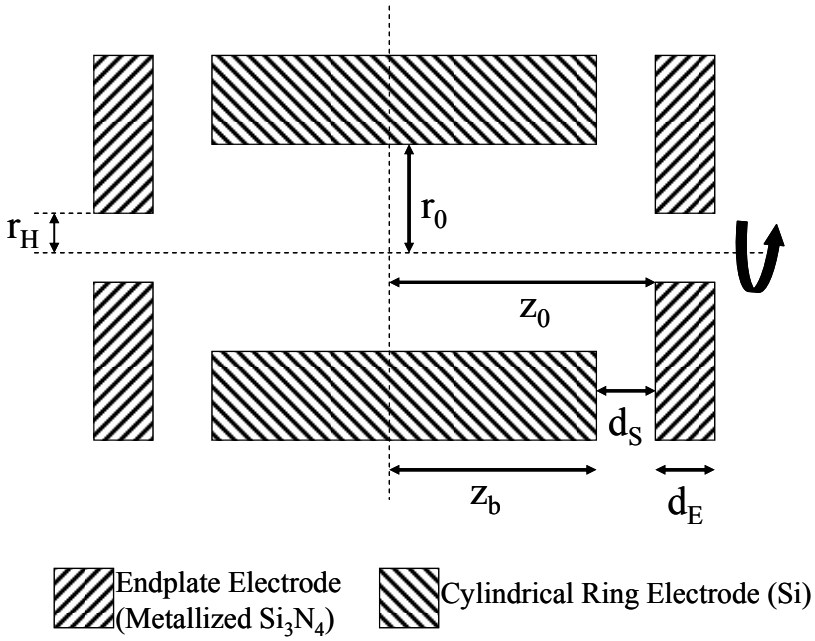

Figure 9 Schematic representation of cylindrical ion trap geometry and its dimensions.

Figure 9 is a schematic representation of one CIT in the fabricated array where (r_0) is the radius of each CIT ring electrode, (d_E) the endplate thickness, (d_s) the endplate spacing, (z_b) the ring electrode thickness and (z_0) the distance from the center of the (Si) ring electrode to the metallized endplate aperture (Si_3N_4). The change in Si thickness during wet thermal oxidation was taken into account to determine the final value of z_0. Three optical contact photomasks, one

each for ring electrode pattern, endplate pattern and metallization pattern were designed with Coventorware 4.0. These masks were obtained commercially from the Nano Fabrication Center (NFC) at University of Minnesota (Industry standard, 0.09 in thick, 5 × 5 in^2 dimensions, dark field chrome-on-soda-lime optical masks).

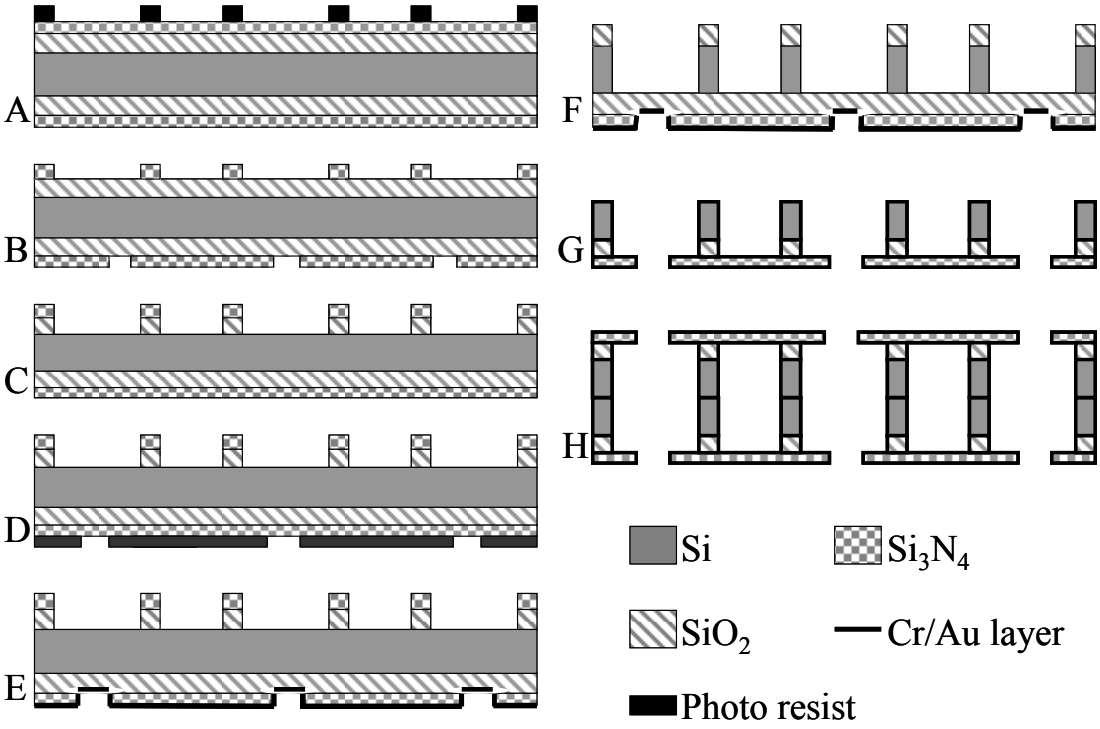

Figure 10 Schematic of the final fabrication process developed for μCIT array.

Figure 10 describes the process flow used to fabricate the μCIT arrays. The schematic depicts only three μCIT units for simplified portrayal, but the process was applied to a Si wafer (100 mm diameter) with multiple 5 × 5 arrays of varying r_0. Each wafer had pairs of identical arrays for each r_0 to simultaneously obtain two symmetrical half-μCIT structures. Since typical wafers can differ in thickness by ± 25 μm, numerous arrays of a range (325 μm to 375 μm) of r_0 were incorporated in the optical mask to make sure there was a range of z_0/r_0 ratios (0.82 to 1.23) obtained in each processed wafer. The process steps are described below in sections A through H and correspond with the process steps in Figure 7. To prepare the starting substrate, a 5μm thick layer of SiO_2 was thermally grown on a (100) low resistivity (0.001-0.005 ohm-cm)

n-type 350 μm thick double-sided polished Si wafer. This process was followed by deposition of a 3 μm thick layer of Si_3N_4 using LPCVD.

2.3.1 Ring Electrode Lithography (A-C)

Hexamethyldisilazene (HMDS), an adhesive promoter, was spun onto the starting substrate at 3000 r/min for 40 s. This process was followed by spinning a positive photoresist (PR) S 1827 (Shipley Microposit) at 3000 r/min for 40 s. The wafer was baked at 90 ºC for 60 s on a hot plate and exposed to 365 nm light for 6 s with an energy of 198 mJ/cm^2 in a mask aligner (EV620) using the ring-electrode mask. The PR was developed in a MF319 developer (Shipley Microposit) and the exposed Si_3N_4 was completely etched in an inductively coupled plasma (ICP) based reactive ion etching (RIE) instrument operating at 200 W of RF power, 45 SCCM of CF_4 and 5 SCCM of O_2 at 30 mTorr for 135 min. The wafer was then placed in 49% hydrofluoric acid (HF) for 5 min to etch the underlying exposed 5 μm thick SiO_2 layer, to expose the Si areas to be etched, as defined by the ring-electrode mask. The Si etch step (step F) was performed later so that the backside of the wafer could be patterned with the endplate pattern before the bulk Si was etched away. Spinning the wafer on a vacuum chuck with the bulk Si etched away didn't seem to be a feasible option due to fragility issues.

2.3.2 Endplate Lithography and Metallization (D and E)

A similar lithography procedure was performed on the back side of the substrate using the endplate mask to obtain an aperture in each endplate. The endplate pattern was backside aligned with the ring electrode pattern on the opposite side. The exposed Si_3N_4 was etched using an ICP-based RIE, exposing the underlying SiO_2 layer. The wafer was then dipped in 49% HF for 1 min to partially etch back the SiO_2 layer. The partial isotropic etch created a rounded SiO_2 undercut under the Si_3N_4 aperture edge. This 1 μm undercut was incorporated to physically isolate a next Cr/Au layer deposited on the Si_3N_4 from the Cr/Au layer on this SiO_2 layer, in order to lift off the Cr/Au along with the SiO_2 layer during a following SiO_2-release etch step (step *G*).

Lithography was then performed in the following manner on the backside using a negative PR to ensure metallization over the entire endplate (Si_3N_4) surface, except at the location of the dicing street. Negative PR 1500 (Futurrex Inc.) was spun at 3000 r/min for 40 s followed by a 1 min bake at 150 °C. The metallization mask was aligned to the apertures on the wafer using front side alignment and the wafer was exposed to 365 nm light for 15 s with energy of 198 mJ/cm^2. The wafer was post-baked at 100 °C for 1 min before developing in a resist developer RD6 (Futurrex Inc.) for 15 s. The 150 Å of Cr, followed by 2500Å of Au, was sputtered onto this backside. The Cr layer was used to improve the adhesion of the Au layer. The sputtering was performed in 2 mTorr of Ar with 360 W of RF power. A Cr/Au layer was chosen to achieve high conductivity, and to allow for Au-Au thermal compression bonding (TCB) and Au wire bonding processes, used during the packaging stage (step H). The wafer was kept in acetone for 2 hr and subsequently rinsed to strip off the remaining PR and metal deposited on the PR.

2.3.3 Ring Electrode Fabrication (F)

To create arrays of ring electrodes with half thickness cylinders (dimension z_b as shown in Figure 6), the exposed Si on the front side of the wafer was etched through its entire thickness. These deep cylindrical geometries were etched in Si by using the Si_3N_4/SiO_2 as a hard mask in an ICP-based deep reactive ion etching (DRIE), in which a mixture of SF_6, Ar, and C_4F_8 radicals were used according to the Bosch process [60]. After 445 Bosch cycles at 15 mTorr and 400 W of ICP power, the Si was completely etched through, forming an array of cylinders and stopping on the back-side SiO_2. The Si_3N_4 layer of the Si_3N_4/SiO_2 mask layer gets completely etched during the DRIE process exposing the SiO_2 layer on the front side.

2.3.4 SiO_2 Release and Metallization of Ring Electrode (G)

The processed wafer was dipped in 49% HF for 4 min to etch the exposed SiO_2 layer to reveal the Si_3N_4 endplates with apertures. This release step was extended for an extra 10 min to

create a 15 μm undercut in the SiO_2 layer between Si and the Si_3N_4, in order to provide electrical isolation between the endplate and ring electrodes during metallization.

A 150/2500 Å layer of Cr/Au was sputtered at an angle while rotating the substrate onto the front side surface of the wafer to obtain a conductive layer on the un-etched flat Si surface, the Si surface inside the arrays of cylinders, and the Si_3N_4 (endplate) surface at the bottom of the cylinders. As mentioned above, the shadow region (15 μm undercut) prevented formation of a continuous metal layer between the metallized Si cylinder and metallized Si_3N_4 endplates.

2.3.5 Packaging of the μCIT Array (H)

PR S1827 was then sprayed onto the wafer and baked for 30 s at 90 °C to encapsulate the undercut area and the cylinders from any particles that might be generated during the dicing process. The wafer was diced into separate arrays of 7.6 × 6.7 mm^2 chips. The chips were dipped in acetone and methanol sequentially to strip the PR and to remove any residue.

The half-μCIT array structures were tested individually for electrical isolation between the half cylinder and the endplate electrodes. Before flip-chip bonding, the two half arrays were rotated by 180 ° with respect to each other in order to provide access to the Au-coated flat Si surface, for electrical connections. The two identical half-μCIT array structures were pressed back-to-back under 0.8 MPa pressure at 320 °C for 2 min in a FineTech flip chip bonder. Under these conditions, Au-Au thermo compression bonding occurred and a single complete μCIT array was obtained. The bonded μCIT array was mounted with conductive epoxy onto a PCB, (with Au coated Cu traces) to electrically connect one endplate. Wire bonds were made with Au wire (diameter of 25 μm), connecting the ring electrode and the other endplate electrode to the PCB. Copper wires, to be attached to the electric feedthrough of the vacuum system were then soldered onto the traces of the PCB.

2.4 Testing

Ion trap mass spectra are typically obtained using a mass instability scan, whereby the LMCO for ion trapping is raised by a linear ramp of the RF trapping voltage (V_{rf}). The LMCO is

the smallest mass-to-charge ratio $(m/z)_{bnd}$ (bnd equals boundary) of an ion that can be trapped for a particular set of ion trap parameters. Equation (2) relates the LMCO to the operational parameters of a CIT MS [18, 61, 62] and can be used to assign mass values in Th (Thompson or m/z) to the peaks in the experimentally derived mass spectra.

$$(m/z)_{bnd} = -4A_2V_{rf}/q_{bnd}r_0^2\Omega^2 \quad (2)$$

where (Ω) is the RF angular frequency (in rad/s), (q_{bnd}) is the dimensionless value of the RF Mathieu parameter at the boundary of the ion trap stability diagram [7], and (A_2) is the quadrupole component of the electric potential in the z-direction inside a CIT. The typically accepted value for q_{bnd}, (for the common case where the DC Mathieu parameter (*a*) is zero) is 0.90805 [63]. The parameter A_2 depends on variables such as ring electrode-to-endplate spacing d_s, the thickness of the endplates d_E, the endplate aperture radius r_H and the ratio z_0/r_0. To determine A_2 (as well as other multipole components) for the ion traps in our array, the electric potential inside a μCIT (endplate to endplate) was numerically calculated (A_2=0.64) using a finite difference software package, SIMION [64]. A least squares fit was then performed in MATLAB to obtain the multipole components of the numerically determined electric potential along the z-axis of the μCIT. A more detailed description of this approach is described in a previous publication [59].

Experiments were performed in a vacuum chamber with gas inlets and a holder to accommodate the packaged μCIT arrays (reported earlier [59]). Vacuum was obtained using an Adixen ATH 31+ turbo pump backed up by a KNF N813.4ANI roughing pump. Analytes (TCE >99.5% purity from Sigma/Aldrich and PFTBA calibration compound FC43 from SIS) were introduced from a vial, held at 30 ºC, through a capillary (360 μm o.d., 50 μm i.d. and 25 cm in length) connected to stainless steel tubing that directed the gas towards the μCIT array. Helium (He) was used as a carrier gas for analytes and as a buffer gas. Gas phase analytes were ionized with an ELG-2 electron gun from Kimball Physics Inc., which was positioned 3 cm away

from one endplate of the μCIT array. A Kimball Physics x-y raster controller (EGPS-2) was used to deflect the electron beam and allow examination of the performance of each CIT in the array. On the other side of the μCIT array was mounted an electron multiplier detector (Detech model DeTech XP-2074) for detection of ions ejected from each μCIT during the instability scan. When the electron beam was switched on, the detector was switched off, and vice versa, to avoid overloading the detector. The detector operation voltages, -1550 V to -1850 V ("on-mode") and -900 V ("off-mode") were provided by a KEPCO high voltage power supply.

The following procedure was used to determine the optimum deflection plate voltages to direct the electron beam through each μCIT for internal ionization of analytes. With the μCIT trapping voltage off, both the detector and electron gun were switched on and the x-y raster controller voltages were adjusted to find each μCIT. When the electron beam was properly aligned through a μCIT, a maximum number of ions was formed between the μCIT and electron multiplier and subsequently detected. The deflection plate voltages that resulted in the maximum ion generation were recorded for each μCIT and then subsequently used when obtaining mass spectra. Waveforms to trap and eject ions from the μCIT array were generated with a Wavetek Datron 195 waveform generator in combination with a Stanford DG535 digital delay/pulse generator. The waveform was amplified with a linear power amplifier and fed into an air-coil inductor that was attached to the μCIT array. The inductor and capacitance of the μCIT array formed a resonant circuit to obtain RF high voltages ranging from 0 to 250 $V_{0\text{-}p}$. Ions ejected from the μCIT array were collected in the detector. The output signal of the detector was amplified with a current amplifier (Advanced Research Instruments Co. PMT5, gain set to 10^6 V/A) and recorded with a Le Croy 9354A oscilloscope. Table I shows detailed experimental parameters.

2.5 Results and Discussions

2.5.1 Fabrication

The fabrication process used to construct the μCIT array was optimized through several fabrication runs and three design iterations. The final thickness of SiO_2 and Si_3N_4 layers were derived during the characterization of the process, by balancing considerations of the fabrication feasibility (such as deposition and etch time), the overall capacitance, and mechanical aspects such as interlayer stress and sufficient robustness of the assembly. One key objective during design development was to keep the capacitance between the endplate and the ring electrode substrate as low as feasible to avoid excessive power dissipation. This led to the concept of etching bulk Si in areas between the ring-electrode cylinders, as shown in Figure 11(a), which was implemented in the final design and reduced the capacitance from 232 pF to 132 pF per half-μCIT array structure. The interlayer stress between the 5 μm thick SiO_2 and 3 μm thick Si_3N_4 was not large enough to cause any significant bending or curling of the Si_3N_4 endplate membranes after SiO_2 release step as shown in the optical profilometer scan, Figure 11(b).

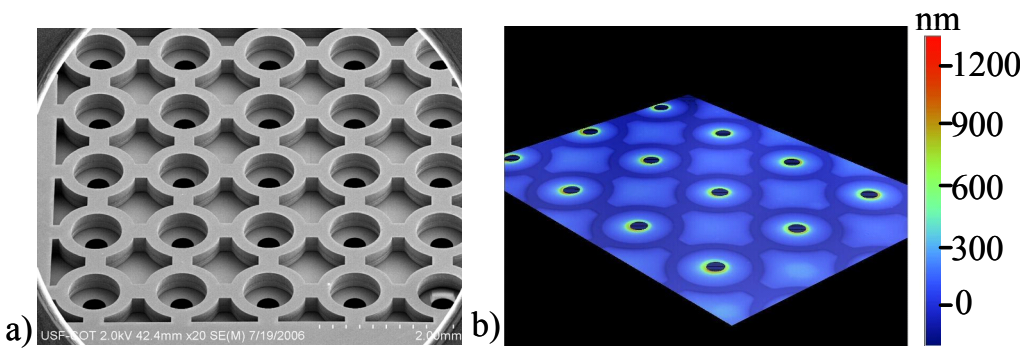

Figure 11 (a) A low magnification SEM image of the μCIT array half-structure showing the ring electrode (top) and the endplate electrode with apertures (bottom); (b) A 3-D surface analysis of the Si_3N_4 membrane showing an outward bowing of 0.6 μm at the aperture edge relative to the membrane.

The surface quality of the cylinder walls was affected due to micron-scale scalloping and undercut of the hard mask (Si_3N_4 and SiO_2) in the Bosch process. Extensive optimization of the Bosch process will be important to obtain desired μCIT geometries and to optimize its

performance. The etch rate per Bosch cycle was a function of the area of Si that was etched, resulting in a micro loading effect that produced varying etch depths with varying r_0 within the same wafer. For this reason, the DRIE etch process was characterized to obtain a verticality of better than 89° of the ring-electrode walls for a predicted optimal r_0 of 360 μm (the z_0 of this wafer was found to be 351 μm, which resulted in the z_0/r_0 to be 0.975). The extent of SiO_2 undercut was determined experimentally.

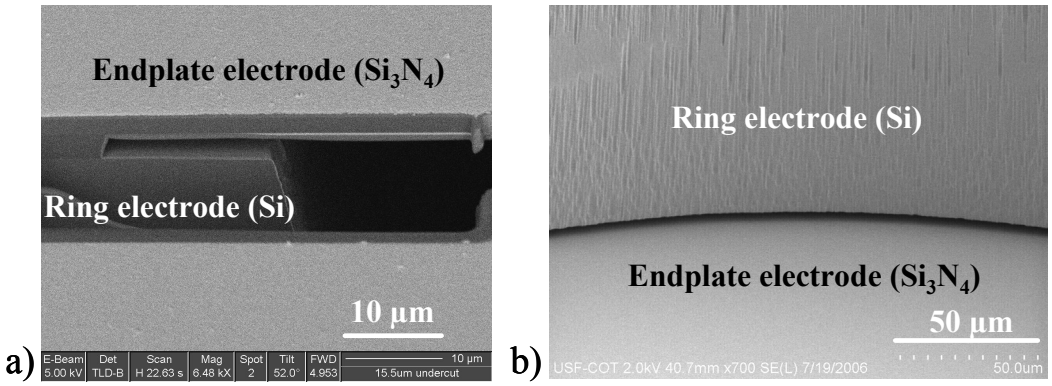

Figure 12 SiO_2 undercut, shown by a) SEM image obtained by cutting the 3 μm thick Si_3N_4 by Focused Ion Beam (FIB); b) SEM image of the inside of the ring electrode.

Figure 12 shows the SiO_2 undercut obtained in 49% HF, which created a "shadow region" and prevented a continuous Cr/Au layer between Si and Si_3N_4 (step G in Figure 10) and maintains electrical isolation of the ring electrodes from the endplates electrodes. The flip chip bonder had a provision for alignment with a 2-μm precision. An offset of 2 μm could lead to shifts in the mass spectral peaks of at most 0.5 Th (see Equation 2).

2.5.2 Experimental

Electronic circuits were optimized to operate the μCIT array using a trapping voltage (V_{rf}) of 10-100 V at 5.5-6.5 MHz. The reasonably low capacitance of the μCIT array allowed for modest power consumption of 7 W and increased operation frequency. The mass range obtainable (50-75 Th) using a single (V_{rf}) scan function was limited by the low potential well depth of the relatively small traps. Larger mass ranges, were investigated by post processing of data from several mass scans, each with increasing start and stop mass. The width (FWHM) of

mass spectral peaks was about 4-5 Th for PFTBA spectra. It is anticipated that mass resolution can be improved by further optimization of the μCIT geometry and/or application of axial modulation (43, 44). Direct introduction of the buffer gas and analyte into the vacuum chamber led to several problems, such as low mass-spectral signal current, detector instability (ion feedback or generation of plasma) and a high gas load on the vacuum system. To rectify these problems, analytes were locally introduced using a capillary to direct the gas influx directly in front of one μCIT endplate. He was used as buffer gas, but did not seem to dramatically increase mass resolution up to the limited achievable pressure of 1 mTorr (mean free path $\lambda \approx 5$ cm).

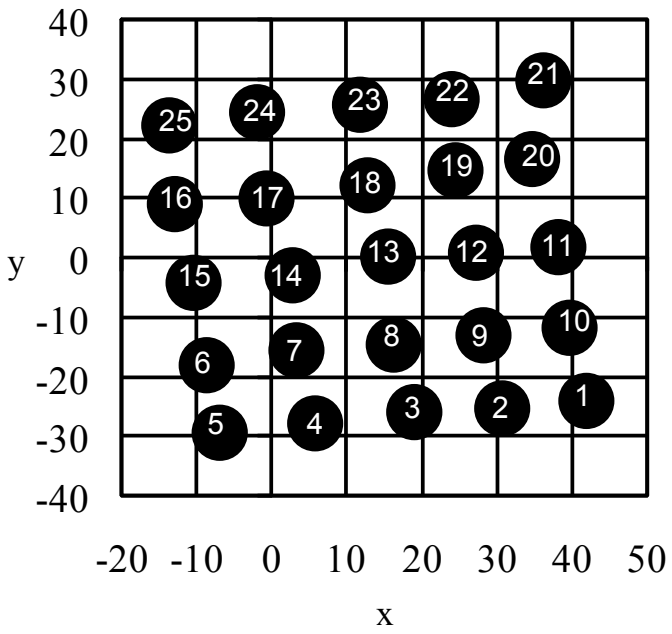

Figure 13 Raster values of electron gun x-y raster deflection plate voltages for optimum transmission of the electron beam through each trap shown in x-y plot. The x and y scales are in voltage applied to the deflection plates of the electron gun.

Figure 13 shows the values of electron gun x-y raster deflection plate voltages for optimum transmission of the electron beam through each trap. Figure 14 shows a small part of a TCE spectrum obtained from μCIT #5 at deflection plate voltages x = -6.9 V and y = -29.3 V. Spectrum 1 was obtained using a trapping voltage of 22 V during ionization and start of the mass instability scan, and spectrum 2 was obtained using an initial trapping voltage of 26.5 V.

The two spectra were combined to create Figure 14. Note that the spike in the signal current caused by switching on the electron multiplier in spectrum 1 and spectrum 2 were removed for clarification purpose.

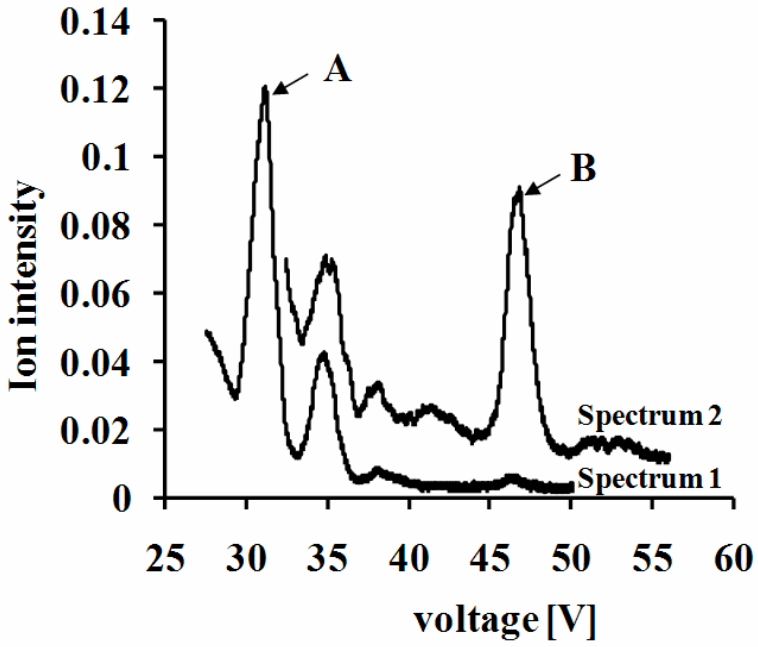

Figure 14 Partial TCE spectrum obtained from μCIT #1 at deflection plate voltages x = -29.3 V and y = 6.9 V. Peak A was assigned to isotope fragment $(C_2ClH)^+$. Peak B was assigned to isotope fragments of $(C_2Cl_2H)^+$.

We have assigned peak A to the mass range 60-63 Th (isotope distribution of TCE fragments $(C_2ClH)^+$) and peak B to the mass range 95-101 (TCE isotope fragments $(C_2Cl_2H)^+$). Using these assignments in Equation 2 yields an A_2 value of 0.74, which is slightly higher than the calculated value of A_2 (0.64) obtained by numerical determination of the electric potential along the μCIT z-axis. Peaks found at 35 V, 37 V, and 42 V are still under investigation. By comparing spectrum 1 and 2 in Figure 14, it can be seen that at low trapping potentials, higher masses have lower signal intensities indicating a limited storage capacity. PFTBA spectra were measured for all traps to obtain the variation in intensities, as shown in Figure 15.

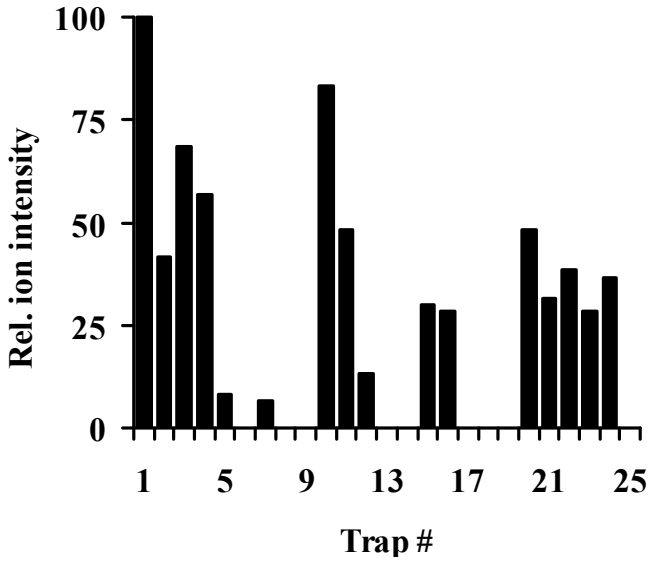

Figure 15 Plot of obtained PFTBA signal intensities for each trap.

We attributed this variation in intensity primarily to the use of a cone-type electron multiplier, in which the gain was highly dependent on location of ion impact. Figure 16, a spatial plot of the measured ion current for each μCIT reflected the cone-type shape and is consistent with our assumption.

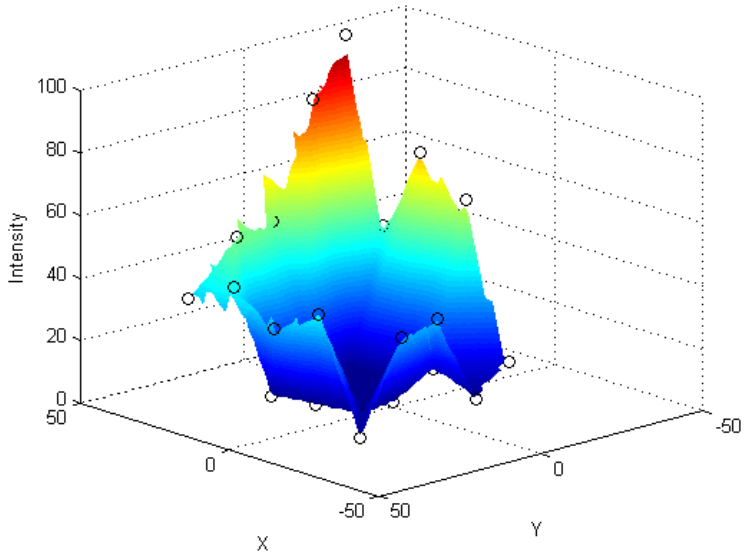

Figure 16 Spatial plot of the ion signal detected in a cone-type detector, illustrating the current gain variation across the cone geometry.

CHAPTER 3

μCIT ARRAY: GENERATION-2

3.1 Abstract

This chapter[2] describes a new fabrication method, simulations, and experimental results for μCIT arrays for use in miniaturized mass spectrometers. The μCIT arrays were fabricated in a silicon-on-insulator (SOI) substrate, and a variety of trap geometries were incorporated into a single μCIT array chip to allow fast iterative measurements of the differences in the mass spectra from μCITs with different ratios of half-axial to half-radial dimensions (z_0/r_0). The chip dimensions were approximately 1.0 cm x 1.5 cm x 0.1 cm. A series of z_0/r_0 were chosen in incremental steps of 3% for each array by changing r_0 from 308 to 392 μm while keeping z_0 fixed at 355 μm, resulting in a range of z_0/r_0 from 1.16 to 0.92 (nine geometries in total).

Simulations were performed in SIMION 7.0 to determine the optimum range of μCIT z_0/r_0 to be fabricated and tested, by producing simulated mass spectra from μCITs with a variety of z_0/r_0 to evaluate predicted mass resolution. Following the simulations, we fabricated the arrays of μCIT geometries in SOI wafers using DRIE to create the cylindrical structures and surface metallization to create ion trap electrodes. Symmetrical arrays of half μCITs were fabricated, diced, and bonded back-to-back to obtain complete μCIT array chips containing all nine geometrical ratios (z_0/r_0), which are referred to in this chapter as the “gradient arrays”. The bonding process provided approximately 5-μm alignment accuracy between the two arrays of

[2] This chapter was published in International Journal of Mass Spectrometry (DOI: 10.1016/j.ijms.2014.06.032). Permission is included in Appendix A.

half μCITs, and the resulting arrays had flat μCIT endplate electrodes with < 3 μm upwards bow. We discuss several critical issues encountered during process development, such as delamination of the buried oxide layer, excessive wafer bow, high capacitance, and ring-electrode wall verticality, along with solutions to mitigate these issues. Mass spectra were obtained experimentally from each trap geometry, and μCIT performance was found to follow the trend with respect to z_0/r_0 observed in the simulations. Experimental efforts indicated that axial modulation on one endplate electrode was required to remove spurious peaks in the mass spectra (caused by higher-order multipole contributions to the trapping electric field), and resulted in mass spectra with full-width-at-half-maximum peaks of 0.4 atomic mass units.

3.2 Background

It is important to develop low-power, potentially handheld, high-performance chemical analyzers to monitor and characterize naturally occurring and man-made chemicals, their (re)distributions and transformations [65]. Mass spectrometry has evolved as a powerful and versatile chemical analysis tool, and has been tailored to fit a broad spectrum of applications. These applications range from laboratory-based clinical measurements, drug testing, analysis of food products, pharmaceutical screening measurements, and environmental chemical analysis. There has been much activity to miniaturize MSs for prolonged in situ measurements at remote or hazardous locations, where it is costly for humans to collect samples and deliver to a laboratory for analysis [66]. For example, field-deployable mass spectrometers (MSs) have been used for in situ measurements of ocean chemistry [67, 68], offsite volcanic monitoring [69], space explorations for biogenic chemical compounds that could indicate extraterrestrial life [70], and studies of comet chemical compositions [71, 72].

Most commercially available portable MS systems are somewhat miniaturized and ruggedized versions of conventional, laboratory-style instruments, which have been tailored for in situ chemical analysis. Further miniaturization based on current technologies gets increasingly difficult, and calls for radically different design methods and new integration

approaches for very small components. Such approaches are necessary to significantly reduce the footprint of all the components, the vacuum housing, and the electronic circuits. Ion trap MSs are a good choice for miniaturization because of their inherent tolerance to relatively high pressures, and because of their scalability without degradation of mass spectral resolution compared to other types of mass analyzers, such as time-of-flight (TOF) MSs and double-focusing sector MSs [73]. Bonner et al. [17] studied the trapping performance of cylindrical ion traps, finding them to generate an effective electric trapping potential quite similar to that of quadruple ion traps (QITs) with hyperbolic electrodes. Thus, for ease of machinability, some groups have chosen to use cylindrical ring electrodes instead of hyperbolic ones, and have demonstrated a similar potential distribution [74] and device performance [75] for certain radius-to-length ratios (r_0/z_0) [53]. It has been shown that as the r_0 of an ion trap is reduced, the corresponding RF voltage required on the ring electrode to scan out an ion drops as the square of the radius, if the RF frequency is held constant. And for a given trap capacitance, the power required drops by the square of the RF voltage. For very small traps, however, the effective potential well depth becomes too small at very low voltages, so the frequency is typically increased to allow operation at higher voltages, and the overall power consumption is increased accordingly [32]. Still, a tremendous power savings can be accomplished by using very small ion traps.

During miniaturization, however, geometrical imperfections, such as surface quality, alignment of the electrodes, and dimensional variations of miniature μCIT MSs, become relatively more prominent, significantly affecting the trap performance [76] . Therefore, it becomes increasingly important to fabricate these miniaturized structures with high precision. At the sub-millimeter scale, conventional machining of metals becomes less practical, especially for complex 3-D structures, and could be expensive, requiring special machining capabilities, such as electrical discharge machining. For a variety of millimeter-scale mass analyzers, several less conventional machining methods have been investigated, such as stereo

lithography of photosensitive resin to build rectilinear ion traps [77], photolithographically patterned metal surface electrodes on ceramic discs to build a halo ion trap [78], and compression molding of low-temperature co-fired ceramics (LTCCs) to build small CITs [59]. Each of these technologies offers a unique set of advantages over conventional machining, depending on the choice of substrate and mass analyzer.

Reducing the size of ion-trap-based MSs also results in lower ion storage capacity, which can lead to lower sensitivity or degradation in mass resolution due to space charge effects (i.e., Coulomb interactions of the ions) if the traps are overfilled. One recent study on the miniaturization of ion traps estimated the total number of analyzable ions scales as the 1.55-1.75 power of the CIT radius [24]. Several groups [79, 80] have proposed building arrays of miniature CITs that can be operated in unison, to make up for the loss in sensitivity of a single miniaturized CIT. In addition, new capabilities offered by arrays of CIT MSs, such as parallel analyses of chemicals, have been proposed and investigated [81].

Another technology that has been applied to achieve extreme miniaturization is MEMS, due to the ease of building extremely miniature structures with high precision. Components and subsystems of the MS system that have been built using micromachining technologies include sub-millimeter ion trap MSs [32, 78, 82-84], a surface microstructure miniature MS [85], time-of-flight analyzers [86] , quadrupole mass filters [87, 88] , Wien filters [89], micro pumps [90], and small electron [91] and ion sources [92]. A complete MS system, fully integrated with the MEMS approach, has also been demonstrated to build a highly miniaturized chemical sensor [34]. The key advantage of the MEMS approach is that it offers high-precision structures and allows integrated assembly techniques that are not achievable by assembling machined metal components. High-aspect-ratio etching, such as DRIE [93], can be used to produce 3-D structures (e.g., cylinders and trenches) in Si. A MEMS approach can ultimately be cost-effective through batch fabrication, since multiple micro-devices can be processed simultaneously on a batch of 100-mm diameter Si wafers. Monolithically designed ion trap

structures could also offer extra mechanical ruggedness and higher alignment accuracy with less stringent assembly requirements [82].

CITs are an ideal candidate for miniaturization and microfabrication due to their relatively simpler geometry compared to quadrupole ion traps with hyperbolic electrodes. A wide range of μCITs with sizes of 1 to 700 μm r_0 have been micromachined over the past decade. One approach was to use iterative sputtering of tungsten to form the trap electrodes of ion traps with 1 - 10 μm r_0. These μm-scale traps were found to have very high capacitance due to close proximity of the trap electrodes [32]. Another group fabricated 20-μm r_0 ion traps in silicon; these traps successfully obtained a mass spectrum of Xenon (Xe) gas from an array [82].

We have investigated and reported on various substrates for fabrication of miniature CITs with high precision. Low-temperature co-fired ceramics [59], ceramics (alumina 99%), and Si wafers [83] are substrates that we have successfully used to construct miniature CITs. This chapter focuses on the fabrication and testing of a new μCIT array design in silicon-on-insulator (SOI) substrates, incorporating a variety of μCIT sizes (r_0/z_0) in each array. The design allowed for faster iterative testing to analyze the trap performance and to identify the optimum geometries. Here we report on the design, simulation, fabrication, and testing of these μCIT arrays.

3.3 Device Design

The design approach adopted to create this generation of μCIT arrays is a derivative of our previous designs [83]. An SOI substrate was chosen instead of Si to: 1) incorporate a thicker endplate electrode for better mechanical ruggedness, 2) incorporate a thicker SiO_2 layer for lower capacitance and higher breakdown voltage, and 3) enable a simpler fabrication process. The wafers were custom ordered from Ultrasil and MEMS Engineering with a buried oxide layer (BOX) of 10 μm sandwiched between a 350-μm-thick Si layer (called “handle Si”) and a 40-μm- thick Si layer (called “device Si”). Figure 17 illustrates the structural details of two chip-scale arrays of half μCITs that were bonded back-to-back to obtain a complete μCIT array.

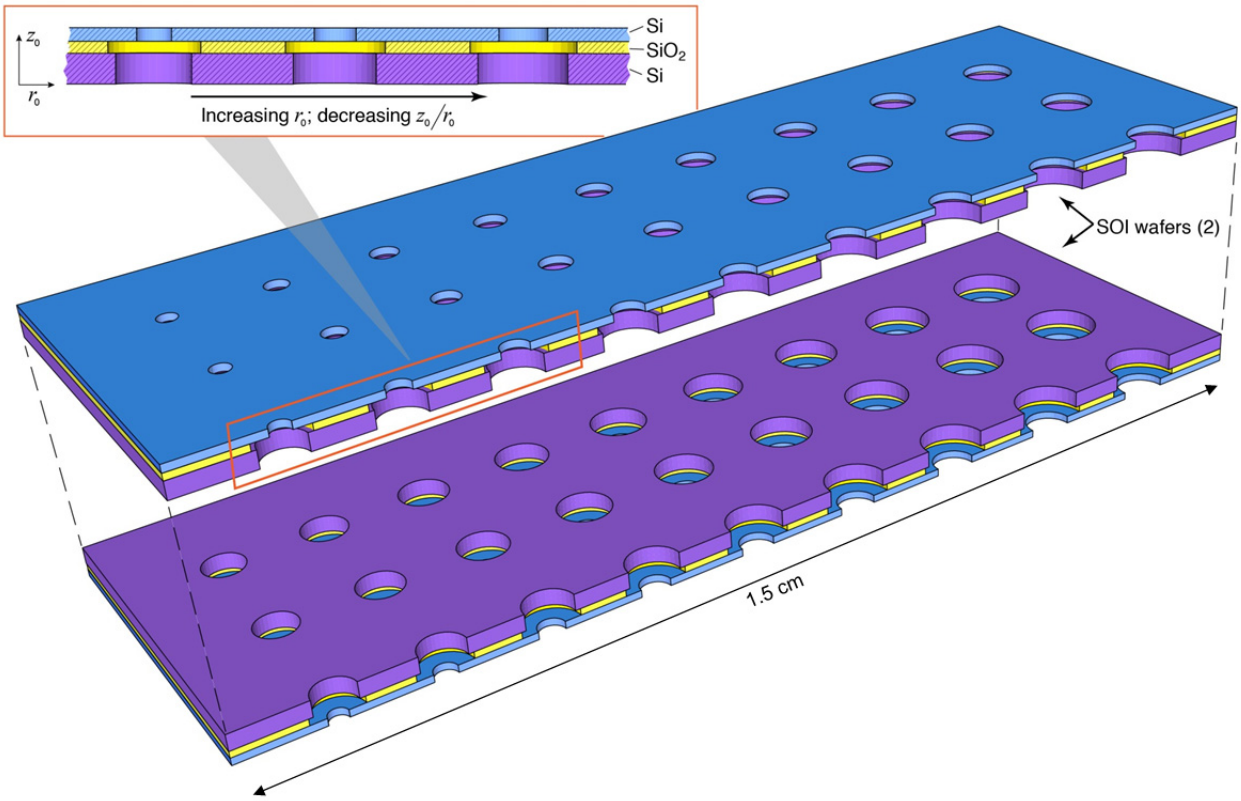

Figure 17 Cross-sectional schematic of the gradient μCIT array fabricated in an SOI substrate.

To fabricate a range of geometries (z_0/r_0) in the same SOI chip, a series of r_0 with a 3% increment in r_0 was incorporated into the mask design. Since the wafer thickness was constant for an SOI wafer, this resulted in a z_0/r_0 range (1.16 to 0.92). Each array consisted of nine columns of three identical traps to investigate the uniformity of MEMS structures and chip boundary effects. To investigate the effect of aperture size on the trapping performance, two sets of the gradient arrays (each with 3 x 9 traps) were incorporated within a single SOI chip: one with aperture size 30% of r_0 and the other with 45% of r_0. The overall footprint of each SOI chip was approximately 1 x 1.5 cm, and fabrication was performed using a 100-mm diameter SOI wafer. Table 1 lists the design details for each gradient μCIT array, where z_0 is the sum of handle Si wafer thickness (z_b) and the gap (d_s) between the ring and endplate electrode, while d_e is the endplate electrode thickness.

Table 1 Design details of the μCIT array

Handle Si thickness (z_b)	350 μm
Device Si thickness (d_e)	40 μm
Buried SiO_2 thickness (d_s)	10 μm
z_0 (z_b+d_s) (Fixed)	360 μm
Radius 1 (r_0 308 μm)	z_0/r_0: 1.16
Radius 2 (r_0 319 μm)	z_0/r_0: 1.13
Radius 3 (r_0 329 μm)	z_0/r_0: 1.09
Radius 4 (r_0 340 μm)	z_0/r_0: 1.06
Radius 5 (r_0 350 μm)	z_0/r_0: 1.03
Radius 6 (r_0 361 μm)	z_0/r_0: 1.00
Radius 7 (r_0 371 μm)	z_0/r_0: 0.97
Radius 8 (r_0 382 μm)	z_0/r_0: 0.94
Radius 9 (r_0 392 μm)	z_0/r_0: 0.92

3.4 Simulations

Simulations were performed in SIMION 7.0 to determine the anticipated spectral quality of a range of trap geometries to guide the design and fabrication of μCIT arrays. For each trap geometry, we generated separate trap files that conformed to the trap designs described in Section 3.3. A user program rendered and randomized the initial conditions of argon (Ar) ions (mass 40) at the start of the simulation. To simulate kinetic cooling of ions through ion-neutral interactions, a hard sphere collision model was used, with He as the buffer gas. The ions were initially trapped and cooled for 4-7 ms by applying an RF potential on the ring electrode, and then ejected using the mass selective instability mode by ramping the RF voltage amplitude. The ion number, mass, and time of flight were recorded and used to generate the simulated mass spectra. This process was repeated for each of the trap geometries. Table 2 shows the simulation parameters used.

Table 2 Parameters used for simulations in SIMION

Frequency of RF potential	7.6 MHz
Initial ion energy	33 meV
Mean free path	700 mm
Collision gas mass	4 amu
RF ramp rate	10 V/ms
Random time of birth	0.9 µs
Random offset	50 µm
Percentage energy variation	50 %
RF voltage	30-70 V_{pp}

3.5 Fabrication

The fabrication approach described in this chapter is a modification of the process described in chapter 2, used to create our previously reported Si-based µCIT arrays [83], to adapt the process for SOI substrates; Figure 18 provides a comparison of the process flows. The fabrication process is briefly described here; a more detailed description is available in chapter 2.

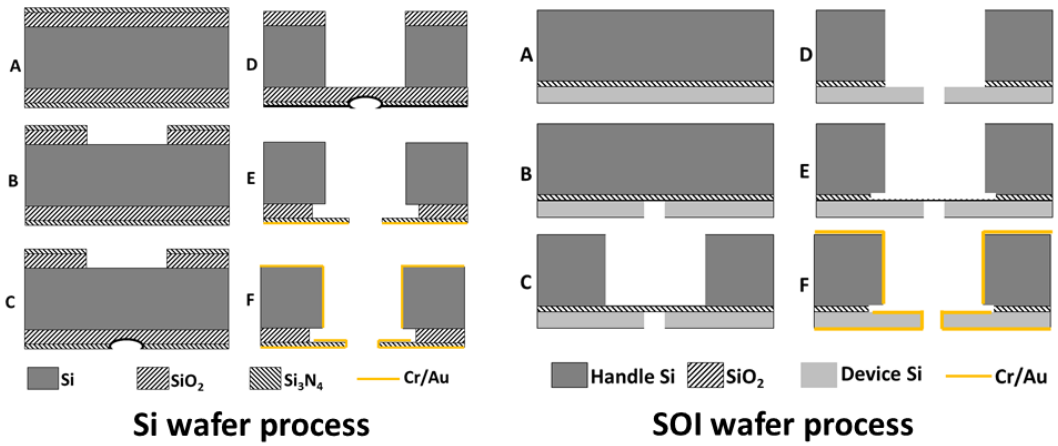

Figure 18 A comparison of the process flow using Si wafer vs SOI wafer.

To etch the endplate in the device Si of the SOI wafer, UV photolithography was performed in an AVG aligner AV620 to transfer the endplate pattern from the optical mask to a

PR layer. Using PR (Futurrex PR1-2000A) as the hard mask in Unaxis DRIE, the device Si was anisotropically completely etched using DRIE in the regions where PR was developed (i.e., removed). This resulted in a cylindrical pattern of endplate apertures in the device Si and exposed the BOX layer. Photolithography was repeated on the opposite side of the wafer using a negative PR (Futurrex NR9-3000PY) to transfer the ring electrode pattern on the handle Si layer. A blanket layer of 120 nm thick aluminum (Al) was sputtered in an AJA ATC 1800 sputtering tool. The developed PR was stripped off using acetone to perform Al lift-off. The patterned Al layer was used as a hard mask in DRIE to etch the handle Si (350 μm) anisotropically using 630 cycles of the Bosch process [93].

At this stage, the BOX layer was exposed from both sides at the bottom of the ring and endplate cylinders. A time-controlled etch in hydrofluoric acid (HF) was performed to remove the BOX layer in the cylinders. This also created a 10-μm undercut in the BOX layer as the HF etch was isotropic in nature. An additional 5-min HF etch was performed to increase the undercut to 15 μm. Later, Cr/Au layers of 50/250 nm were deposited on both sides of this processed SOI wafer, coating the flat endplate layer (device Si), the vertical Si cylinder walls, and the flat handle Si surface to obtain conductive cylindrical geometries. The individual halfCIT arrays were then diced from the wafer in a rotating diamond-blade-type dicing machine (Kulicke & Soffa model) and bonded back-to-back in a “PICO” FineTech flip chip bonder. An optical system was used to manually align the endplate apertures with the ring cylinders using a micron precision stage. Thermal compression bonding of the Au-to-Au layers was performed by compressing the two structures together under 0.8 MPa pressure at 320° C. This resulted in complete μCIT arrays. The individual CIT arrays were tested for electrical isolation between the ring and the two endplate electrodes. Then, capacitance was measured in a probe station using an Agilent 4263B LCR impedance meter.

The fabricated μCIT arrays were mounted on one side of a custom-designed, Au-coated 3.5 x 3.5 cm printed circuit board (PCB) using silver epoxy. The PCB was designed with a

center window cut-out for electron and ion transmission, and had four holes on the four corners for mounting to a custom vacuum flange. Electrical connections from a μCIT array to Au connection strips designed on the PCB were established using wire bonding of a 25-μm diameter Au wire in a wire bonder (Kulicke & Soffa 4524).

3.6 Experimental

Figure 19 illustrates the experimental setup used to test the gradient μCIT arrays. The vacuum system consisted of a custom-designed stainless steel (SS) vacuum chamber (6x4x4 inches^3) with three openings machined to provide for the installation of ISO 63 flanges. A rasterable electron gun (Kimball Physics ELG-2) was mounted on one flange, and the Turbo Pump (Varian V70) was mounted on the second flange backed up by a roughing pump (KNF UN813-4ANI). The third flange held the ion optics assembly, which, when installed, was in line with the electron gun. A metering valve (Cole Parmer M2T1) provided for the introduction of gas directly into the chamber. On the back side of the gradient μCIT array, a chevron stack of micro-channel plates (MCP) (Burle APD 2 MA 18/12/10/12 40:1 MP) was installed to detect ion current.

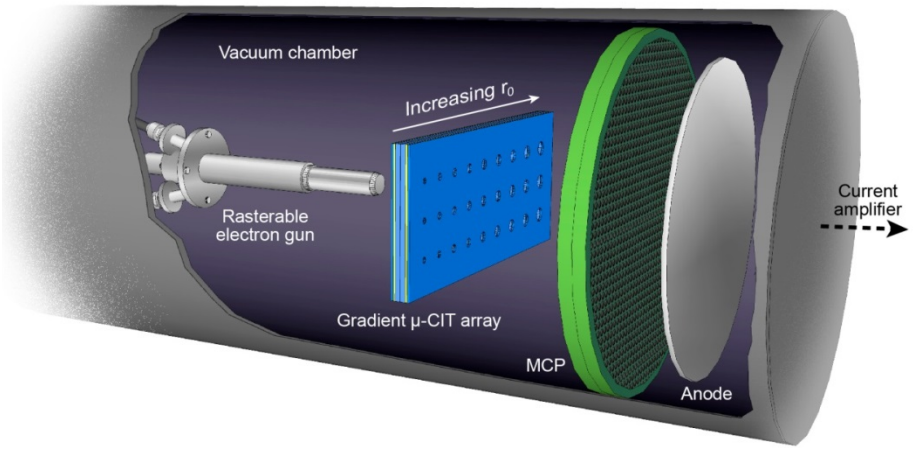

Figure 19 Rendering of the μCIT array mass spectrometer test setup.

The signal from the MCP was amplified using a current amplifier (Advanced Research Instruments PMT-5), which provided a response time of 1.2 μs at an input sensitivity of 1 μA/V. The signal from the current amplifier was recorded on an oscilloscope (Le Croy 9354A) and

saved to generate the mass spectrum in a user-written MATLAB program. A continuous flow of the analyte was introduced into the chamber through a capillary (360-μm od, 50-μm id, 25-cm length), with the exit of the capillary placed close to the μCIT array to introduce analytes near the traps.

To investigate the performance of each trap in the array, the x-y controls of the electron gun were used to direct the electron beam at the center of each trap. Ions were created in the μCITs, one trap at a time, to obtain a mass spectrum from each μCIT separately. The trigger sequence for the ionization cycle, RF voltage ramp, and detector voltage was created using a Stanford DG535 pulse generator.

To create the trapping RF voltage and ramp, a sinusoidal signal was generated by one channel of a waveform generator (Wavetek 195), was modulated in amplitude by a positive ramp signal from another channel, and was then fed into a linear power amplifier. The RF voltage was applied to the ring electrode of the μCIT array using a custom-built inductor coil, which was introduced into the circuit (the μCIT array chip had an equivalent total capacitance of 540 pF) to drive the circuit in a parallel resonance mode. The inductor coil was adjusted to tune the inductance so as to obtain resonance in the frequency range used for simulations. Both of the endplate electrode plates were initially grounded. Ions were ejected sequentially during the RF voltage ramp according to their m/z ratio, and the ion current was detected and amplified by the MCP detector and amplifier.

Axial modulation via monopolar resonance excitation was used to improve mass resolution and to remove spurious peaks from non-linear resonances by applying a small RF signal (in the range of mV) at a fraction of the ion secular frequency (at ejection) to the endplate electrode closest to the MCP detector using another channel of the waveform generator. Table 3 shows a detailed list of the μCIT array operation parameters.

Table 3 Operating parameters for the gradient μCIT array

Frequency of RF potential	7.46 MHz
RF power	4.8 W
Axial modulation frequency	5.67 MHz
Axial modulation amplitude	77 mV_{0-p}
Detector (OFF)	-900 V
Detector (ON)	-1850 V
Total pulse sequence	43 ms
Ionization time	39 ms
RF potential ramp time	3 ms
Ion ejection time	40-42 ms
RF voltage	35-70 V_{pp}
Electron energy	120 eV
Current amplifier gain	10^6 A/V
Helium+ Argon pressure	$3.1x10^{-5}$ Torr
Trichloromethane pressure	$5.5x10^{-5}$ Torr
Krypton pressure	$6.5x10^{-6}$ Torr
Background pressure	$4.0x\ 10^{-7}$ Torr

3.7 Results and Discussions

3.7.1 Simulations

Figure 20 shows several examples of simulated mass spectra of Ar (mass 40) for a series of μCIT geometries with 30% r_0 endplate apertures without using axial modulation. From this selection, it is evident that z_0/r_0 in the range of 0.94-0.97 generates the best spectral resolution and signal intensity. Peaks from non-linear resonances are also visible in the spectra, in which ions are ejected at a q_z in the stability diagram lower than the boundary ejection (q_z =

0.908) [94]. Simulated results from μCIT geometries with 45% r_0 endplate apertures showed similar trends; they are not shown here to avoid redundancy.

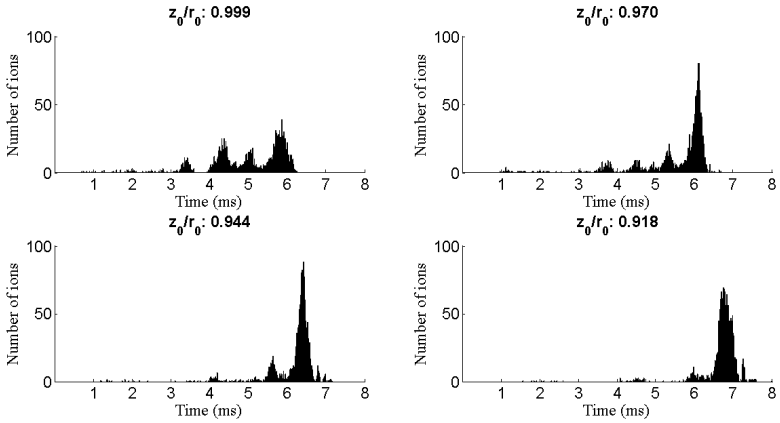

Figure 20 Simulated mass spectra of Ar (mass 40) recorded using a range of μCIT geometries (z_0/r_0: 0.918 to 0.999) without axial modulation.

3.7.2 Fabrication

3.7.2.1 Delamination Issues

As shown in Figure 21, partially floating endplate layers were obtained during μCIT array fabrication in the SOI wafers with a 10-μm BOX layer (purchased from Ultrasil). Initially, we believed that the HF etch rate was higher than expected and had created an excessive BOX layer undercut. However, SEM analysis of a cross-section of the floating endplate region revealed that a delamination occurred at the SiO_2-SiO_2 interface of the SOI substrate.

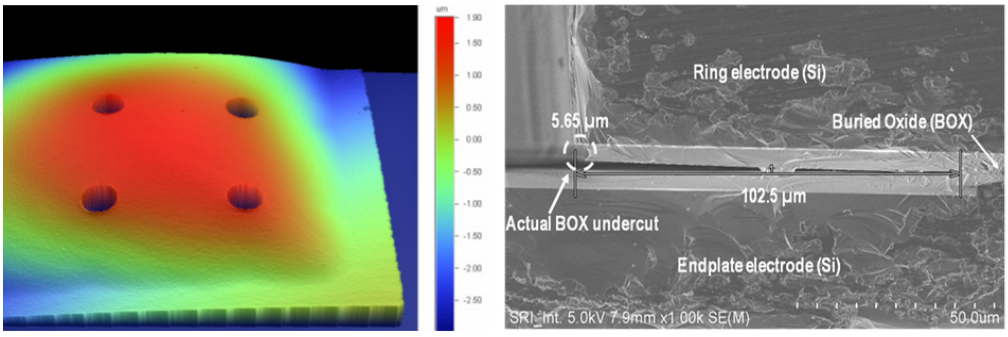

Figure 21 Left: Wyko optical surface analysis shows upwards bow of about 3 μm from the center of each array to the side, indicating that the endplate could be partially (or fully) floating; Right: SEM of an SOI wafer cross-section, diced at the center of a μCIT ring electrode cylinder, showing the delamination between the two BOX layers.

This delamination was related to the vendor fabrication method for these SOI wafers. To form an SOI wafer, one Si wafer is usually oxidized and bonded to another Si wafer using anodic bonding, which is the industry standard. With this approach, however, the BOX layer is limited to 4 or 5 μm in thickness. Since we requested a 10-μm BOX layer, the SOI wafers were made by bonding together two oxidized Si wafers, each with an SiO_2 layer thickness of 5 μm, using SiO_2-to-SiO_2 bonding. This apparently resulted in poor bond strength and high stress between the wafers. Consequently, once the HF etched the first 5 μm of the first BOX layer, it appeared to very rapidly delaminate due to residual stress along the BOX-to-BOX interface.

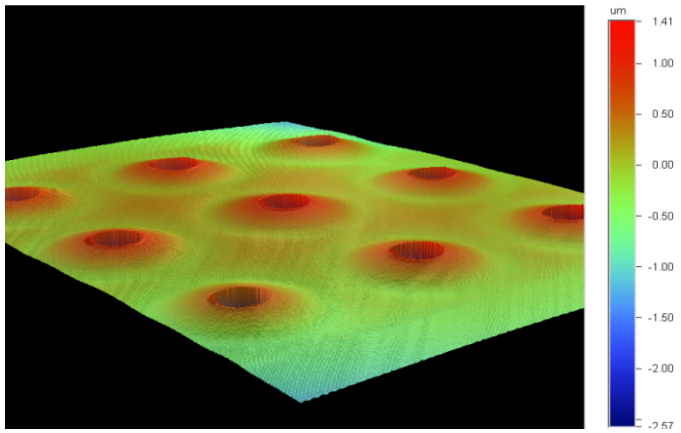

Figure 22 3-D surface profile of the endplate layer, showing that the device Si layer is attached to the handle Si layer by BOX, and showing a slight upward bow at the apertures.

To resolve this issue, the BOX was partially etched up to 4 μm in HF, and the remaining BOX was etched in RIE to avoid lateral etch and rapid delamination. Figure 22 shows the endplate surface profile of the half-μCIT structure created using this method. The half-μCIT structure shows a very flat membrane and a 1-to-2 μm upward bow at the edge of the apertures.

3.7.2.2 Excessive Wafer Bow

Another issue with the 10-μm BOX layer wafers was an excessive bow in each wafer. These wafers had a 5-μm backside thermal oxide (TOX) layer that was not required for our process, so it was removed during processing. During fabrication of the μCIT arrays using these SOI wafers, the bow increased to about 200 μm when the TOX was removed, leading to significant problems during the second lithography. To overcome this problem, the TOX layer

was not removed for subsequent wafers, and instead was used as the hard mask for the through-wafer DRIE process.

3.7.2.3 μCIT Array Capacitance

Due to limited BOX thickness, which separated the endplate and ring electrode surfaces, and the larger overall size of the gradient array compared with our previous designs [95], the capacitance was expected to be higher for these devices. The measured capacitance of the gradient array chips was approximately 540 pF. It would be desirable to achieve a larger dielectric gap between the endplate and ring electrode surfaces to reduce the capacitance, but with this fabrication approach, the gap was limited by the thickness of the BOX layer. A way to achieve a larger separation between these components would be to use three substrates, two for the endplate electrodes and one for the ring electrode, and then create a large stand-off by bulk etching much of the Si in endplate substrate, leaving much smaller surfaces for bonding the three components together.

3.7.2.4 Fabrication Tolerance

Radii of etched ring electrode cylindrical structures were measured with an optical microscope to compare with the designed radii in the optical mask. Optical microscope measurements indicated a 3-μm increase in the radial dimension, which was attributed to the combined effect of diffraction in thick PR during photolithography, and a hard mask undercut in DRIE. The result was a micromachining tolerance of about 0.4% of r_0.

3.7.2.5 DRIE Wall Verticality and Roughness (KOH)

Although the DRIE Bosch process is anisotropic, the verticality of the walls depends on factors such as the loading effect (how much area is being etched), the aspect ratio (the etch depth to width ratio), and the type of etch stop layer used [93]. Cylinder walls with an angle greater than 89° were observed in the ring electrode structures etched using the Bosch process. Residual Si whisker-like particles observed at the end of the DRIE step were typical of the DRIE

process when etching deep topography. A short KOH etch of 30 s was used to successfully remove the Si whiskers.

3.7.2.6 Bonding Alignment Accuracy

Two arrays of half μCITs are shown in Figure 23 next to a USA nickel coin for size comparison. These were then bonded back-to-back to form a complete μCIT array chip.

Figure 23 Left: Optical image of the two symmetrical μCIT array half-structures before bonding. Right: Complete μCIT array obtained after bonding the two arrays of halfCITs mounted on an Au-coated PCB substrate.

The overall alignment accuracy of the endplate apertures and ring electrodes depends on two steps: (1) the alignment accuracy of the ring electrode pattern to the endplate pattern established by backside alignment during the second photolithography step (typically ±2-3 μm), and (2) the alignment accuracy of the two half arrays of μCITs when bonded together in the flip chip bonder (typically ±5 μm). The second alignment step was also critical to obtain continuous cylindrical walls inside the ring electrodes at the interface of the two half-ring electrodes, and to align the two endplate apertures axially with the ring electrode. Since the flip chip bonder uses a microscope and an XYZ stage, the alignment accuracy tends to be dependent on how well the structures are aligned by eye when looking into the microscope. Figure 24 shows the depth profile of the μCIT array with the two arrays of half μCITs bonded together. Figure 24 (left) shows an example of poor alignment, indicated by the reflection (in blue) off the edge of the lower endplate aperture during depth profile.

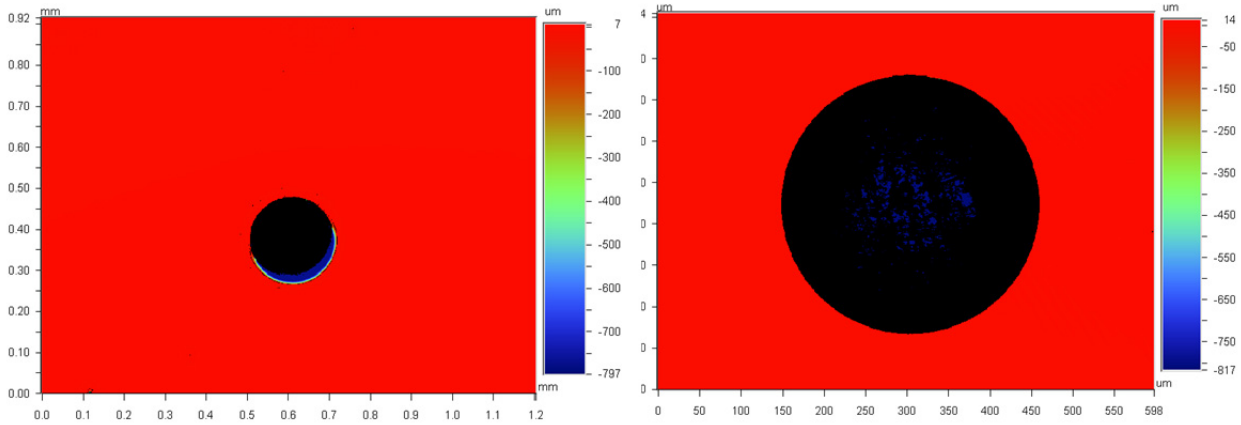

Figure 24 Depth-profile performed using an optical profilometer from the top endplate aperture to the bottom aperture to investigate the alignment of the two bonded arrays of half μCITs. Left: example of bad alignment; Right: example of good alignment at higher magnification.

Figure 24 (right) shows an example of good alignment, indicated by the absence of the edge of the bottom aperture, suggesting that the two apertures and the ring electrode are well aligned within ca. 5 μm with respect to each other.

3.7.3 Measurements

A series of Ar spectra were obtained by directing the electron beam at the center of each trap in the gradient μCIT array. The relatively high capacitance (540 pF) of the gradient array μCIT chips limited the voltage that could be applied to the ring electrode at the RF frequencies required, due to the limited output power of our RF amplifier (6 W) and the LC resonance circuit used in these experiments. Thus, the upper mass range attainable was approximately 50 amu. Table 3 shows the experimental parameters used to obtain the spectra shown in Figures 25 through 29.

Figure 25 shows the spectra obtained from each trap in a gradient array (with 30% r_0 endplate apertures) without axial modulation. The RF voltage during the RF ramp (35-70 V_{pp}) at the time of Ar ion ejection was recorded to be 52 V_{pp} These experimental results show similar trends to the simulated results in Figure 20, indicating that the z_0/r_0 ratio 0.97 provides mass spectra with fewer spurious peaks from non-linear resonances created by higher-order

multipoles in the electric potential distribution inside the trap. This indicates that this z_0/r_0 ratio most faithfully reproduces the potential distribution of a quadrupole ion trap with hyperbolic electrodes.

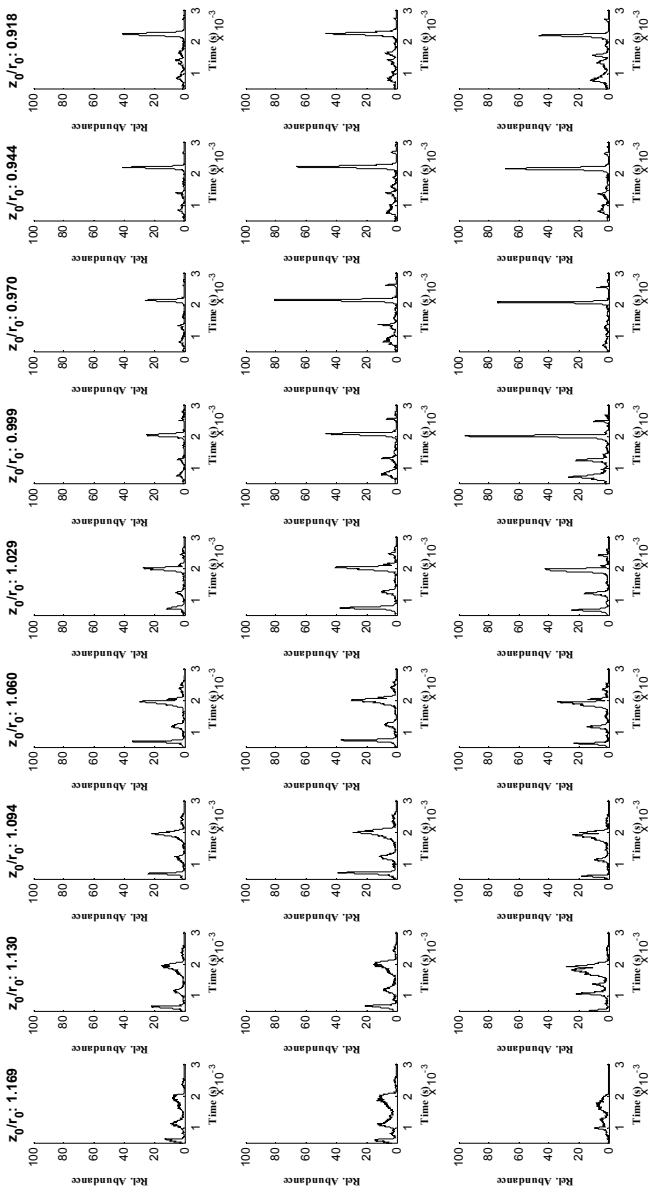

Figure 25 A series of Ar spectra obtained without axial modulation from each trap in the gradient μCIT array with the 30% r_o aperture size.

Figure 26 shows the mass spectra from the three traps with z_0/r_0 = 0.97 (taken from Figure 25) overlaid on the same graph.

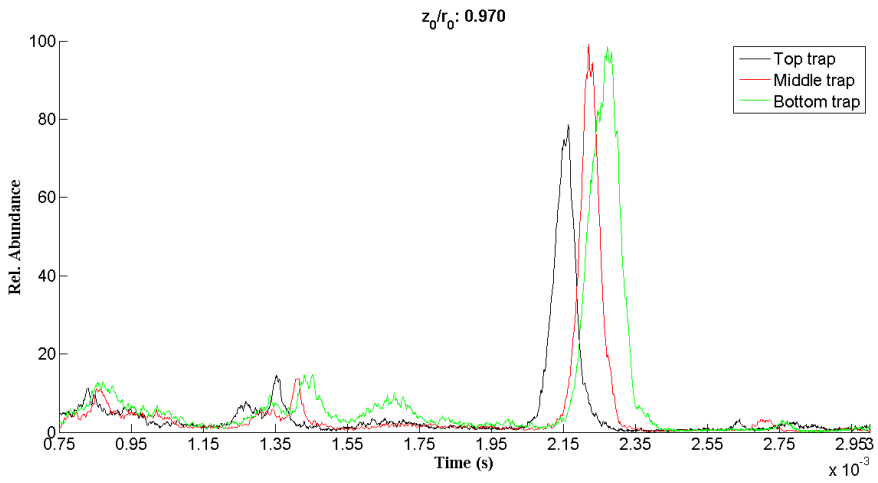

Figure 26 An overlap of Ar mass spectra obtained from the three traps with the same z_0/r_0, showing a time shift in the spectra.

These traps should yield identical results, but instead show a time shift in the spectra. The relative time shift is believed to be caused by a slight misalignment in the bonding process and an inherent non-uniformity associated with the micromachining process used to fabricate these structures. Figure 27 shows the series of Ar spectra obtained using axial modulation on one endplate.

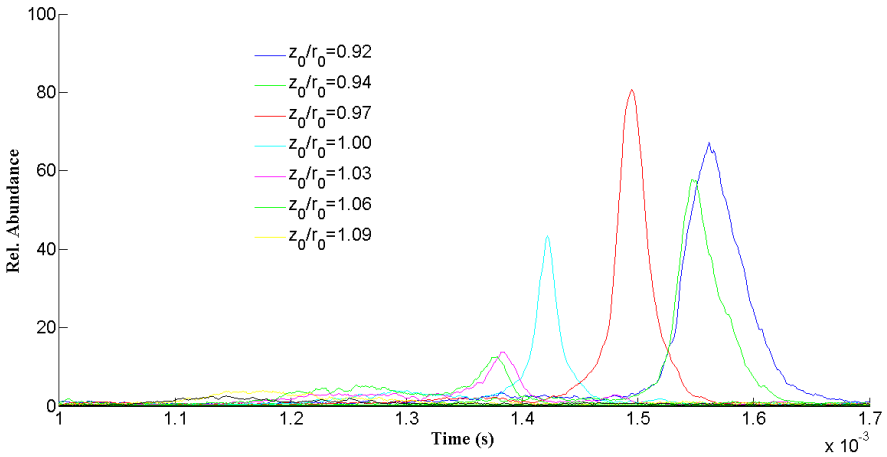

Figure 27 Experimentally obtained spectra of Ar for a range of z_0/r_0 in the gradient μCIT array using axial modulation.

These experimental results corroborate previous findings [83] that predict the optimum geometry to be $z_0/r_0 \approx 0.97$. Figure 28 shows a mass spectrum of doubly charged krypton (Kr^{2+}) obtained from a μCIT with $z_0/r_0 = 0.97$ using axial modulation. The spectrum shows clearly

resolved stable Kr isotopes, and also contains peaks from the residual gas in the vacuum housing.

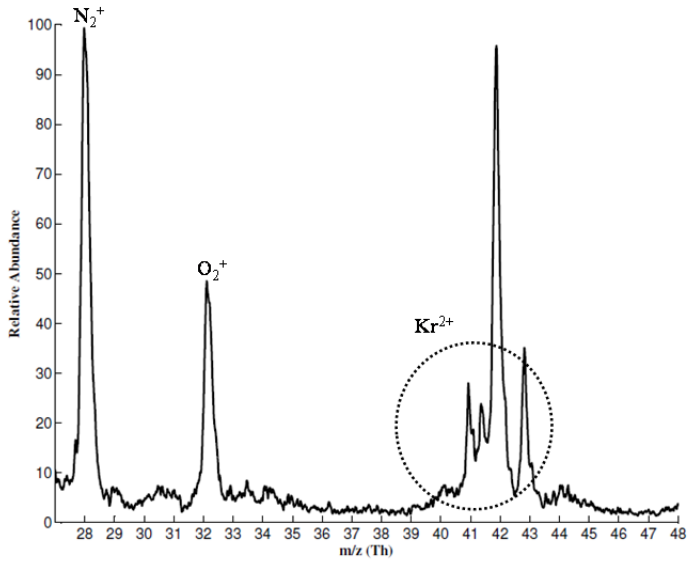

Figure 28 Experimental mass spectral data from a single trap (z_0/r_0 = 0.97) in the gradient μCIT array. Axial modulation was used to obtain better-than-unit-mass resolution. Doubly charged krypton ions correspond to masses 82, 83, 84, and 86.

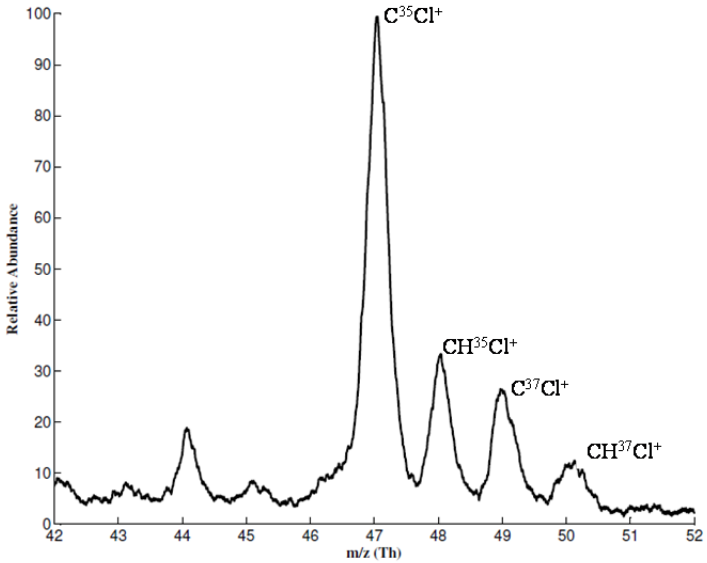

Figure 29 Partial mass spectrum of TCE, showing the stable isotopes of chlorine.

Figure 29 is the mass spectrum of fragments of trichloroethylene, showing the stable isotopes of chlorine (^{35}Cl and ^{37}Cl).

3.8 Conclusions and Future Work

This chapter describes a novel design and fabrication method for creating μCIT arrays for use in miniaturized mass spectrometers. A series of z_0/r_0 were incorporated into each μCIT array chip for rapid and efficient testing to determine optimum μCIT geometries. Experimentally obtained spectra indicate a better-than-unit-mass resolution using axial modulation in mass-selective instability mode in a single trap. These results compare well with simulations presented here and previously. Although design requirements of such high-precision sub-millimeter structures are well met using MEMS technology, issues like excessive stress and wafer warp induced by thick SiO_2 layers on Si need to be carefully accounted for in the design structure. The μCIT array chips had an undesirably high capacitance, which was attributed to a large area of overlap of electrodes and extremely close spacing, as dictated by the current design and by limitations of oxide layer growth. From the SOI process development, we learned that it is critical to know exactly how the starting substrate was fabricated to avoid undesirable effects during processing.

Future improvements in μCIT array designs and processing methods should address capacitance, voltage breakdown, and alignment issues. A three-wafer design, in which endplate electrodes and ring electrodes are fabricated separately and bonded together, could address all of these issues. Large areas of the endplate electrodes could be bulk-etched to increase the gap between the endplates and ring electrodes, while leaving only small areas with a small spacing for bonding. The larger gap will decrease overall capacitance and increase breakdown voltage. Also, by forming each ring electrode in a single wafer, alignment precision can be less critical. In the reported approach, a misalignment would significantly distort the electric field at the center of each trap. To further increase sensitivity for a given μCIT array “footprint”, traps could be packed more closely (e.g., in a hexagonal orientation). This would also help to reduce capacitance, since there would be less bulk Si in the ring electrode chip. Better alignment

accuracy can be attained by using dedicated alignment marks for the flip chip bonding process, or by using passive alignment via mechanical locking structures.

Furthermore, to compensate for possible geometric variations across the array and the resultant shift in the spectra among identical traps, it would be beneficial to detect ion currents from each trap independently. Post-processing of the ion currents from individual traps could minimize this shift to obtain high-resolution mass spectra. A multi-anode detector array can be designed to accomplish this. Lessons learned from this generation of μCIT array are being used in ongoing work to design a high-density μCIT array for a lower-power, higher mass-range μMS.

CHAPTER 4

PLANAR ION FUNNEL

4.1 Abstract

The novel planar ion funnel (PIF) design presented in this chapter[3] emphasizes simple fabrication, assembly, and operation, making it amenable to extreme miniaturization. Simulations performed in SIMION 8.0 indicate that ion focusing can be achieved by using a gradient of electrostatic potentials on concentric metal rings in a plane. A prototype was fabricated on a 35 x 35 mm custom-designed PCB with a center hole for ions to pass through, and a series of concentric circular metal rings of increasing diameter on the front side of the PCB. Metal vias on the PCB electrically connected each metal ring to a resistive potential divider that was soldered on the back of the PCB. The PIF was tested at 5.5E-6 Torr in a vacuum test setup that was equipped with a broad-beam ion source on the front and a MCP ion detector on the back of the PIF. The ion current recorded on the MCP anode during testing indicated a 23x increase in the ion transmission through the PIF when electric potentials were applied to the rings. These preliminary results demonstrate the functionality of a 2D ion funnel design with a much smaller footprint and simpler driving electronics than conventional 3D ion funnels. Future directions to improve the design and a possible micromachining approach to fabrication are discussed in the conclusions.

[3] This chapter was published in Review of Scientific Instruments (DOI: 10.1063/1.4897480). Permission is included in Appendix A.

4.2 Background

A variety of methods for sample ionization and the efficient transfer of ions into mass analyzers have contributed to the widespread use of mass spectrometry in chemical, biological, and medical applications. The use of ion optics to efficiently transport ions is a critical component in the construction of many types of analytical instruments involving ionization methods, such as electrospray ionization mass spectrometry [96], ion mobility spectrometry (IMS) coupled with mass spectrometry [97-99], laser ablation [100], in-vacuum matrix-assisted laser desorption ionization (MALDI) [101], atmospheric pressure MALDI [102], Fourier transform ion cyclotron resonance [103, 104], and subambient ionization in quadrupole mass spectrometry [105]. The operation and efficiency of such ion transfer optics directly impact overall sensitivity [106] and could impact the resolution of the analytical instrument, as is the case for IMSMS [99]. Some examples of ion transmission devices are skimmers, inlet multi-capillary tubes[107], RF-only multipole ion guides [108, 109] and a combination of these passive and active transmission components [110]. One of the more important functions of ion optics in such instruments is to transport the ions by “funneling” them from a broad-beam source into a more narrowly defined beam to efficiently introduce the ions into an analytical device, such as a mass analyzer [100], to obtain higher sensitivity. Ion funnels are also used to transport ions from a high-pressure region into a lower-pressure region, using a differential chamber vacuum housing, as is often used in a field-deployable ion trap mass spectrometer [111].

Ion funnels provide a major improvement in ion injection efficiency and have become more prevalent at the front end of different types of mass spectrometers, where conventionally, a small orifice, commonly called a skimmer, is used to limit the conductance between different vacuum stages. The most popular design of an ion funnel, derived from the stacked radio frequency (RF) ion guide [112], uses a set of concentric annular plates of decreasing diameter, stacked together with a spacer, forming a funnel-like 3D cone geometry. The ions are funneled by applying either an electrostatic (DC) [97] or by a combination of electrodynamic RF potentials

and DC potentials [113, 114]. Transmission efficiencies of near 100% have been demonstrated in simulated models and validated through experiments at intermediate pressures of 1-20 Torr [115]. Using the popular 3D conical stack of electrodes, a passive ion funnel at atmospheric pressure has also been reported [116]. It makes use of isolated annular plates of decreasing diameter. Ion focusing is achieved by the potential generated when the charge builds up on the electrodes as they are exposed to the ion flux.

This chapter reports on an electrostatically driven PIF that was constructed in a two-dimensional plane, making it amenable to further miniaturization. Instead of the conventional method of stacking a series of annular plates of decreasing internal diameters, a series of concentric rings, with successively smaller diameters, patterned on a single substrate, was used to focus the ions towards a center ion transit aperture. A voltage divider circuit soldered onto the back of the plate was used to apply a gradient of potentials on each successive concentric ring to generate the potential distribution in front of the concentric rings. The use of a gradient of electrostatic potentials to focus the ions in high vacuum applications simplifies the driving electronics and circuitry, but it is expected that the PIF could also be driven with RF potentials making it applicable to low to medium vacuum (>1 mTorr) applications as well. In the following, we present the simulations, fabrication approach, test setup, and performance analysis of the PIF prototype. Potential methods for optimization and future directions are discussed in conclusion.

4.3 Simulations

The design of the PIF was initially modeled and simulated in SIMION [117] ion optics software to investigate the focusing effect on low-kinetic-energy (KE) (5-10 eV) ions of atomic mass number 28 to represent N_2^+. The scale of dimensions for the model was chosen considering the scale of the ion source and ion detector to be used to test the prototype PIF, and also to ensure a realistically achievable PCB design with reasonable cost to show proof of principle. The model consisted of a series of seven concentric electrode rings with decreasing

internal diameter, each 0.4 mm wide, with a gap of 0.4 mm between each successively smaller ring. The inside diameter of the smallest ring was 3.6 mm, resulting in an opening with a spot size of 3.6 mm for ion transmission. A user program was written to apply a geometric series of DC voltages. The lowest voltage of 2 V was applied to the smallest ring and the highest voltage of 128 V was applied to the largest ring. Figure 30 illustrates the PIF model developed in SIMION, and the potential contours when the potentials were applied using the user program. Three annular plates were incorporated on the right side (exit) of the PIF, with independent potential control, to further collimate the ion beam transmitted through the center hole of the PIF. Ions were created 10 mm to the left of the PIF as a group spread across an area of 6 x 6 mm, symmetrically placed along the center axis of the PIF, with an initial KE of 5 eV in the direction normal to the PIF plane. As the group of ions was initialized, trajectories were recorded as shown in Figure 31 (left). Figure 31 (right) shows the potential energy contours across the model as the ions traversed from left to right. To investigate the acceptance angle, a series of simulations were performed by progressively increasing the incident angle of the ion flux with respect to the PIF plane. A Gaussian 3D distribution was used as the initial ion flux (1000 ions). Acceptance angles up to 1.17 steradians resulted in higher than 33% ion-transmission efficiency, for ion spot-size of 1 mm at a distance of 1 mm past the ion-transmission aperture. The focal length of the transmitted ions was dependent on several simulation parameters such as initial KE energy, angle of incident, ion mass and the gradient and amplitude of voltages applied on PIF electrodes. It is also expected that the focal length would be relatively less dependent on PIF design factors such as electrode spacing, number of electrodes, electrode thickness etc., as long as a comparable potential gradient was applied across the PIF electrodes.

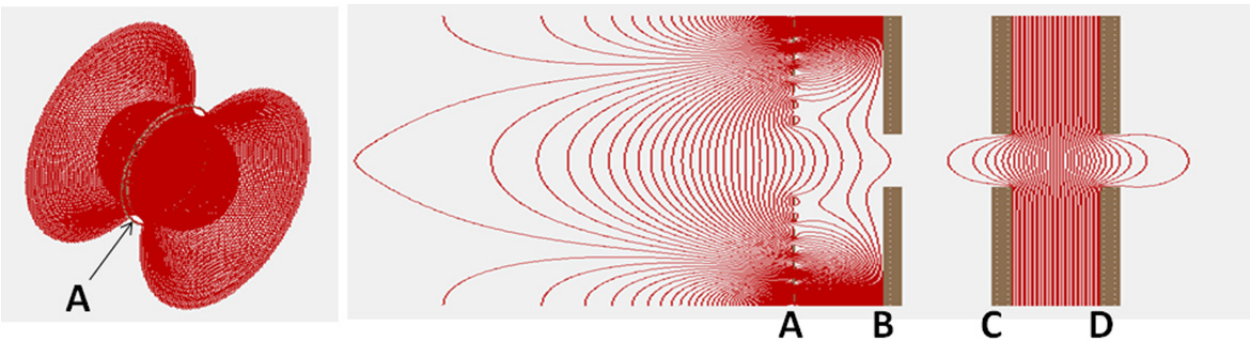

Figure 30 Left: 3D isometric view of the potential contours due to the gradient of voltages applied on the PIF electrodes (A) Right: Cross-sectional view of the PIF electrodes (A) and collimating lenses (B, C, and D) generated in SIMION, showing the potential contours.

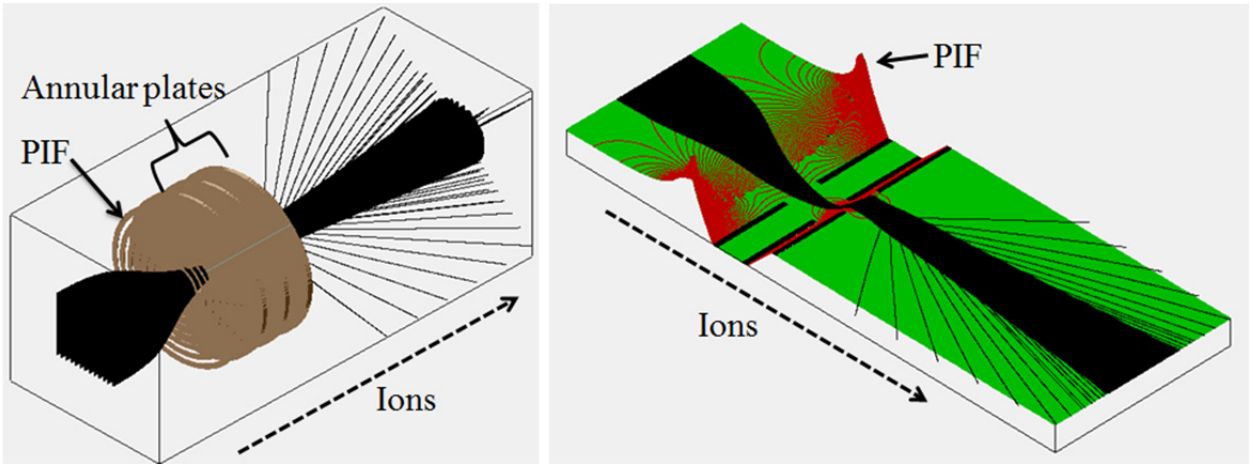

Figure 31 Left: 3D screenshot of ions being funneled by the PIF and the collimating lenses in SIMION; Right: Potential energy view of the PIF model, showing the gradient of potential energy across the concentric rings to illustrate the focusing effect.

4.4 Fabrication

Figure 32 shows the prototype PIF, which was constructed using a custom-designed, 1.6-mm- thick PCB (FR4 substrate) with leadless solder finish for the metal rings. The overall PCB was designed to be 35 x 35 mm^2 with four holes (1.6 mm dia) on the corners for mechanical mounting and alignment with other Kimball Physics eV parts used in the vacuum test setup. Figure 32(a) shows the front side of the PIF with the center hole for ion transmission, ten concentric metal rings of decreasing internal diameter, and the ground plane. While the simulated PIF design has seven rings, the actual prototype has ten rings instead of seven to leave room for increasing the area of ion flux, if needed. Through-hole metal-filled vias were

incorporated into the design to electrically connect each concentric metal ring to a voltage divider circuit on the back side of the PCB, as shown in Figure 32(b). A network of resistors was used to obtain a geometric distribution of potential on the series of concentric rings. Surface-mount resistors of appropriate values were soldered to the PCB, and the rest of the metal on the front side was grounded to reduce the area of the non-conductive surface (FR4 material) exposed to the ion flux to keep the charging of the PIF as low as possible.

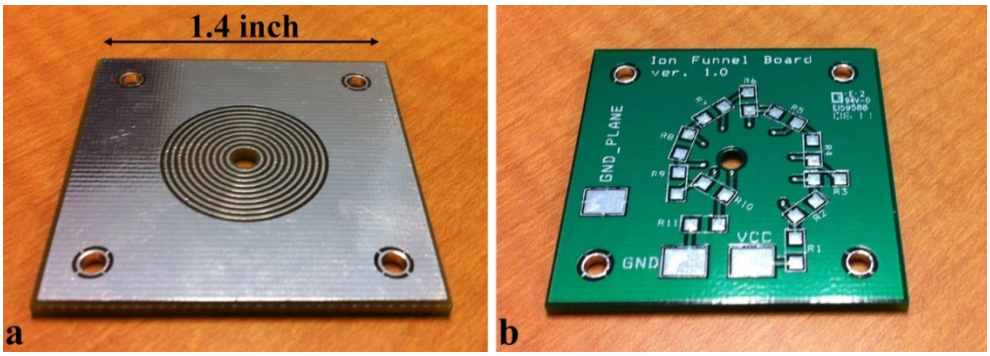

Figure 32 The PIF constructed for proof-of-principle tests. (a) Front side of the PIF, showing the concentric rings with the center ion transmission hole and the outside area plated with metal to form the ground plane. (b) Back side of the PIF, showing the voltage divider circuit and test points.

Since the PIF was constructed on a PCB substrate, it was suspected that the insulating surface (0.4 mm wide) between the rings would charge up if it were exposed to the ion flux. Although it would be ideal to have a highly resistive layer to dissipate the charge while maintaining a potential gradient across the concentric rings, the authors did not have strong reasons to believe that this would significantly impact the performance of the PIF. If the funneling is efficient, then the ions will not reach the PIF surface and will be constantly redirected towards the center hole by the potential established via a potential gradient on the concentric ring. The charge dissipation, however, would be critical for applications where the PIF needs to be operated in a pulsed mode. In that case, the insulating surface could be coated with a highly resistive layer, such as Germanium, which would bleed excess charge to ground while maintaining the potential on the rings.

4.5 Experimental

The PIF was tested under vacuum at a background residual gas pressure of 5.5E-6 Torr. The test setup was built to fit in a 6 x 4 x 4 inch^3 aluminum (Al) vacuum chamber with a turbo molecular pump (ATH 30+) and a roughing pump installed to obtain a background vacuum level of approximately 1E-7 Torr. The vacuum chamber top plate was equipped with four NW16KF electrical feed-throughs, including two high-voltage vacuum feed-throughs and a micro ion gauge (Granville-Phillips 354002-YD-T) to measure low pressures. A metering valve was used to introduce the gas for ionization into the vacuum chamber.

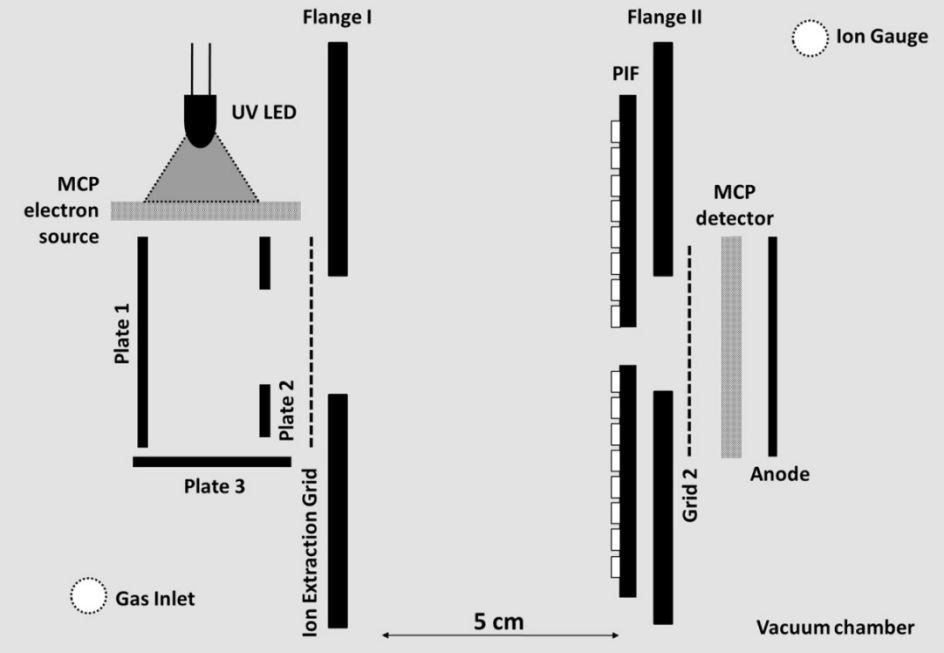

Figure 33 Cross-sectional rendering of the segmented test setup used to verify the performance of the PIF. The section on the left contains the broad-beam ionization source and the ionization cell, the middle section contains the PIF, and the section on the right contains the ion detector assembly.

All the components were installed on two custom-designed Al flanges, as shown in Figure 33, mounted onto the top vacuum chamber flange, and were designed to divide the inside of the housing into three separate chambers: the ionization chamber, the PIF chamber, and the ion detection chamber. This separation ensured that any ions reaching the detector had to pass through the PIF center aperture. Holes (12.5 mm dia) were machined in the center of

the two plates for ion transmission, while the other regions where the flanges were cut out for sufficient gas conductance were covered with a fine nickel mesh (222 LPI) to avoid electric potential penetration from one section to the other.

To generate a broad beam of ions in the ionization chamber, a broad beam of electrons was generated by using a deep ultraviolet (DUV) range light-emitting diode (LED) (SET Inc. UVTOP255) coupled with a chevroned stack of two MCPs (Burle APD 2 MA 18/12/10/12 40:1 MP). This approach to generating electrons has been previously tested in our lab. A DUV LED packaged in a TO-39 with flat window, with a beam divergence of 60°, was used to illuminate the entire active area (18 mm diameter) of the MCP to generate a broad beam of electrons. The front side of the MCP was biased at -1870 V while the potential at the back side of the MCP was adjusted relative to ground to produce most electrons in the 60-70 eV energy range, since this is the energy typically used in electron impact ion sources. The ionization cell was constructed using Kimball Physics stainless steel plates (plates 1, 2, and 3), as shown in Figure 33. In a separate experiment, plate 3 was connected to a picoammeter (Keithley 6487) and the average current measured by collecting the electrons generated by the MCP was recorded to be 4.8 μA. A grid was installed to extract and accelerate the ions from this cell towards the PIF. The ionization chamber design and the voltages required to generate a broad beam of ion flux with a low KE range was assessed by simulating the ionization chamber in SIMION. For plates 1, 2 and 3 biased at 5V and the ion extraction grid at -5V and a 3D Gaussian distribution of ions across the volume of the ionization chamber, with initial KE 33 meV, an ion flux with average KE of 6.9 eV, median KE of 7 eV and a standard deviation of 0.9 eV was generated and directed towards the PIF. Out of 1000 simulated ions, 92% of the ions were extracted.

The PIF was installed on flange II, as shown in Figure 34. The voltage divider circuit and connections on the back side of the PIF are not shown for simplicity. The length of the ion flux path in the test setup was kept longer than that in the simulated model to investigate the use of lower voltages for focusing the ions. To validate the simulated configuration for the experiments,

as mentioned in Section II, only seven of the ten rings were connected to the voltage divider, and the remaining three rings were attached to the electrical ground.

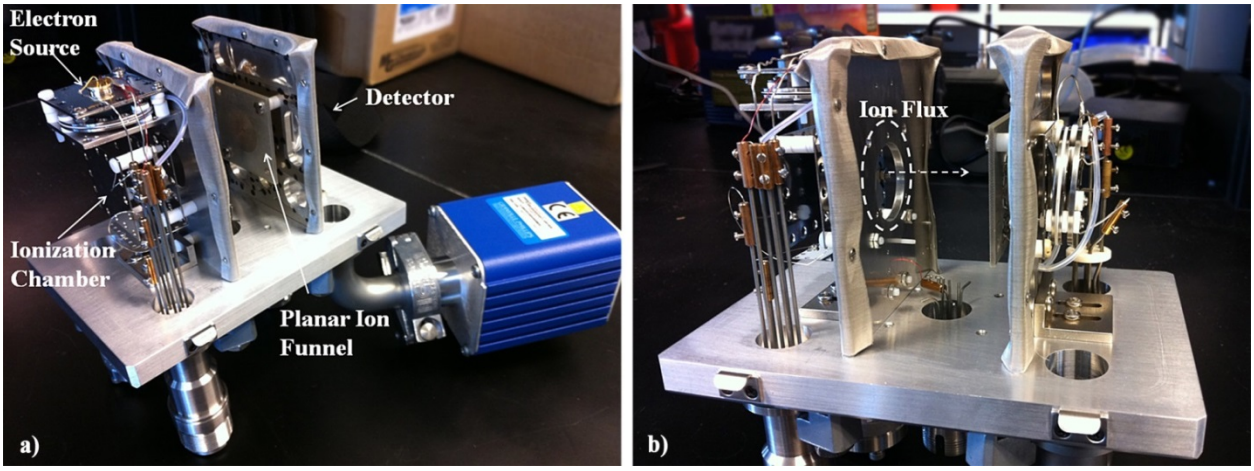

Figure 34 a) Test setup, showing the components mounted on the two Al flanges, which are installed on the top vacuum flange. The top vacuum flange is inverted from its normal configuration when installed on the vacuum chamber. b) Test setup outside the vacuum chamber, showing the path of ion flux from the ionization chamber to the PIF.

4.6 Results and Discussion

The performance of the PIF was determined by comparing the total ion flux measured at the anode with the voltages on the PIF electrodes off, and then on at various magnitudes. The two experiments were performed in direct succession to minimize changes in operating conditions, such as background pressure, temperature, and electron flux. Air was introduced into the chamber through the needle valve, and the valve position was adjusted to keep the pressure stable at 5.5E-6 Torr. Since the background gas was air, it is believed that most of the ions formed through EI were N_2^+ and O_2^+. The DUV LED was operated at 5% duty cycle with a pulse period of 10 ms. A potential of -5 V was applied to the ion extraction grid to extract the ions towards the PIF chamber.

Figure 35 shows the ion signal recorded on the anode with increasing voltages applied to the PIF electrodes. With PIF voltage off (0 V), and hence the entire PIF substrate grounded, a very small amount of ion flux was detected by the ion detector.

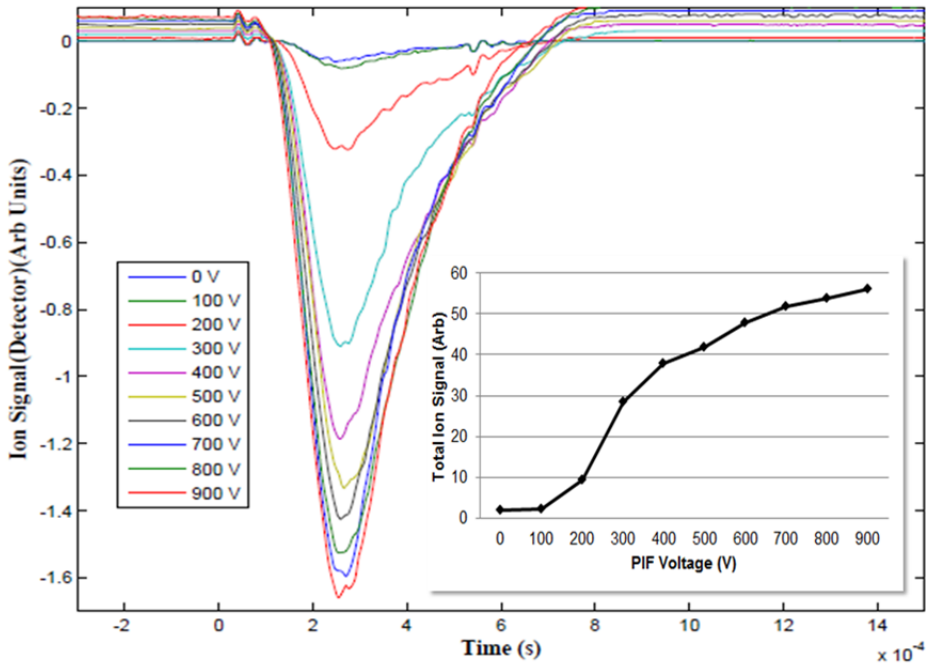

Figure 35 Ions detected as they are focused towards the center of the PIF and traverse through the center ion transmission hole for a range of voltages applied to the PIF. The signal increased as the voltage was successively increased from 0 to 900 V. A maximum signal enhancement of 23x was observed at 900 V. Inset Figure: Area under the curves representing the total ion signal detected for each successively higher potential applied to the PIF outside ring. Maximum gain was observed when the potential was increased from the 100 to 400 V range.

With the voltage supply at 100 V, a potential of 100 V was applied to the largest ring (the seventh, in this case) and geometrically lower voltages (by a factor of 2) were applied on each successively smaller ring. The increase in the detector signal indicated that substantially more ions traversed through the center hole of the PIF with increased PIF voltages. The focusing effect increased with higher voltages applied to the electrodes. Figure 35 (inset) shows the total area under the respective curves. The ratio of the ion signal detected with PIF off and with PIF on (with a maximum voltage 900 V) was measured to be about 23x. Coincidentally, the ratio of the area of the center hole to the total area spread for the seven concentric rings was calculated to be about 25. Any further incremental increase in the maximum voltage above 900 V did not further increase the signal, indicating that most of the ions were being funneled at 900 V. Increasing the voltage beyond 1200 V actually decreased the ion signal. One cause of the

decrease could be that the potentials on the rings were high enough to start repelling ions, so they did not reach the PIF transmission aperture in the center of the PCB.

4.7 Conclusions

A novel PIF has been developed, and initial experiments indicate a strong focusing effect for low-energy ions. Signal increase of up to 23x has been measured using DC voltages of up to 900 V on the outer ring. The design and operation of the PIF provide an easy path to miniaturization, due to its small form factor and simple construction by mounting focusing rings and the electronic circuitry on a single substrate. Such a design, with careful optimizations, could possibly replace the larger, more conventional 3D ion funnels. Further optimization of the design, by using a more compatible fabrication technology, such as micromachining processes, is also possible. One way to achieve this would be to construct the PIF on a silicon (Si) wafer by sputtering a highly resistive layer on Si, similar to the germanium layer used fabrication of 2D "halo ion traps" [57, 118], to generate a gradient potential rather than a series of discrete concentric rings. This would also further simplify the electronics, since no voltage divider circuit would be required. In addition, since the PIF focuses ions with different KEs at different locations along the axis, the PIF could also be used as an energy filter. The possibility for further miniaturization, along with the simpler setup and operation of a PIF, make it a compelling choice to be an integral part of miniature analytical instruments for efficient transport of ions.

CHAPTER 5

ONGOING WORK AND FUTURE DIRECTIONS

5.1 Ongoing μMS Development

5.1.1 Summary

The primary objective of this collaborative research between SRI International (SRI) and Goddard Space Flight Center (GSFC) is to demonstrate the capabilities of an entirely new class of micro-mass spectrometer (μMS) instruments for use as chemical analyzers in space flight missions.

The objective of this research is to adapt μMS technology for detection of molecules of interest to astrobiology and to demonstrate the μMSs' ability to measure higher-mass molecules (up to 250 atomic mass units). Figure 36 shows a μMS, which will collect interplanetary dust particles and gases from cometary coma on a sample collector plate. Gases can be continuously sampled. After the sample isolation chamber (SIC) interlock is closed, the sample collector plate can be heated slowly, to desorb molecules with lower vapor pressures from the plate or from dust particles collected on the plate, for analysis. Upon desorption of the chemicals, molecules flow into an array of μMSs, where they are ionized with a special electron ionization source using UV light. The ionized molecules are then mass analyzed and detected by a MCP with a multi-anode system. We will demonstrate the μMS prototype instrument's ability to detect and characterize water and compounds of prebiotic relevance, such as those emitted from jets or forming on the surfaces of comets. The proposed instrument will weigh 1000 g; its size will be 10x10x10 cm^3 with a SIC of 1x1x2 cm^3, and it will have a low power consumption of 4.5 W.

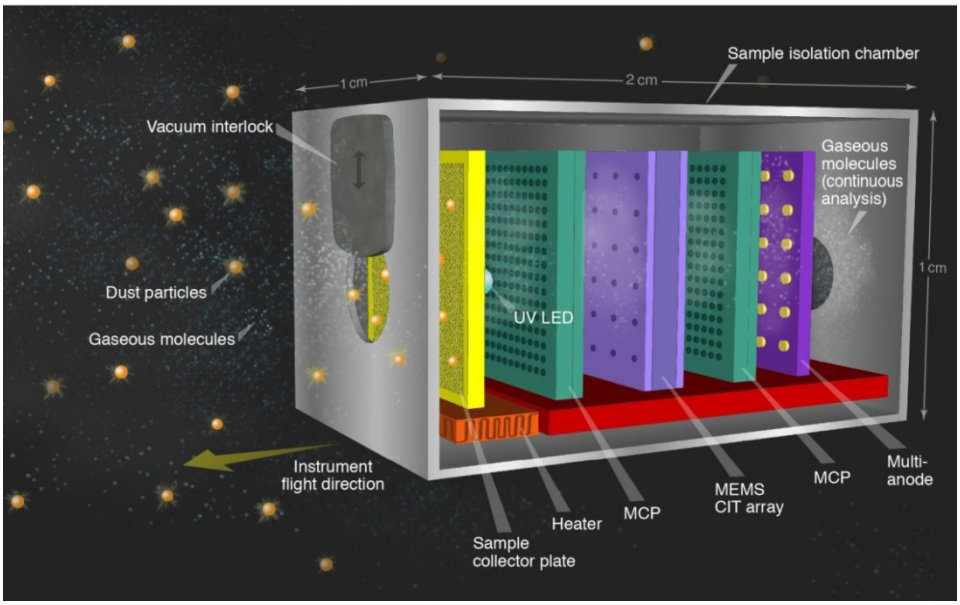

Figure 36 μMS cometary sampling concept device.

5.1.2 Simulations

Ion optics simulations were performed in ion optics software SIMION 8.0 to investigate two aspects of the μCIT geometry.

5.1.2.1 Simulation 1: Optimum Geometry (z_0/r_0)

For a fixed 60-μm gap between the endplate electrode (EE) and ring electrode (RE), a series of simulations were performed for a range of r_0, keeping z_0 constant. This series allowed us to measure and compare mass spectra for z_0/r_0 ranging from 0.92 to 1.26.

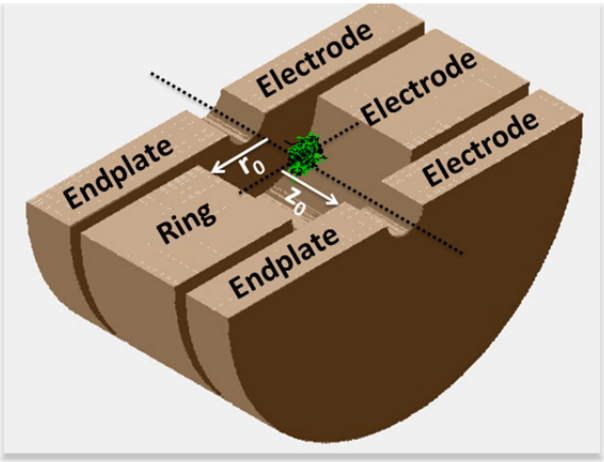

Figure 37 μCIT model in SIMION.

5.1.2.2 Simulation 2: Effects of Etched Wall Verticality

The motivation to investigate the effects of verticality is that the wall of the cylindrical hole of RE etched in Si using deep reactive ion etching (DRIE) tends to have a slight angle instead of being exactly 90°. Adjusting the process conditions in DRIE allows us to obtain near 90° (almost vertical), but in some cases, 88° and 86° were also measured at GSFC. Beside the DRIE conditions, the angle is also affected by any change in the mask or the type of substrate. To understand the effect of varying wall verticality, a series of simulations was performed (Figure 38) using the most optimal ratio as identified by simulations in section 5.1.2.1. The angle was varied from 90° to 80° in steps of 2°, and the simulated mass spectra were recorded for ions ejecting on both sides of the μCIT model.

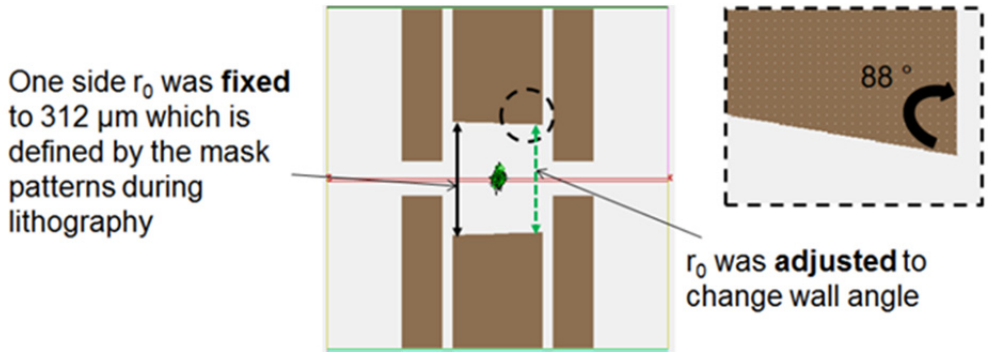

Figure 38 Modeling the μCIT geometry in SIMION for varying cylinder wall verticality simulations.

5.1.3 Fabrication

A three-electrode integration approach was adopted to build a complete μCIT array chip at NASA GSFC. This approach allowed flexibility in the range of gaps that could be incorporated between the three electrodes. The gap is a critical design aspect of the μCIT array and dictates the operational specifications of the μCIT. A 60-μm gap was chosen to avoid electrical breakdown due to high electric fields caused by anticipated particulate contamination and RF voltages required to operate the μCIT chip.

The fabrication process was broadly divided into three process steps – RE fabrication, EE fabrication, and bonding – to form the complete μCIT array chip as shown in Figure 39

(right). Bulk etching in Si was performed using DRIE for all three CIT electrodes. To obtain a μCIT array chip design with low capacitance and high electrical breakdown between the three electrodes, a 2 μm thick silicon dioxide (SiO_2) layer was thermally grown on all 3 electrodes followed by a selective metallization step. The micromachined and metallized electrodes were bonded together in a flip chip bonder using optical alignment. The obtained μCIT chip was packaged and delivered to SRI for testing.

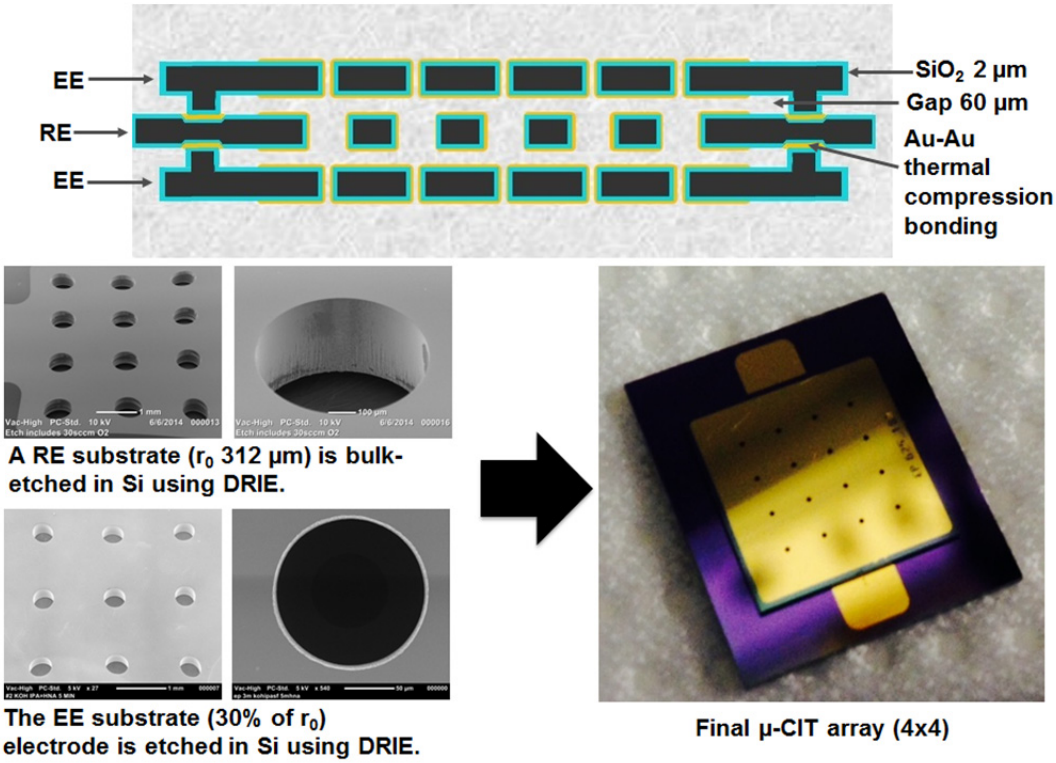

Figure 39 (Top) Cross-sectional view of the μCIT chip; (Left) SEM of etched structures in Si; (right) optical image of a complete μCIT array chip.

5.1.4 μMS Architecture

We implemented the μMS design in a high-vacuum test setup to build an operational MS system. All ion optics components were incorporated in a custom-designed ULTEM 2100 package (later to be replaced with ultra-high vacuum- compatible ceramics) with the volume of 10 cm^3. Figure 40 shows the 3D model of the μMS integration approach and the μMS test setup built to be fitted into a conventional vacuum chamber for preliminary characterization. All ion

optics components inside the μMS package were designed to be stacked together, aligned by the inside corners of the ULTEM package, and lightly compressed with four set screws.

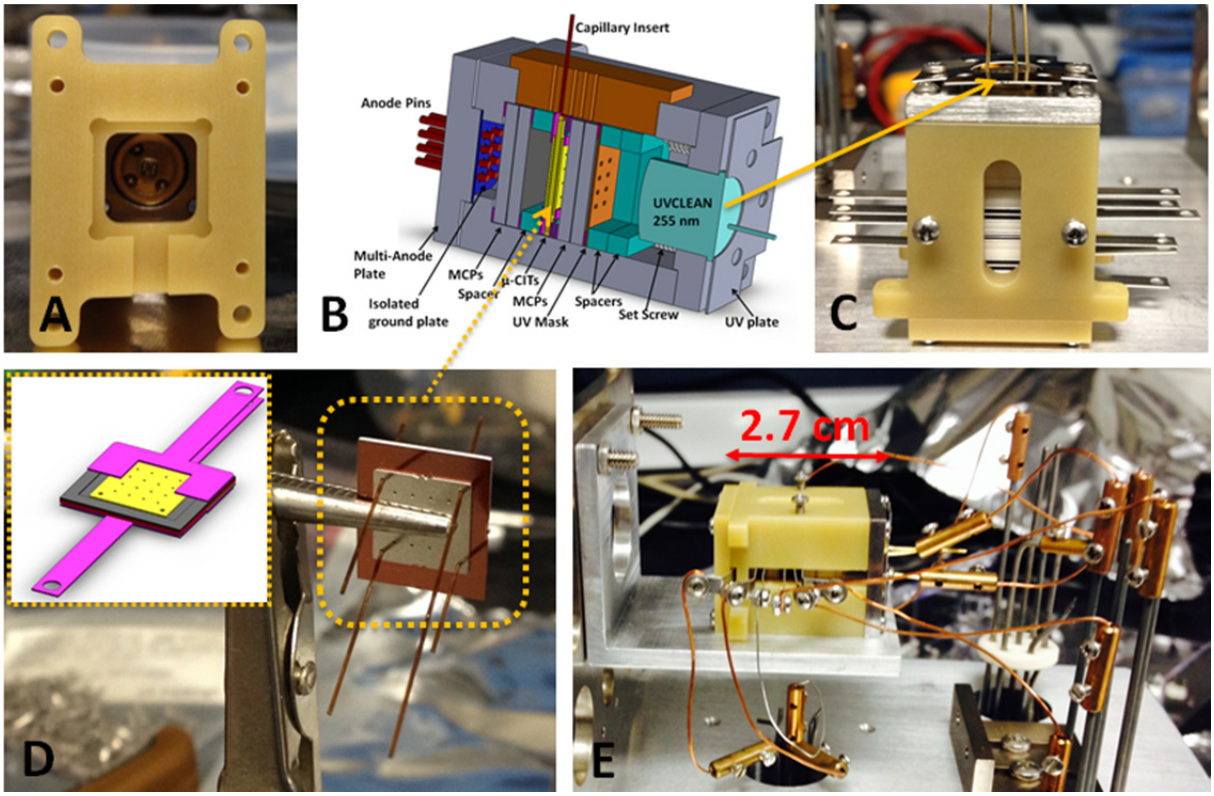

Figure 40 A) UV-LED fitted inside the μMS package; B) projection views of the μMS package with a cross-sectional view showing all the components; C) all components and electrical connectors installed in the μMS package; D) stainless steel CIT array assembled together using capillary-based mechanical alignment; E) integrated μMS assembly installed on the top flange of the vacuum chamber.

5.1.5 μMS Test Setup

To ultimately perform ultra-high-vacuum (UHV) measurements emulating conditions on a cometary mission, an HV system was built using a 6-inch 6-way stainless steel cube with conflat (CF) flanges. A 300 l/s turbo molecular pump (Agilent 304) backed by a scroll pump (Agilent IDP3) was installed as the pumping system. A custom-designed CF was built with electrical feedthroughs required to apply the range of voltages and waveforms to perform complete MS operation in the mass-selective instability mode. The CF flange included two sub-miniature version A (SMA) connectors for RF voltages to the electrodes of the μCIT array chip, two 9-pin sub-d connectors for miscellaneous low-voltage signals for

UV LEDs and grids, one 25-pin sub-d connector for detecting the signal from each trap independently, one 4-pin HV (5KV/5A) connector for applying high voltages to MCPs, and one 1/16 Swagelok connector for analyte introduction into the vacuum chamber. Figure 41 shows the UHV test bed with the details of the custom 6-inch CF flange in the inset. A full-range pressure gauge was installed to measure the pressure down to 1E-10 Torr. A minimum pressure of 2E-10 Torr was observed so far.

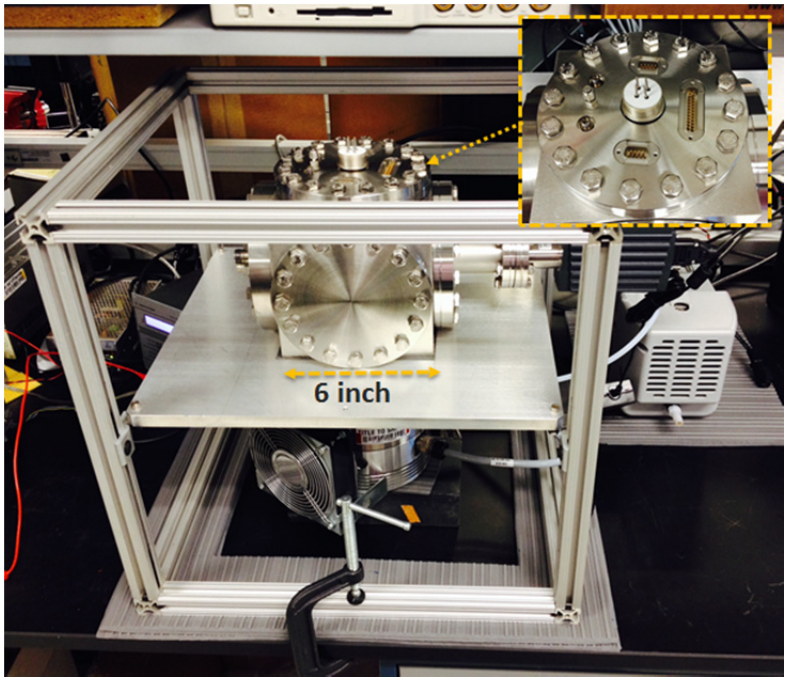

Figure 41 The UHV test setup installed and operational at 2E-10 Torr.

5.1.6 Preliminary Results and Discussions

5.1.6.1 Simulations

5.1.6.1.1 Simulation 1

Figure 42 shows the series of simulated spectra obtained by trapping and performing mass-selective instability ejection of 2000 ions each of 40 and 45 amu for a range of z_0/r_0 CIT models. The ions were cooled via collision cooling using He buffer gas for about 1.5 ms. Simulated spectra indicate z_0/r_0 in the range 0.96 to 1.02 is optimum.

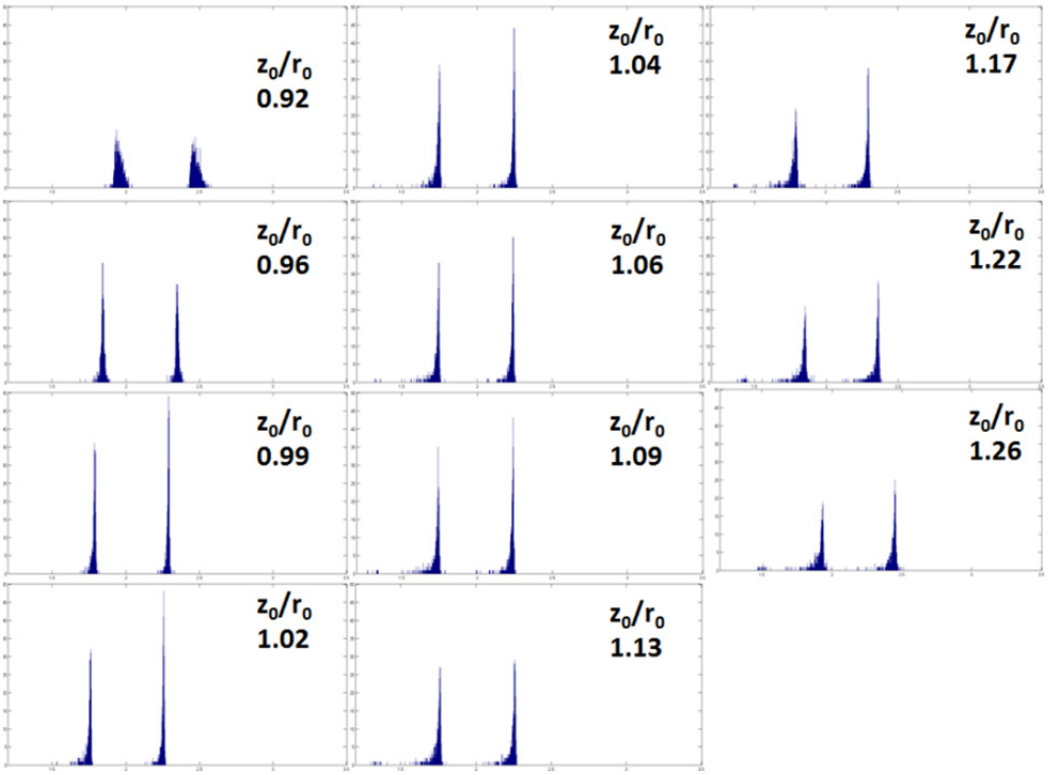

Figure 42 Simulated spectra for a range of trap geometry (z_0/r_0).

5.1.6.1.2 Simulation 2

The series of simulations with varying cylinder wall angle in RE indicated a preferential ejection of ions from the larger diameter side of the RE. Figure 43 shows the trend of preferential ejection for varying cylinder wall angles. It is noticeable that the preferential ejection is significant for angles smaller than 88°. This is critical during MS test setup integration. The electron source is mounted on one side and the detector is mounted on the other side of the μCIT array chip. The 88° and 86° cases can be advantageous (more ions detected as compared to a perfect 90° cylinder wall) if the μCIT array is mounted with the right orientation; i.e. if the electron source is mounted on the tapered side of the μCIT array chip. No noticeable degradation of simulated spectra quality was observed in this series of simulations. An invention disclosure titled “3D ion trap optimized for preferential ejection” has been filed to cover this new finding.

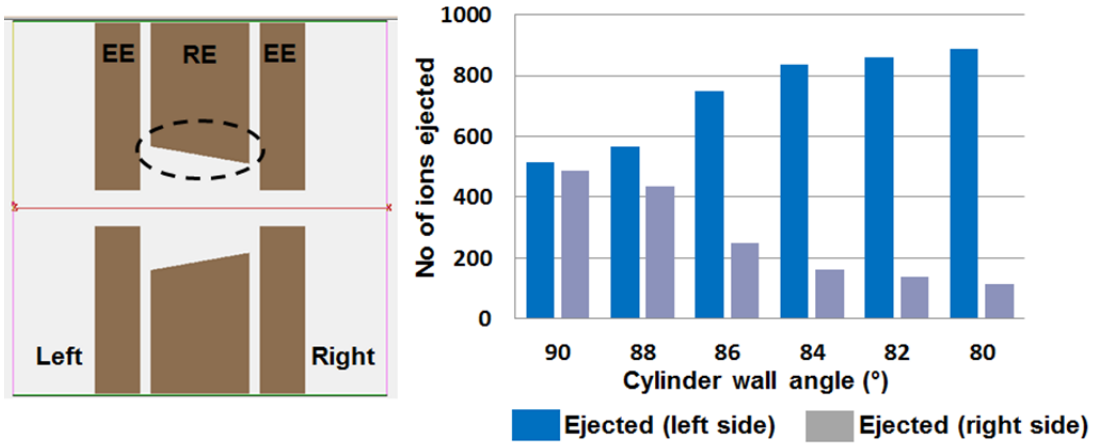

Figure 43 (Left) Cross-sectional view of the CIT model; (right) trend of preferential ejection with varying cylinder wall angle. Total ions simulated: 1000.

5.1.6.2 Fabrication

5.1.6.2.1 Electrical Isolation

The three electrodes were electrically isolated from each other, meaning that no electrical short occurred during the bonding or packaging process.

5.1.6.2.2 Electrode Alignment

The μCIT array chip was analyzed under the microscope to verify alignment across the chip. The optical mask used to fabricate the electrodes also incorporated Vernier calibration marks that were etched on the electrode surface and were visible under the microscope. Figure 9 shows the microscope images of some of these Vernier marks. It was observed that some sides were better aligned (~6 μm) than others (~20 μm). With the flip-chip bonder used for alignment and bonding, a repeatable alignment accuracy of 5 μm is expected. This bonding process and alignment features will be optimized to achieve a targeted, repeatable alignment of <5 μm.

5.1.6.2.3 Bonding Strength

As the μCIT chip was being installed into the μMS ion optics package, one of the EE came off. Microscope analysis of the bond pads revealed that the bond area was smaller than the actual area of the pit (Figure 44). This is believed to be due to the slight curved topography

of the etched pits (in the ring electrode), while the posts had a relatively flat surface (un-etched Si surface), causing a non-conformal inter-substrate boundary.

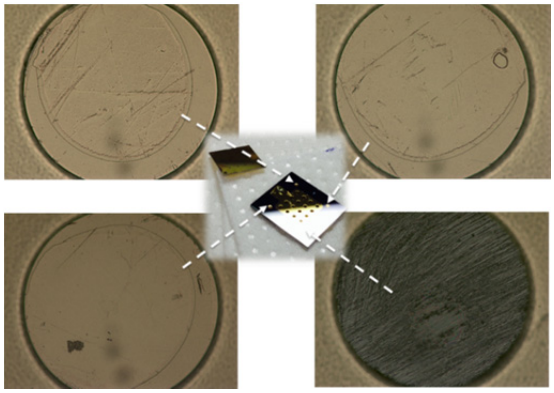

Figure 44 Optical image of the four bond pads in RE used to assemble the μCIT array.

5.1.6.3 Testing

We took a low-risk path to validating the 10 cm^3 μMS ion optics package and test setup, by designing a micro-scale CIT array in stainless steel (SS). The early-on validation of the SS micro-scale CITs is described here, which was performed in a different project, and is followed by the description of the implementation of SS μCITs in the 10 cm^3 μMS ion optics package.

5.1.6.3.1 Early Validation of SS μCITs

Micro-scale CIT array assembly was implemented using photo-etched SS and Kapton sheets, procured from Vacco industries. The SS μCIT array were comprised of three separate SS machined plates stacked together (with Kapton spacers in between each electrode) and co-aligned using four high precision dowel pins procured from McMaster-Carr. The CIT geometry chosen for this approach was z_0/r_0 0.96 which is the most optimum geometry as deduced from prior project simulations and experiments at SRI. The alignment approach used for this design was expected to result in ring-endplate alignment of 50 μm. Figure 45 illustrates the SS μCIT design and dimensions. A conventional MS test setup equipped with a rasterable electron gun was used to generate mass spectra of Xe isotopes using the SS μCIT array. Figure 46 shows the SS μCIT array that was assembled onto a PCB package.

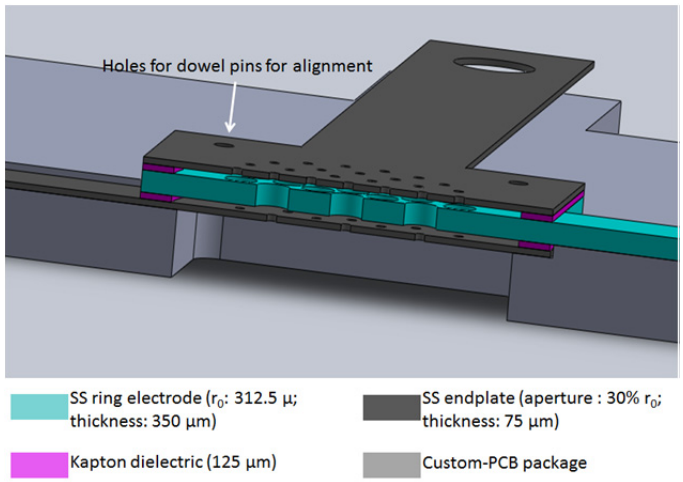

Figure 45 A cross-sectional 3D view to illustrate the SS µCIT array design and assembly.

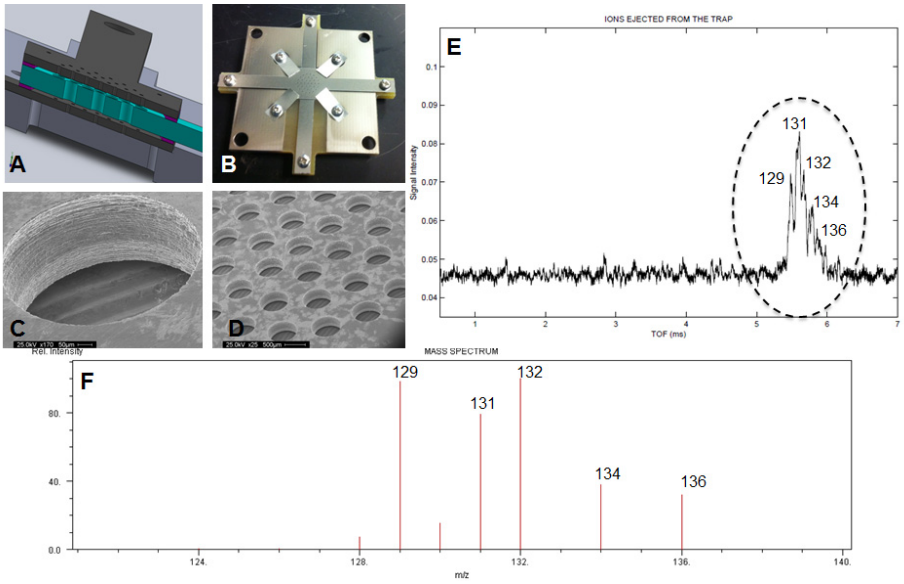

Figure 46 A) A cross-sectional view of the 3-D model of the SS µCIT array comprised of ring electrodes (teal) and two endplates (dark gray) separated by Kapton spacers (magenta), with the entire assembly supported by a fiberglass PCB (light gray) ; B) The three electrodes assembled together; C) High-magnification SEM image of SS ring electrode; D) A low-magnification SEM image showing the SS µCIT ring electrode array; E) Measured mass spectra of Xe showing the various isotopes; F) NIST mass spectra showing relative isotope abundance, for comparison.

Several parameters such as electron beam intensity, energy and focus, Xe partial pressure, He buffer gas partial pressure, ionization time, RF voltage ramp time, RF and ionization voltages, and MCP voltage were varied to find the most optimum settings to maximize

the trapped ion signal while maintaining the best separation of Xe isotopes. Axial modulation was used by applying a low frequency (1/3rd of the RF trapping frequency 7.44 MHz) voltage potential on the endplate that was closer to the MCP detector, to improve the ejected mass resolution. Figure 46 E shows the measured sequentially-scanned mass spectra of Xe showing the various detectable Xe isotopes (129-136 amu) and their relative abundance obtained, using the SS μCIT. Mass resolution is slightly greater than 1 atomic mass unit (noted by overlapping isotope spectral peaks) Figure 46F shows the NIST mass spectra of Xe as a benchmark.

The capacitance of the SS μCITs was measured to be <25 pF. During post testing analysis, the electronics was altered by eliminating the RF amplifier and driving the LC tuned circuit directly from the waveform generator (WaveTek Datron 195). By optimizing the inductor value, an RF voltage of up to 200 V_{p-p} was measured across the SS μCIT array. The average power output from the waveform generator was measured by a power meter (Hewlett Packard 438A) to be in the 55 mW range. This means that the RF amplifier (Ophir 5303055) was “overkill” for this application. It is believed that the μCITs, both Si and SS, can be operated at much lower power consumption as previously reported, as long as the capacitance is maintained in the 20-30 pF range.

5.1.6.3.2 μMS Testing

The form factor and trap sizes of the SS μCITs were identical to those of the μCIT array chip. The RE was designed for an array of 4x4 holes with r_0 312 μm, and the EE was designed to be a 4x4 array of holes with radii equal to 35% of r_0. High-precision, micro-etched Kapton films were used as the dielectric layer to define the gap between the RE and EE, which resulted in a z_0/r_0 ~ 0.96. The SS electrodes were obtained by a vendor and were machined using chemical etching processes. The three SS electrodes were assembled together using four alignment holes on four corners of the electrodes, and using a capillary to mechanically align the three electrodes and the two Kapton spacers separating the three electrodes, as shown in Figure 47 A and B. Figure 47 C shows the assembled SS μCIT

array ready to be integrated into the μMS package. Figure 47 D shows the final setup just before the system was pumped down to perform measurements. For initial validation, a single plate was used as the anode to collect the ions ejected from all the traps across the array.

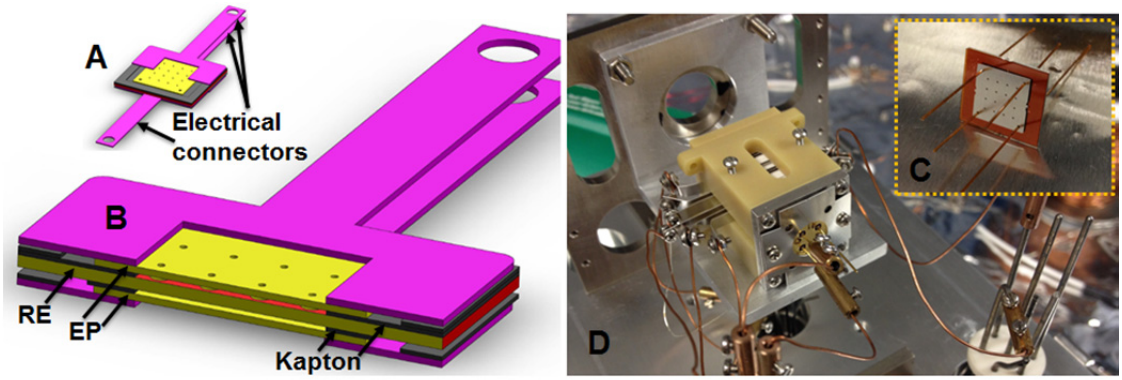

Figure 47 A and B) Design of SS μCIT array; C) assembled SS μCIT array; D) μMS ion optics package with all electrical connections ready to be tested under vacuum.

Several configurations were optimized to reduce the RF pick-up on the anode. Initial MS operation experiments were performed with Ar as the analyte directly introduced into the vacuum chamber via a metering valve. Electronics waveforms and signals were set up using laboratory-scale versatile test equipment to operate the UVLED, MCPs, μCIT array, and detector MCPs. A significant signal of trapped ions using Ar as the analyte was recorded on the anode, using the mass-selective instability mode operation. Experiments are underway to optimize the experiment conditions and operating parameters to improve the mass spectrum. It is promising to see a significant signal of trapped and ejected ions, without any electrical breakdown or severe RF pickup issues. The method of aligning the SS μCIT array can be improved to improve the mass resolution of the array collectively.

5.2 Future Direction

It is expected that further improvements and characterization of the miniature ion optics described in this dissertation can be used to lay the foundation for novel MS architectures; particularly amenable to miniature, ruggedized and low-power MS designs. μCIT arrays are

poised to be instrumental in realization of radically new MS designs. In order to utilize the full potential, alignment accuracy of the μ-electrodes needs to be improved, especially if larger scale arrays are to be operated for enhanced sensitivity. Capacitance of μCIT arrays need to be reduced/maintained low while increasing array scale, to keep the power requirements low ultimately for a handheld MS. μCIT arrays also need ways to efficiently ionize molecules in the traps across the array uniformly and improvement in broad-beam switchable electron sources will be critical to address. Novel assembly and packaging schemes need to be applied to these miniature components. As micro-scale ion optics components are developed and demonstrated, they enable smaller form-factor packaging schemes. This works in favor of the mass analysis process as smaller gaps between 1) the ionization source and the traps and 2) the traps and the detector, can reduce losses during ionization and ion detection processes thereby improving the power efficiency of the overall mass spectrometer. Vacuum systems also needs considerable redesigning, which is enabled by small packages of micro ion optics components.

In another application, the ion concentration qualities of the PIF can used to design a MS tailored for orbital measurement missions. New implementation schemes using sub-arrays of different trap sizes tailored for a specific range of chemicals can be used to perform parallel analysis for missions that only allow a very short window of measurement opportunity. Instrument-scale assembly and integration techniques can be the key to harness the potential these low power miniature ion optics have to offer.

With the advent in robotics, mobile radio-controlled platforms and changing paradigms towards networked constellations, miniature sensors such as a μMS can be instrumental in enabling very low-cost, pervasive and agile, near-real-time chemical screening missions.

REFERENCES

[1] P. E. Miller and M. B. Denton, "The Quadrupole Mass Filter-Basic Operating Concepts," *Journal of Chemical Education,* vol. 63, pp. 617-622, Jul 1986.

[2] J. V. Johnson, R. A. Yost, P. E. Kelley, and D. C. Bradford, "Tandem-In-Space and Tandem-In-Time Mass-Spectrometry-Triple Quadrupoles and Quadrupole Ion Traps," *Analytical Chemistry,* vol. 62, pp. 2162-2172, Oct 1990.

[3] W. C. Wiley and I. H. McLaren, "Time-Of-Flight Mass Spectrometer with Improved Resolution," *Review of Scientific Instruments,* vol. 26, pp. 1150-1157, 1955.

[4] I. V. Chernushevich, A. V. Loboda, and B. A. Thomson, "An Introduction to Quadrupole-Time-Of-Flight Mass Spectrometry," *Journal of Mass Spectrometry,* vol. 36, pp. 849-865, Aug 2001.

[5] A. N. Halliday, D. C. Lee, J. N. Christensen, A. J. Walder, P. A. Freedman, C. E. Jones, C. M. Hall, W. Yi, and D. Teagle, "Recent Developments in Inductively-Coupled Plasma Magnetic-Sector Multiple Collector Mass-Spectrometry," *International Journal of Mass Spectrometry and Ion Processes,* vol. 146, pp. 21-33, Aug 1995.

[6] A. G. Marshall, C. L. Hendrickson, and G. S. Jackson, "Fourier Transform Ion Cyclotron Resonance Mass Spectrometry: A Primer," *Mass Spectrometry Reviews,* vol. 17, pp. 1-35, Jan-Feb 1998.

[7] R. E. March, "An Introduction to Quadrupole Ion Trap Mass Spectrometry," *Journal of Mass Spectrometry,* vol. 32, pp. 351-369, Apr 1997.

[8] C. M. Barshick and J. R. Eyler, "A Glow-Discharge Ion-Source With Fourier-Transform Ion-Cyclotron Resonance Mass-Spectrometric Detection," *Journal of the American Society for Mass Spectrometry,* vol. 3, pp. 122-127, Feb 1992.

[9] É. Mathieu, "Mémoire Sur Le Mouvement Vibratoire D'une Membrane De Forme Elliptique.," *J. math. pure appl.,* vol. 13, p. 66, 1868.

[10] G. Stafford, "Ion Trap Mass Spectrometry: A Personal Perspective," *Journal of the American Society for Mass Spectrometry,* vol. 13, pp. 589-596, Jun 2002.

[11] G. C. Stafford Jr, P. E. Kelley, J. E. P. Syka, W. E. Reynolds, and J. F. J. Todd, "Recent improvements in and analytical applications of advanced ion trap technology," *International Journal of Mass Spectrometry and Ion Processes,* vol. 60, pp. 85-98, 1984.

[12] R. E. March, "Quadrupole Ion Trap Mass Spectrometer," in *Encyclopedia of Analytical Chemistry*, ed: John Wiley & Sons, Ltd, 2006.

[13] J. C. Schwartz, J. E. P. Syka, and I. Jardine, "High-Resolution on a Quadrupole Ion Trap Mass-Spectrometer," *Journal of the American Society for Mass Spectrometry,* vol. 2, pp. 198-204, May-Jun 1991.

[14] R. E. Kaiser, R. G. Cooks, G. C. Stafford, J. E. P. Syka, and P. H. Hemberger, "Operation of a Quadrupole Ion Trap Mass-Spectrometer to Achieve High Mass Charge Ratios," *International Journal of Mass Spectrometry and Ion Processes,* vol. 106, pp. 79-115, May 1991.

[15] S. Haywood, D. B. Langmuir, R. V. Langmuir, and R. F. Wuerker, "Containment Device," ed: Google Patents, 1962.

[16] M.-N. Benilan and C. Audoin, "Confinement D'ions Par Un Champ Electrique De Radio-Fréquence Dans Nne Cage Cylindrique," *International Journal of Mass Spectrometry and Ion Physics,* vol. 11, pp. 421-432, 1973.
[17] R. F. Bonner, J. E. Fulford, R. E. March, and G. F. Hamilton, "The Cylindrical Ion Trap. Part I. General Introduction," *International Journal of Mass Spectrometry and Ion Physics,* vol. 24, pp. 255-269, 1977.
[18] E. R. Badman, R. C. Johnson, W. R. Plass, and R. G. Cooks, "A Miniature Cylindrical Quadrupole Ion Trap: Simulation and Experiment," *Analytical Chemistry,* vol. 70, pp. 4896-4901, Dec 1998.
[19] R. E. Mather, R. M. Waldren, J. F. J. Todd, and R. E. March, "Some Operational Characteristics of a Quadrupole Ion Storage Mass-Spectrometer having Cylindrical Geometry," *International Journal of Mass Spectrometry and Ion Processes,* vol. 33, pp. 201-230, 1980.
[20] T. L. Grebner and H. J. Neusser, "Laser-Produced Ions Stored in a Cylindrical Ion-Trap and Detected in a Reflectron Time-Of-Flight Mass-Spectrometer," *International Journal of Mass Spectrometry and Ion Processes,* vol. 137, pp. L1-L6, Oct 1994.
[21] T. D. Wood, C. W. Ross, and A. G. Marshall, "Selective Parent Ion Axialization for Improved Efficiency of Collision-Induced Dissociation in Laser-Desorption Ionization Fourier-Transform Ion-Cyclotron Resonance Mass-Spectrometry," *Journal of the American Society for Mass Spectrometry,* vol. 5, pp. 900-907, Oct 1994.
[22] G. E. Patterson, A. J. Guymon, L. S. Riter, M. Everly, J. Griep-Raming, B. C. Laughlin, Z. Ouyang, and R. G. Cooks, "Miniature Cylindrical Ion Trap Mass Spectrometer," *Analytical chemistry,* vol. 74, pp. 6145-6153, 2002.
[23] S. Boumsellek and R. J. Ferran, "Trade-offs in miniature quadrupole designs," *Journal of the American Society for Mass Spectrometry,* vol. 12, pp. 633-640, 2001.
[24] Y. Tian, J. Higgs, A. Li, B. Barney, and D. E. Austin, "How Far Can Ion Trap Miniaturization Go? Parameter Scaling and Space-Charge Limits for Very Small Cylindrical Ion Traps," *Journal of Mass Spectrometry,* vol. 49, pp. 233-240, 2014.
[25] H. G. Dehmelt, "Radiofrequency Spectroscopy of Stored Ions. I. Storage.," *Adv. At.. Mol. Phys,* vol. 3, p. 20, 1967.
[26] Available: http://www.marketsandmarkets.com/PressReleases/mass-spectrometry-market.asp
[27] X. Y. Liu and J. Pawliszyn, "On-Site Environmental Analysis by Membrane Extraction with a Sorbent Interface Combined with a Portable Gas Chromatograph System," *International Journal of Environmental Analytical Chemistry,* vol. 85, pp. 1189-1200, Dec 2005.
[28] C. R. Arkin, T. P. Griffin, J. A. Diaz, D. W. Follistein, C. H. Curley, D. P. Floyd, G. R. Naylor, W. D. Haskell, M. Blalock, and F. W. Adams, "A Small Mass Spectrometer System for In Situ Gas Analysis," *Trac-Trends in Analytical Chemistry,* vol. 23, pp. 322-330, Apr 2004.
[29] R. T. Short, S. K. Toler, G. P. G. Kibelka, D. T. R. Roa, R. J. Bell, and R. H. Byrne, "Detection and Quantification of Chemical Plumes using a Portable Underwater Membrane Introduction Mass Spectrometer," *Trac-Trends in Analytical Chemistry,* vol. 25, pp. 637-646, Jul-Aug 2006.
[30] E. R. Badman and R. G. Cooks, "Special feature: Perspective-Miniature mass analyzers," *Journal of Mass Spectrometry,* vol. 35, pp. 659-671, Jun 2000.
[31] L. Gao, Q. Y. Song, G. E. Patterson, R. G. Cooks, and Z. Ouyang, "Handheld Rectilinear Ion Trap Mass Spectrometer," *Analytical Chemistry,* vol. 78, pp. 5994-6002, Sep 2006.

[32] M. G. Blain, L. S. Riter, D. Cruz, D. E. Austin, G. X. Wu, W. R. Plass, and R. G. Cooks, "Towards the Hand-Held Mass Spectrometer: Design Considerations, Simulation, and Fabrication of Micrometer-Scaled Cylindrical Ion Traps," *International Journal of Mass Spectrometry,* vol. 236, pp. 91-104, Aug 2004.
[33] S. Pau, C. S. Pai, Y. L. Low, J. Moxom, P. T. A. Reilly, W. B. Whitten, and J. M. Ramsey, "Microfabricated Quadrupole Ion Trap for Mass Spectrometer Applications," *Physical Review Letters,* vol. 96, Mar 2006.
[34] M. Geear, R. R. A. Syms, S. Wright, and A. S. Holmes, "Monolithic MEMS Quadrupole Mass Spectrometers by Deep Silicon Etching," *Journal of Microelectromechanical Systems,* vol. 14, pp. 1156-1166, Oct 2005.
[35] N. Sillon and R. Baptist, "Micromachined Mass Spectrometer," *Sensors and Actuators B-Chemical,* vol. 83, pp. 129-137, Mar 2002.
[36] J. A. Diaz, C. F. Giese, and W. R. Gentry, "Sub-Miniature ExB Sector-Field Mass Spectrometer," *Journal of the American Society for Mass Spectrometry,* vol. 12, pp. 619-632, Jun 2001.
[37] J. P. Hauschild, E. Wapelhorst, and J. Muller, "Mass Spectra Measured by a Fully Integrated MEMS Mass Spectrometer," *International Journal of Mass Spectrometry,* vol. 264, pp. 53-60, Jun 2007.
[38] R. B. Darling, A. A. Scheidemann, K. N. Bhat, and T. C. Chen, "Micromachined Faraday Cup Array using Deep Reactive Ion Etching," *Sensors and Actuators a-Physical,* vol. 95, pp. 84-93, Jan 2002.
[39] C. A. Spindt, C. E. Holland, A. Rosengreen, and I. Brodie, "Field-Emitter Arrays for Vacuum Microelectronics," *Ieee Transactions on Electron Devices,* vol. 38, pp. 2355-2363, Oct 1991.
[40] G. A. J. Amaratunga, M. Baxendale, N. Rupesinghe, I. Alexandrou, M. Chhowalla, T. Butler, A. Munindradasa, C. J. Kiley, L. Zhang, and T. Sakai, "Field Emission from a New Form of Thin Film Amorphous Carbon Having Nanoparticle Inclusions and Carbon Nanotubes," *New Diamond and Frontier Carbon Technology,* vol. 9, pp. 31-51, 1999.
[41] S. E. Huq, P. D. Prewett, J. C. She, S. Z. Deng, and N. S. Xu, "Field Emission from Amorphous Diamond Coated Silicon Tips," *Materials Science and Engineering B-Solid State Materials for Advanced Technology,* vol. 74, pp. 184-187, May 2000.
[42] A. Olsson, P. Enoksson, G. Stemme, and E. Stemme, "A Valve-Less Planar Pump Isotropically Etched in Silicon," *Journal of Micromechanics and Microengineering,* vol. 6, pp. 87-91, Mar 1996.
[43] S. E. Vargo and E. P. Muntz, "Initial Results from the First MEMS Fabricated Thermal Transpiration-Driven Vacuum Pump," *AIP Conference Proceedings,* vol. 585, pp. 502-509, 2001.
[44] R. Zengerle, J. Ulrich, S. Kluge, M. Richter, and A. Richter, "A Bidirectional Silicon Micropump," *Sensors and Actuators a-Physical,* vol. 50, pp. 81-86, Aug 1995.
[45] S. C. Terry, J. H. Jerman, and J. B. Angell, "Gas-Chromatographic Air Analyzer Fabricated on a Silicon-Wafer," *Ieee Transactions on Electron Devices,* vol. 26, pp. 1880-1886, 1979.
[46] I. M. Lazar, J. Grym, and F. Foret, "Microfabricated Devices: A New Sample Introduction Approach to Mass Spectrometry," *Mass Spectrometry Reviews,* vol. 25, pp. 573-594, Jul-Aug 2006.
[47] G. A. Schultz, T. N. Corso, S. J. Prosser, and S. Zhang, "A Fully Integrated Monolithic Microchip Electrospray Device for Mass Spectrometry," *Analytical Chemistry,* vol. 72, pp. 4058-4063, Sep 2000.
[48] E. R. Badman and R. G. Cooks, "A Parallel Miniature Cylindrical Ion Trap Array," *Analytical Chemistry,* vol. 72, pp. 3291-3297, Jul 2000.

[49] A. M. Tabert, J. Griep-Raming, A. J. Guymon, and R. G. Cooks, "High-Throughput Miniature Cylindrical Ion Trap Array Mass Spectrometer," *Analytical Chemistry,* vol. 75, pp. 5656-5664, Nov 2003.
[50] L. M. Roylance and J. B. Angell, "A Batch-Fabricated Silicon Accelerometer," *Electron Devices, IEEE Transactions on,* vol. 26, pp. 1911-1917, 1979.
[51] J. M. Wells, E. R. Badman, and R. G. Cooks, "A Quadrupole Ion Trap with Cylindrical Geometry Operated in the Mass Selective Instability Mode," *Analytical Chemistry,* vol. 70, pp. 438-444, Feb 1998.
[52] C. R. Arkin, B. Goolsby, and D. A. Laude, "Characterization of a Hybrid Ion Trap," *International Journal of Mass Spectrometry,* vol. 191, pp. 47-57, Aug 1999.
[53] G. Wu, R. G. Cooks, and Z. Ouyang, "Geometry Optimization for the Cylindrical Ion Trap: Field Calculations, Simulations and Experiments," *International Journal of Mass Spectrometry,* vol. 241, pp. 119-132, 2005.
[54] H. Lagadec, C. Meis, and M. Jardino, "Effective Potential of an RF Cylindrical Trap," *International Journal of Mass Spectrometry and Ion Processes,* vol. 85, pp. 287-299, Sep 1988.
[55] W. W. Lee, C. H. Oh, P. S. Kim, M. Yang, and K. S. Song, "Characteristics of Cylindrical Ion Trap," *International Journal of Mass Spectrometry,* vol. 230, pp. 25-31, Nov 2003.
[56] P. K. Tallapragada, A. K. Mohanty, A. Chatterjee, and A. G. Menon, "Geometry Optimization of Axially Symmetric Ion Traps," *International Journal of Mass Spectrometry,* vol. 264, pp. 38-52, Jun 2007.
[57] D. E. Austin, M. Wang, S. E. Tolley, J. D. Maas, A. R. Hawkins, A. L. Rockwood, H. D. Tolley, E. D. Lee, and M. L. Lee, "Halo Ion Trap Mass Spectrometer," *Analytical Chemistry,* vol. 79, pp. 2927-2932, Apr 2007.
[58] F. H. W. Van Amerom, A. Chaudhary, M. Cardenas, J. Bumgarner, and R. T. Short, "Microfabrication of Cylindrical Ion Trap Mass Spectrometer Arrays for Handheld Chemical Analyzers," *Chemical Engineering Communications,* vol. 195, pp. 98-114, 2008.
[59] A. Chaudhary, F. H. W. van Amerom, R. T. Short, and S. Bhansali, "Fabrication and Testing of a Miniature Cylindrical Ion Trap Mass Spectrometer Constructed from Low Temperature Co-Fired Ceramics," *International Journal of Mass Spectrometry,* vol. 251, pp. 32-39, Mar 2006.
[60] F. Laermer and A. Schilp, "Method of Anisotropically Etching Silicon," *US Patent 5,501,893,* Mar 1996.
[61] G. T. Abraham, A. Chatterjee, and A. G. Menon, "Escape Velocity and Resonant Ion Dynamics in Paul Trap Mass Spectrometers," *International Journal of Mass Spectrometry,* vol. 231, pp. 1-16, 2004.
[62] W. R. Plass, "The Dependence of RF Ion Trap Mass Spectrometer Performance on Electrode Geometry and Collisional Processes," Ph.D. Dissertation, Justus-Liebig-Universität Giessen, Germany.
[63] R. E. March and R. J. Hughes, in *Quadrupole Storage Mass Spectrometry*, 1st ed: New York: John Wiley & Sons Inc., 1989, p. 112.
[64] D. A. Dahl, "Simion for the Personal Computer in Reflection," *International Journal of Mass Spectrometry,* vol. 200, pp. 3-25, 2000.
[65] S. I. Ohira and K. Toda, "Micro gas analyzers for environmental and medical applications," *Analytica Chimica Acta,* vol. 619, pp. 143-156, Jul 2008.
[66] J. A. Diaz, C. F. Giese, and W. R. Gentry, "Mass spectrometry for in-situ volcanic gas monitoring," *Trac-Trends in Analytical Chemistry,* vol. 21, pp. 498-514, Aug 2002.
[67] R. J. Bell, W. B. Savidge, S. K. Toler, R. H. Byrne, and R. T. Short, "In situ determination of porewater gases by underwater flow-through membrane inlet mass spectrometry," *Limnology and Oceanography-Methods,* vol. 10, pp. 117-128, Mar 2012.

[68] S. D. Wankel, S. B. Joye, V. A. Samarkin, S. R. Shah, G. Friederich, J. Melas-Kyriazi, and P. R. Girguis, "New constraints on methane fluxes and rates of anaerobic methane oxidation in a Gulf of Mexico brine pool via in situ mass spectrometry," *Deep-Sea Research Part Ii-Topical Studies in Oceanography,* vol. 57, pp. 2022-2029, Nov 2010.
[69] T. P. Griffin, J. A. Diaz, C. R. Arkin, C. Soto, C. H. Curley, and O. Gomez, "Three-dimensional concentration mapping of gases using a portable mass spectrometer system," *Journal of the American Society for Mass Spectrometry,* vol. 19, pp. 1411-1418, Oct 2008.
[70] D. M. Anderson, K. Biemann, G. P. Shulman, P. Toulmin, H. C. Urey, T. Owen, L. E. Orgel, and J. Oro, "Mass-spectrometric analsysis of organic compounds, water and volatile constituents in atmosphere and surface of Mars-Viking Mars Lander," *Icarus,* vol. 16, pp. 111-&, 1972.
[71] J. Kissel and F. R. Krueger, "The organic-component in dust from comet Halley as measured by the Puma mass-spectrometer on board VEGA-1," *Nature,* vol. 326, pp. 755-760, Apr 1987.
[72] P. Eberhardt, M. Reber, D. Krankowsky, and R. R. Hodges, "The D/H and O-18/O-16 ratios in water from comet P/Halley," *Astronomy and Astrophysics,* vol. 302, pp. 301-316, Oct 1995.
[73] Z. Ouyang and R. G. Cooks, "Miniature mass spectrometers," *Annu Rev Anal Chem (Palo Alto Calif),* vol. 2, pp. 187-214, 2009.
[74] J. F. J. Todd, "Theoretical and practical aspects of ion trap performance," *Abstracts of Papers of the American Chemical Society,* vol. 196, pp. 57-ANYL, Sep 1988.
[75] J. M. Wells, E. R. Badman, and R. G. Cooks, "A quadrupole ion trap with cylindrical geometry operated in the mass selective instability mode," *Anal Chem,* vol. 70, pp. 438-444, Feb 1998.
[76] W. Xu, W. J. Chappell, R. G. Cooks, and Z. Ouyang, "Characterization of electrode surface roughness and its impact on ion trap mass analysis," *Journal of Mass Spectrometry,* vol. 44, pp. 353-360, Mar 2009.
[77] M. Yu, M. Fico, S. Kothari, Z. Ouyang, and W. J. Chappell, "Polymer-based ion trap chemical sensor," *Ieee Sensors Journal,* vol. 6, pp. 1429-1434, Dec 2006.
[78] D. E. Austin, M. Wang, S. E. Tolley, J. D. Maas, A. R. Hawkins, A. L. Rockwood, H. D. Tolley, E. D. Lee, and M. L. Lee, "Halo ion trap mass spectrometer," *Anal Chem,* vol. 79, pp. 2927-2932, Apr 2007.
[79] O. J. Orient, A. Chutjian, and V. Garkanian, "Miniature, high-resolution, quadrupole mass-spectrometer array," *Review of Scientific Instruments,* vol. 68, pp. 1393-1397, Mar 1997.
[80] A. M. Tabert, J. Griep-Raming, A. J. Guymon, and R. G. Cooks, "High-throughput miniature cylindrical ion trap array mass spectrometer," *Anal Chem,* vol. 75, pp. 5656-5664, Nov 2003.
[81] E. R. Badman and R. G. Cooks, "Cylindrical ion trap array with mass selection by variation in trap dimensions," *Anal Chem,* vol. 72, pp. 5079-5086, Oct 2000.
[82] S. Pau, C. Pai, Y. Low, J. Moxom, P. Reilly, W. Whitten, and J. Ramsey, "Microfabricated quadrupole ion trap for mass spectrometer applications," *Physical Review Letters,* vol. 96, 2006.
[83] A. Chaudhary, F. H. W. van Amerom, and R. T. Short, "Development of microfabricated cylindrical ion trap mass spectrometer arrays," *Journal of Microelectromechanical Systems,* vol. 18, pp. 442-448, Apr 2009.
[84] S. Pau, W. B. Whitten, and J. M. Ramsey, "Planar geometry for trapping and separating ions and charged particles," *Anal Chem,* vol. 79, pp. 6857-6861, 2007/09/01 2007.

[85] P. Siebert, G. Petzold, A. Hellenbart, and J. Muller, "Surface microstructure miniature mass spectrometer: processing and applications," *Applied Physics a-Materials Science & Processing,* vol. 67, pp. 155-160, Aug 1998.
[86] H. J. Yoon, J. H. Kim, E. S. Choi, S. S. Yang, and K. W. Jung, "Fabrication of a novel micro time-of-flight mass spectrometer," *Sensors and Actuators a-Physical,* vol. 97-8, pp. 441-447, Apr 2002.
[87] S. Taylor, J. J. Tunstall, R. R. A. Syms, T. Tate, and M. M. Ahmad, "Initial results for a quadrupole mass spectrometer with a silicon micromachined mass filter," *Electronics Letters,* vol. 34, pp. 546-547, 1998.
[88] D. V. Wiberg, N. V. Myung, B. Eyre, K. Shcheglov, O. J. Orient, E. Moore, and P. Munz, "LIGA-fabricated two-dimensional quadrupole array and scroll pump for miniature gas chromatograph/mass spectrometer," pp. 8-13, 2003.
[89] N. Sillon and R. Baptist, "Micromachined mass spectrometer," *Sensors and actuators. B, Chemical,* vol. 83, pp. 129-137, 2002.
[90] N. T. Nguyen and T. Q. Truong, "A fully polymeric micropump with piezoelectric actuator," *Sensors and actuators. B, Chemical,* vol. 97, pp. 137-143, 2004.
[91] L. Licklider, X. Q. Wang, A. Desai, Y. C. Tai, and T. D. Lee, "A micromachined chip-based electrospray source for mass spectrometry," *Anal Chem,* vol. 72, pp. 367-375, Jan 2000.
[92] S. Wright, R. Moseley, G. Hong, and S. O'Prey, "MEMS-based nanospray-ionization mass spectrometer," *Journal of Microelectromechanical Systems,* vol. 19, pp. 1430-1443, 2010.
[93] G. T. A. Kovacs, N. I. Maluf, and K. E. Petersen, "Bulk micromachining of silicon," *Proceedings of the Ieee,* vol. 86, pp. 1536-1551, Aug 1998.
[94] R. E. March, "Quadrupole ion trap mass spectrometry: a view at the turn of the century," *International Journal of Mass Spectrometry,* vol. 200, pp. 285-312, Dec 2000.
[95] A. Chaudhary, F. van Amerom, and R. T. Short, "Development of Microfabricated Cylindrical Ion Trap Mass Spectrometer Arrays," *Microelectromechanical Systems, Journal of,* vol. 18, pp. 442-448, 2009.
[96] J. W. Thompson, J. W. Eschelbach, R. T. Wilburn, and J. W. Jorgenson, "Investigation of Electrospray Ionization and Electrostatic Focusing Devices using a Three-Dimensional Electrospray Current Density Profiler," *J Am Soc Mass Spectrom,* vol. 16, pp. 312-23, Mar 2005.
[97] K. Gillig, B. Ruotolo, E. Stone, and D. Russell, "An Electrostatic Focusing Ion Guide for Ion Mobility-Mass Spectrometry," *International Journal of Mass Spectrometry,* vol. 239, pp. 43-49, 2004.
[98] R. C. Blase, J. A. Silveira, K. J. Gillig, C. M. Gamage, and D. H. Russell, "Increased Ion Transmission in IMS: A High Resolution, Periodic-Focusing DC Ion Guide Ion Mobility Spectrometer," *International Journal of Mass Spectrometry,* vol. 301, pp. 166-173, 2011.
[99] E. S. Baker, B. H. Clowers, F. M. Li, K. Tang, A. V. Tolmachev, D. C. Prior, M. E. Belov, and R. D. Smith, "Ion Mobility Spectrometry-Mass Spectrometry Performance Using Electrodynamic Ion Funnels And Elevated Drift Gas Pressures," *J Am Soc Mass Spectrom,* vol. 18, pp. 1176-1187, Jul 2007.
[100] P. V. Johnson, R. Hodyss, K. Tang, W. B. Brinckerhoff, and R. D. Smith, "The Laser Ablation Ion Funnel: Sampling for In Situ Mass Spectrometry on Mars," *Planetary and Space Science,* vol. 59, pp. 387-393, 2011.
[101] P. R. Kemper, N. F. Dupuis, and M. T. Bowers, "A New, Higher Resolution, Ion Mobility Mass Spectrometer," *International Journal of Mass Spectrometry,* vol. 287, pp. 46-57, Oct 2009.
[102] S. G. Moyer and R. J. Cotter, "Atmospheric Pressure MALDI," *Analytical Chemistry,* vol. 74, pp. 468A-476A, Sep 2002.

[103] R. Harkewicz, M. E. Belov, G. A. Anderson, L. Pasa-Tolic, C. D. Masselon, D. C. Prior, H. R. Udseth, and R. D. Smith, "ESI-FTICR mass spectrometry employing data-dependent external ion selection and accumulation," *J Am Soc Mass Spectrom,* vol. 13, pp. 144-154, Feb 2002.
[104] C. M. Barshick and J. R. Eyler, "A Glow-Discharge Ion-Source With Fourier-Transform Ion-Cyclotron Resonance Mass-Spectrometric Detection," *J Am Soc Mass Spectrom,* vol. 3, pp. 122-127, Feb 1992.
[105] J. S. Page, K. Tang, R. T. Kelly, and R. D. Smith, "Subambient Pressure Ionization with Nanoelectrospray Source and Interface for Improved Sensitivity in Mass Spectrometry," *Anal Chem,* vol. 80, pp. 1800-1805, Mar 2008.
[106] K. Tang, A. A. Shvartsburg, H. N. Lee, D. C. Prior, M. A. Buschbach, F. M. Li, A. V. Tolmachev, G. A. Anderson, and R. D. Smith, "High-Sensitivity Ion Mobility Spectrometry/Mass Spectrometry using Electrodynamic Ion Funnel Interfaces," *Anal Chem,* vol. 77, pp. 3330-3339, May 2005.
[107] T. Kim, H. R. Udseth, and R. D. Smith, "Improved ion transmission from atmospheric pressure to high vacuum using a multicapillary inlet and electrodynamic ion funnel interface," *Analytical Chemistry,* vol. 72, pp. 5014-5019, Oct 2000.
[108] I. V. Chernushevich and B. A. Thomson, "Collisional cooling of large ions in electrospray mass spectrometry," *Analytical Chemistry,* vol. 76, pp. 1754-1760, Mar 2004.
[109] C. Y. Ng, "State-selected and state-to-state ion-molecule reaction dynamics," *Journal of Physical Chemistry A,* vol. 106, pp. 5953-5966, Jun 2002.
[110] D. Smith and P. Spanel, "Selected ion flow tube mass spectrometry (SIFT-MS) for on-line trace gas analysis," *Mass Spectrometry Reviews,* vol. 24, pp. 661-700, Sep-Oct 2005.
[111] A. Misharin, K. Novoselov, V. Laiko, and V. M. Doroshenko, "Development and Characterization of a Field-Deployable Ion-Trap Mass Spectrometer with an Atmospheric Pressure Interface," *Analytical Chemistry,* vol. 84, pp. 10105-10112, Nov 2012.
[112] D. Gerlich, "Inhomogeneous RF-Fields - A Versatile Tool for the Study of Processes with Slow Ions," *Advances in Chemical Physics,* vol. 82, pp. 1-176, 1992.
[113] T. Kim, A. V. Tolmachev, R. Harkewicz, D. C. Prior, G. Anderson, H. R. Udseth, R. D. Smith, T. H. Bailey, S. Rakov, and J. H. Futrell, "Design and Implementation of a New Electrodynamic Ion Funnel," *Analytical Chemistry,* vol. 72, pp. 2247-2255, 2000/05/01 2000.
[114] S. A. Shaffer, A. Tolmachev, D. C. Prior, G. A. Anderson, H. R. Udseth, and R. D. Smith, "Characterization of an Improved Electrodynamic Ion Funnel Interface for Electrospray Ionization Mass Spectrometry," *Analytical Chemistry,* vol. 71, pp. 2957-2964, 1999/08/01 1999.
[115] A. V. Tolmachev, T. Kim, H. R. Udseth, R. D. Smith, T. H. Bailey, and J. H. Futrell, "Simulation-Based Optimization of the Electrodynamic Ion Funnel for High Sensitivity Electrospray Ionization Mass Spectrometry," *International Journal of Mass Spectrometry,* vol. 203, pp. 31-47, Dec 2000.
[116] E. P. Kremer, G. J. Evans, and R. E. Jervis, "A Novel Method for the Collimation of Ions at Atmospheric Pressure," *Journal of Physics D: Applied Physics,* vol. 39, pp. 5008-5015, 2006.
[117] D. A. Dahl, "Simion for the Personal Computer in Reflection," *International Journal of Mass Spectrometry,* vol. 200, pp. 3-25, Dec 2000.
[118] D. E. Austin, Y. Peng, B. J. Hansen, I. W. Miller, A. L. Rockwood, A. R. Hawkins, and S. E. Tolley, "Novel Ion Traps Using Planar Resistive Electrodes: Implications for Miniaturized Mass Analyzers," *Journal of the American Society for Mass Spectrometry,* vol. 19, pp. 1435-1441, Oct 2008.

APPENDICES

Appendix A: Copyright Permissions

The following are Copyright permissions for use of material in Chapters 2, 3 and 4 respectively.

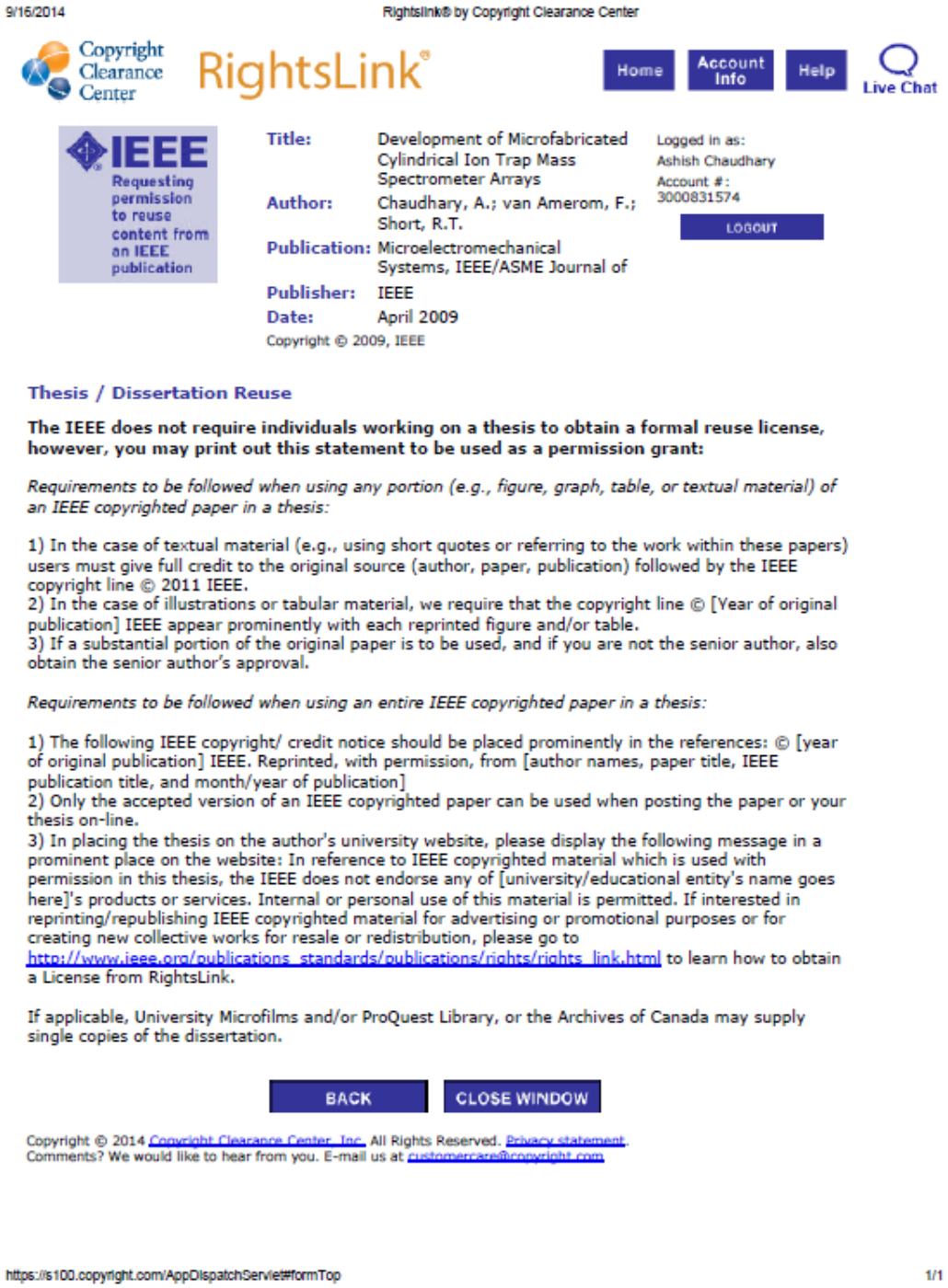

9/16/2014 RightsLink® by Copyright Clearance Center

Copyright Clearance Center RightsLink®

Home | Account Info | Help | Live Chat

IEEE Requesting permission to reuse content from an IEEE publication

Title: Development of Microfabricated Cylindrical Ion Trap Mass Spectrometer Arrays
Author: Chaudhary, A.; van Amerom, F.; Short, R.T.
Publication: Microelectromechanical Systems, IEEE/ASME Journal of
Publisher: IEEE
Date: April 2009
Copyright © 2009, IEEE

Logged in as:
Ashish Chaudhary
Account #:
3000831574
LOGOUT

Thesis / Dissertation Reuse

The IEEE does not require individuals working on a thesis to obtain a formal reuse license, however, you may print out this statement to be used as a permission grant:

Requirements to be followed when using any portion (e.g., figure, graph, table, or textual material) of an IEEE copyrighted paper in a thesis:

1) In the case of textual material (e.g., using short quotes or referring to the work within these papers) users must give full credit to the original source (author, paper, publication) followed by the IEEE copyright line © 2011 IEEE.
2) In the case of illustrations or tabular material, we require that the copyright line © [Year of original publication] IEEE appear prominently with each reprinted figure and/or table.
3) If a substantial portion of the original paper is to be used, and if you are not the senior author, also obtain the senior author's approval.

Requirements to be followed when using an entire IEEE copyrighted paper in a thesis:

1) The following IEEE copyright/ credit notice should be placed prominently in the references: © [year of original publication] IEEE. Reprinted, with permission, from [author names, paper title, IEEE publication title, and month/year of publication]
2) Only the accepted version of an IEEE copyrighted paper can be used when posting the paper or your thesis on-line.
3) In placing the thesis on the author's university website, please display the following message in a prominent place on the website: In reference to IEEE copyrighted material which is used with permission in this thesis, the IEEE does not endorse any of [university/educational entity's name goes here]'s products or services. Internal or personal use of this material is permitted. If interested in reprinting/republishing IEEE copyrighted material for advertising or promotional purposes or for creating new collective works for resale or redistribution, please go to http://www.ieee.org/publications_standards/publications/rights/rights_link.html to learn how to obtain a License from RightsLink.

If applicable, University Microfilms and/or ProQuest Library, or the Archives of Canada may supply single copies of the dissertation.

BACK | CLOSE WINDOW

Copyright © 2014 Copyright Clearance Center, Inc. All Rights Reserved. Privacy statement.
Comments? We would like to hear from you. E-mail us at customercare@copyright.com

https://s100.copyright.com/AppDispatchServlet#formTop 1/1

Title:	Experimental evaluation of micro-ion trap mass spectrometer geometries
Author:	Ashish Chaudhary,Friso H.W. van Amerom,R. Timothy Short
Publication:	International Journal of Mass Spectrometry
Publisher:	Elsevier
Date:	1 October 2014

Order Completed

Thank you very much for your order.

This is a License Agreement between Ashish Chaudhary ("You") and Elsevier ("Elsevier"). The license consists of your order details, the terms and conditions provided by Elsevier, and the payment terms and conditions.

Get the printable license.

License Number	3464971376926
License date	Sep 09, 2014
Licensed content publisher	Elsevier
Licensed content publication	International Journal of Mass Spectrometry
Licensed content title	Experimental evaluation of micro-ion trap mass spectrometer geometries
Licensed content author	Ashish Chaudhary,Friso H.W. van Amerom,R. Timothy Short
Licensed content date	1 October 2014
Licensed content volume number	371
Licensed content issue number	n/a
Number of pages	11
Type of Use	reuse in a thesis/dissertation
Portion	full article
Format	electronic
Are you the author of this Elsevier article?	Yes
Will you be translating?	No
Title of your thesis/dissertation	Miniature Ion Optics Towards a Micro Mass Spectrometer
Expected completion date	Dec 2014
Estimated size (number of pages)	100
Elsevier VAT number	GB 494 6272 12
Permissions price	0.00 USD
VAT/Local Sales Tax	0.00 USD / 0.00 GBP
Total	0.00 USD

ORDER MORE... CLOSE WINDOW

Title:	A novel planar ion funnel design for miniature ion optics
Author:	A. Chaudhary,Friso H. W. van Amerom,R. T. Short
Publication:	Review of Scientific Instruments
Volume/Issue	85/10
Publisher:	AIP Publishing LLC
Date:	Oct 9, 2014
Page Count:	5

Order Completed

Thank you very much for your order.

Click here for Payment Terms and Conditions.

Get a printable version for your records.

License Number	3495930340581
Order Date	Oct 25, 2014
Publisher	AIP Publishing LLC
Publication	Review of Scientific Instruments
Article Title	A novel planar ion funnel design for miniature ion optics
Author	A. Chaudhary,Friso H. W. van Amerom,R. T. Short
Online Publication Date	Oct 9, 2014
Volume number	85
Issue number	10
Type of Use	Thesis/Dissertation
Requestor type	Author (original article)
Format	Electronic
Portion	Excerpt (> 800 words)
Will you be translating?	No
Title of your thesis / dissertation	Miniature Ion Optics Towards a Micro Mass Spectrometer
Expected completion date	Dec 2014
Estimated size (number of pages)	100
Total	0.00 USD

ORDER MORE... CLOSE WINDOW

ABOUT THE AUTHOR

Ashish Chaudhary received B.E. degree in electrical engineering (EE) from C. R. State College of Engineering, Haryana, India in 2001, and M.S. in EE from University of South Florida (USF) in 2004 and is currently pursuing Ph.D. from USF in EE.

In 2004, he started working as a MEMS research engineer at Center for Ocean Technology at USF St. Petersburg. His primary job responsibility was to develop micromachining processes to build miniature ion trap arrays in Silicon towards miniaturization of ion trap mass spectrometers (MS). From April 2007, he has been with SRI International as research engineer. At SRI, he expanded his job responsibilities beyond MEMS implementation and had hands-on-experience with the operation and testing of custom-designed MS test setups. His areas of interest include extreme miniaturization of mass spectrometer components using MEMS technology and expanding the application base for such a sensor beyond conventional applications. He has been working on optimization of μCIT arrays and development of matched electron source for dedicated ionization in each trap of the array. More recently, he's interested in exploring design alterations that will be required to deploy a μMS in LEO/outer space.